A Search for Anomalous Muon Neutrino Disappearance and Tau Neutrino Appearance using NOvA Near Detector

Thesis submitted to
Cochin University of Science and Technology

in partial fulfillment of the requirements for the award of the degree of

DOCTOR OF PHILOSOPHY

by
Rijeesh K

Department of Physics
Cochin University of Science and Technology
Kochi - 682022

November 2018

A Search for Anomalous Muon Neutrino Disappearance and Tau Neutrino Appearance using NOvA Near Detector

PhD Thesis in the field of High Energy Physics

Author
Rijeesh K
Department of Physics
Cochin University of Science and Technology
Kochi - 682022
rijeeshk@fnal.gov, rijeeshkodencheri@gmail.com

Research Supervisor
Dr. Ramesh Babu Thayyullathil
Emeritus Scientist
Department of Physics
Cochin University of Science and Technology
Kochi - 682022
rameshbabut@gmail.com

Research Co-supervisor
Dr. Robert K Plunkett
Senior Scientist
Fermi National Accelerator Laboratory
Batavia
IL - 60510
plunk@fnal.gov

DECLARATION

I hereby declare that the work presented in this thesis is based on the original research work done by me under the guidance of Dr. Ramesh Babu Thayyullathil, Department of Physics, Cochin University of Science and Technology, Kochi, India, 682022 and Dr. Robert K Plunkett, Fermi National Accelerator Laboratory, Batavia, IL, USA, 60510 and has not been included in any other thesis submitted previously for the award of any degree.

Kochi

Rijeesh K

November 10, 2018

CERTIFICATE

Certified that the work presented in this thesis entitled **"A Search for Anomalous Muon Neutrino Disappearance and Tau Neutrino Appearance using NOvA Near Detector"** is based on the bonafide record of research work done by Rijeesh K, under our guidance in the Department of Physics, Cochin University of Science and Technology, Kochi, 682022 and at the Fermi National Accelerator Laboratory, Batavia, IL, USA, 60510 in partial fulfillment of the requirements for award of the degree of Doctor of Philosophy and has not been included in any other thesis submitted for the award of any degree. All the relevant corrections and modifications suggested by the audience during the pre-synopsis seminar and recommendations by doctoral committee of the candidate have been incorporated in the thesis.

Kochi

November 05, 2018

Dr. Ramesh Babu T

(Supervising Guide)

Batavia, IL

November 10, 2018

Dr. Robert K Plunkett

(Joint Guide)

Acknowledgements

First and foremost, I would like to thank my supervisor Dr. Ramesh Babu Thayyullathil, for his guidance and encouragement throughout my Ph.D. years. I acknowledge my sincere gratitude to Dr. Robert K Plunkett, my co-supervisor at Fermilab. Rob's nice hospitality and constructive recommendations on this work greatly helped me.

My special gratitude to late Dr. Rajendran Raja, Senior Scientist, Femilab who helped our University to become a part of the Indian Institutions and Fermilab collaboration. My sincere thanks to Prof. Brajesh C Choudhary, the Spokesperson of the DST project entitled "Collaboration by Indian Physicists on Neutrino Project" at Fermilab, USA. I also want to thank the Department of Science and Technology, India, Fermilab and NOvA collaborators and all members of collaborating Indian Institutions, for their help and support.

I am thankful to the conveners of our group Prof. Alex Sousa, Dr. Louise Suter and Dr. Gavin Davies. Louise's day-to-day support, availability and constructive suggestions greatly helped me in keeping my progress on schedule. I would like to express my very great appreciation to Prof. Adam Aurisano for his valuable and constructive suggestions during the

planning and development of this research work. His willingness to give his time so generously has been very much appreciated. I also would like to thank Dr. John Cooper and Dr. Peter Shanahan for their constant support and help at the Lab. I wish to acknowledge the help provided by Dr. Christopher Backhouse for working with CAFAna and Dr. Alex Himmel for helping me with production software. I am particularly grateful for the assistance given by the staffs at Fermilab. Assistance provided by Kappy and Etta was greatly appreciated.

I would like thank all Neutrino Social Organizing Committee (NSOC) members at Fermilab. I would like to offer my special thanks to Prof. Chang Kee for giving me the opportunity to join the committee, which greatly helped me to expand my friendship circle at Fermilab. Thanks to all my friends at the Fermilab. Thanks to all teachers and non-teaching staffs at CUSAT. My sincere thanks to all research scholars for the times that we spent together and making my life at CUSAT more enjoyable throughout my research. This would not have been possible without the support of my family. Finally, I would like to express my very great appreciation to my family, especially for my parent's and brother Rajaneesh's support throughout my life.

Rijeesh K

Preface

The NOvA experiment consists of two finely segmented, liquid scintillator detectors operating 14.6 mrad off-axis from the NuMI muon-neutrino beam. The Near Detector (ND) is located in the Fermilab campus, 1 km from the NuMI target, while the Far Detector (FD) is located at Ash River, MN, 810 km from the NuMI target. The NOvA experiment is primarily designed to measure electron-neutrino appearance at the FD using the ND to control systematic uncertainties. However, the ND is well suited to search for anomalous short-baseline (SBL) oscillations. The standard three-flavor neutrino oscillations have well explained by a wide range of neutrino experiments. The anomalous results, such as electron-antineutrino excess seen by LSND and MiniBooNE do not fit the three-flavor paradigm. This can be explained by an additional fourth flavor sterile neutrino at a larger mass scale than the existing three flavor neutrinos. This thesis presents a novel method for selecting tau neutrino interactions with high purity at the ND using a convolutional neural network (CNN). Using this method, the preliminary results of anomalous SBL muon-neutrino disappearance and tau-neutrino appearance due to sterile neutrino oscillations in NOvA will be shown.

Chapter 1 briefly explains the history of neutrino physics. The discovery of neutrinos, the phenomena of neutrino oscillations and the concept of sterile neutrinos are discussed in this chapter. It also describes the different oscillation experiments which confirmed the neutrino oscillation phenomena and the sterile neutrino experiments across the globe. The standard three flavor neutrino oscillation model, the matter effect and the sterile neutrino oscillations are briefly discussed in this chapter.

Chapter 2 is briefing the history of tau-neutrinos, the first direct detection of ν_τ's performed by the DONUT collaboration at Fermilab and other studies conducted by various experiments. The experiments which searched for the large mass-squared splitting oscillations are also briefly discussed in this chapter. The chapter concludes with various experiments in relation with ν_τ such as The NOMAD and CHORUS experiments.

Chapter 3 describes the NOvA experiment, the neutrino beam used for the experiment and the detector technology. It also discuss the neutrino beam production, the detector technology and the details of the NOvA data taking. The simulation packages used for the neutrino beam, detectors and neutrino interactions in the detectors are briefly discussed in this chapter. The calibration of the detectors, neutrino event reconstruction and the particle identifiers used in NOvA are discussed in the last part of this chapter.

Chapter 4 summaries the particle identifiers used in the tau-neutrino appearance analysis and the sideband studies conducted to validate these particle identifiers. Boosted Decision Trees (BDT) implemented in the TMVA package of ROOT software and CNN are used for developing these particle identifiers. The three different particle discriminators developed for the hadronic mode ν_τ Charged Current (CC) interactions are detailed in this chapter.

Chapter 5 details the event selection criteria used for the joint muon-neutrino disappearance and the tau-neutrino appearance analysis in the NOvA ND. A CNN based particle identifiers called Convolutional Visual Network (CVN) is used as a primary selector for the $\nu_\mu \to \nu_\mu$ selection and the BDT based three separate particle discriminants are used for the $\nu_\mu \to \nu_\tau$ selections. The details of the preselection cuts and final selection cuts are briefly discussed in this chapter.

Chapter 6 briefly present the systematic studies conducted for this analysis. The overall estimate of the uncertainties may arise due to any elements involved in the neutrino simulation. The systematic uncertainties arise from various elements in the neutrino beam part and the detector are detailed in this chapter.

Chapter 7 summarizes the studies conducted using a simulated 'fake data' to find the sensitivity of NOvA ND to the heavy sterile neutrinos. The chapter presents the results of the sensitivity study conducted in a parameter space formed between $\Delta m_{41}{}^2$ and $\sin^2 2\theta_{\mu\tau}$ using $\nu_\mu \to \nu_\tau$, $\nu_\mu \to \nu_\mu$ and a joint $\nu_\mu \to \nu_\tau$ and $\nu_\mu \to \nu_\mu$ oscillation fits. This chapter also presents the sensitivity of NOvA ND to $\Delta m_{41}{}^2$ vs. $\sin^2 \theta_{24}$ using the joint $\nu_\mu - \nu_\tau$ fit.

Chapter 8 presents a summary of the results of the analysis. The future plan includes the improvements in the sensitivity by reducing the systematic uncertainties and improving the purity by developing a CVN based particle identifiers for the hadronic and leptonic τ decay modes separately.

Published Papers

- M. A. Acero,..., R. Keloth *et al.*, (NOvA Collaboration), *New constraints on oscillation parameters from ν_e appearance and ν_μ disappearance in the NOvA experiment*, Published in Phys. Rev. D 98, 032012 (2018).

- P. Adamson,..., R. Keloth *et al.*, (NOvA Collaboration), *Search for active-sterile neutrino mixing using neutral- current interactions in NOvA*, Published in Phys. Rev. D 96, 072006.

- P. Adamson,..., R. Keloth *et al.*, (NOvA Collaboration), *Constraints on Oscillation Parameters from ν_e Appearance and ν_μ Disappearance in NOvA*, Published in Phys.Rev.Lett. 118 (2017) no.23, 231801.

- P. Adamson,..., R. Keloth *et al.*, (NOvA Collaboration), *Measurement of the neutrino mixing angle θ_{23} in NOvA*, Published in Phys.Rev.Lett. 118 (2017) no.15, 151802.

- G.S. Davies,..., R. Keloth *et al.*, *Searches for Sterile Neutrinos with NOvA*, Proceedings of Science: International Conference on HEP, 972 (2016).

- Rijeesh Keloth *et al.*, *NOvA Short-Baseline Tau Neutrino Appearance Search*, Conference proceedings, DPF 2107, Fermilab.

- A. Aurisano and R. Keloth, *NOvA Short-Baseline Tau Neutrino Appearance Search*, Published in J. Phys.: Conf. Ser. 888 012143(2017).

Conference Talks and Posters

- *NOvA's Short-Baseline Tau Neutrino Appearance Search* (talk)
  New Perspectives, Fermilab, 2018.
- *NOvA Short-Baseline Tau Neutrino Appearance Search* (poster)
  Young Investigators Meeting (YIM-C), Chicago, 2017.
- *NOvA Short-Baseline Tau Neutrino Appearance Search* (talk)
  New perspectives, Fermilab, 2017.
- *NOvA Short-Baseline Tau Neutrino Appearance Search* (poster)
  Meeting of Division of Particles and Fields of American Physical Society, Fermilab, 2017.
- *NOvA Short-Baseline Tau Neutrino Appearance Search* (talk)
  April Meeting of American Physical Society. Washington DC, Jan. 2016.
- *NOvA Short-Baseline Tau Neutrino Appearance Search* (poster)
  International Neutrino Summer School, Fermilab, 2017.
- *NOvA Short-Baseline Tau Neutrino Appearance Search* (joint poster)
  Neutrino '16, London, 2016.
- *Searches for Sterile Neutrinos with NOvA* (joint poster)
  International Conference on HEP, Chicago, 2016.

Contents

List of Tables

List of Figures

Chapter 1

Introduction

Neutrinos are one of the most abundant, elusive yet, particles in the universe. The existence of neutrinos was first postulated by Wolfgang Pauli in 1930, while investigating the puzzle of radioactive beta decay. Pauli described his idea as "a desperate remed" in a letter to a group of prominent nuclear physicists who were attending a conference in Tuebingen, Germany [1]. Beta decay is the process in which a neutron decays into a proton and, to conserve electric charge, it also emits an electron. The experiments showed that both conservation of energy and angular momentum were violated by this process, which was solved by Pauli, by suggesting that another particle was also emitted, what we now call the neutrino, which happened to be very hard to detect experimentally. Pauli introduced these particles such that they have a very light mass and electrically neutral. These chargeless particles interact with matter only via weak force and gravity, which makes them extremely hard to detect.

1.1   Neutrino Interactions

As mentioned above, the weak force mediates the neutrino interactions. The β decay can be described in the form of four point interaction which involves e, p, n and ν in the same point in space and time. The matrix element M for this four point vertex can be written as,

$$M = G_F(\bar{u}_n\gamma_\mu u_p)(\bar{u}_\nu\gamma^\mu u_e), \tag{1.1}$$

where G_F is the Fermi coupling constant, u_is are the Dirac spinors and γ_μs are the Dirac gamma matrices. This interaction is a Vector-Vector (V–V) type, need no propagator and conserves the parity. In 1956, Wu *et al.*, discovered the parity violation in weak interactions [2]. Using this parity violation, the V–V nature of interaction in Eq. (1.1) is replaced by Vector–Axial (V–A) current and the matrix element takes the form as,

$$M = \frac{G_F}{\sqrt{2}}\left[\bar{u}_n\gamma^\mu(1-\gamma^5)u_p\right]\left[\bar{u}_\nu\gamma_\mu(1-\gamma^5)u_e\right]. \tag{1.2}$$

Later, Sheldon Lee Glashow, Abdus Salam and Steven Weinberg unified electro-magnetic and weak interaction and put forward the electroweak theory [3, 4]. They were awarded the Nobel Prize in Physics in 1979 for their contributions to the theory of the unified weak and electromagnetic interaction between elementary particles, including, the
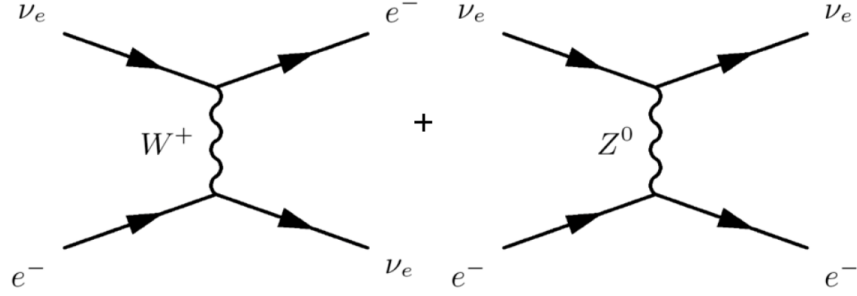
Figure 1.1: The Feynman diagram of CC interaction mediated by a $W_{\pm}$ boson (left) and the NC interaction mediated by the Z_0 boson (right).

prediction of the weak neutral current (NC). This is the theory with spontaneously broken symmetry, $SU(2) \times U(1)_Y \to U(1)_{EM}$, which predicts three broken generators and hence three gauge bosons ($W_{\pm}$ and Z_0). The four point interaction in the Fermi theory was replaced by ($W_{\pm}$, Z_0) propagator. The weak interaction mediated by $W_{\pm}$ boson is called the charged current (CC) interaction and the weak interaction mediated by Z_0 is called the neutral current (NC) interaction. Figure 1.1 shows the Feynman diagrams of weak interaction mediated by $W_{\pm}$ (CC) and Z_0 (NC).

From Eq. (1.2), the e–ν vertex can be written as,

$$j_{\bar{\mu}} = \bar{u}_\nu \gamma_\mu \left(\frac{1 - \gamma^5}{2} \right) u_e, \tag{1.3}$$

and further which can be expressed as,

$$j_{\bar{\mu}} = \bar{\nu}_L \gamma_{\bar{\mu}} e_L, \tag{1.4}$$

where, ν_L and e_L are the left handed chiral projections which can be written as,

$$\bar{\nu}_L = \bar{u}_\nu \frac{1}{2}\left(1 + \gamma^5\right) \quad \text{and} \quad e_L = \frac{1}{2}\left(1 - \gamma^5\right) u_e. \qquad (1.5)$$

The weak CC interaction allows the coupling to only left-handed chiral fermions and therefore the right handed coupling to CC interaction vanishes. The left-handed neutrinos with weak isospin z projection $I_z = 1/2$ and corresponding left handed lepton with projection $I_z = -1/2$ form a weak isospin doublet. The right-handed neutrino is a singlet with $I = 0$.

1.2   Neutrino Mass

In the Standard Model, the generation of masses for the fundamental particles is described by incorporating the Higgs mechanism. With the Higgs mechanism, the electroweak spontaneous symmetry breaking (SSB), the particles attain mass via Yukawa coupling with the Higgs field. But neutrinos remain massless because of the lack of right-handed neutrinos. The experimental evidence from neutrino oscillation experiments proves that neutrinos do have mass. We need to go beyond Standard Model to explain it.

In one of such theories, a Dirac mass term can be added as,

$$m_D \bar{\psi}\psi = m_D \bar{\psi}_L \psi_R + m_D \bar{\psi}_R \psi_L, \tag{1.6}$$

and a Majorana mass term as,

$$m_L \bar{\psi}_L^C \psi_L + m_R \bar{\psi}_R^C \psi_R. \tag{1.7}$$

The Lagrangian can be written as [5],

$$
\begin{aligned}
L_m &= \frac{1}{2}(L_L^D + L_R^D + L_L^M + L_R^M) + h.c, &(1.8)\\
&= m_D \bar{\psi}_R \psi_L + m_D \bar{\psi}_L^C \psi_R^C + m_L \bar{\psi}_L^C \psi_L + m_R \bar{\psi}_R^C \psi_R. &(1.9)
\end{aligned}
$$

This can be written in the matrix form as shown below:

$$L_m \approx \begin{pmatrix} \bar{\psi}_L^C & \bar{\psi}_R \end{pmatrix} \begin{pmatrix} m_L & m_D \\ m_R & m_D \end{pmatrix} \begin{pmatrix} \psi_L \\ \psi_R^C \end{pmatrix}. \tag{1.10}$$

By diagonalizing the matrix, we can get the expression for the mass of mass eigenstate as shown below:

$$m_{1,2} = \frac{1}{2}\left[(m_L + M_R) \pm \sqrt{(m_L - m_R)^2 + 4m_D^2} \right]. \tag{1.11}$$

If $m_L = 0$ and $m_R >> m_D$, Eq. (1.11) becomes, $m_1 = \frac{m_D^2}{m_R}$, which gives mass of the field ν_1 and $m_2 = m_R\left(1 + \frac{m_D^2}{m_R^2}\right) \approx m_R$ which is the mass of the field ν_2. The presence of the suppression factor $\frac{1}{m_R}$ causes one neutrino mass to be very large if the other one is very small. This

explains the cause of relative smallness of the neutrino mass and is called seesaw mechanism [6].

1.3   First Detection of the Neutrino

The first experimental observation of the neutrino interaction was made by Frederic Reins, Clyde Cowan, Jr, and collaborators in 1956 at the Savannah River Plant in South Carolina [7,8]. The source of neutrinos was beta decays taking place in a nuclear reactor. The experiment observed anti-electron neutrinos and the governing process is the following:

$$p + \bar{\nu}_e \rightarrow n + e^+. \tag{1.12}$$

Reins received Nobel prize for this first detection of neutrino in 1995. In 1962 the muon-neutrino was discovered in Brookhaven National Laboratory using the first neutrino beam produced by colliding protons on a target, producing pions that decayed into muons and muon-neutrinos [10]. Leon Lederman, Melvin Schwartz and Jack Steinberger shared the Nobel Prize in Physics in 1988 for the discovery of muon-neutrinos. The tau-neutrino was discovered at Fermilab by the Direct Observation of NU Tau (DONUT) collaboration in 2000 [11]. Measurements of the width of the decay of the Z boson have shown that there is no possibility for more than three generations of active neutrino flavors [12].

1.4 Missing Solar Neutrinos

In 1964, S. N. Bahcall predicted a solar neutrino flux of 5×10^6 neutrinos per cm^{2}s from solar modeling [13]. However the solar neutrino telescope measured the rate of neutrino emission from the Sun at only one third of the expected flux. This deficiency of neutrinos was found to be difficult to explain and was called the *solar neutrino problem*. Recent results from the Sudbury Neutrino Observatory (SNO) suggest that a reasonable number of the electron-neutrinos produced by the Sun are oscillated into muon-neutrinos on the way to the earth [22, 23]. The observations at SNO are consistent with the solar models of neutrino flux assuming that the "neutrino oscillation" is responsible for observation of neutrinos other than electron-neutrinos.

1.5 The Neutrino Flavor Mixing

The oscillations between neutrinos and anti-neutrinos were first predicted by Bruno Pontecorvo, in 1957, later the theory was developed by Maki, Nakagawa and Sakata in 1962 [21] and further elaborated by Pontecorvo again in 1967 [20]. Neutrino oscillation is a quantum mechanical phenomenon where a specific flavor of neutrino, while propagating, can have a probability for changing into a different flavor. The simplest form of neutrino oscillations can be expressed as a unitary transformation relating the flavor and mass eigen-basis.

1.5.1   The PMNS Matrix

The general relation between neutrino flavor and mass eigen states can
be expressed as,

$$|\nu_\alpha\rangle = \sum_j U^*_{\alpha j}|\nu_j\rangle, \tag{1.13}$$

where $\nu_\alpha = \{\nu_e, \nu_\mu, \nu_\tau\}$ is a neutrino with definite flavor, $\nu_j = \{\nu_1, \nu_2, \nu_3\}$
is a neutrino with definite mass and $U^*_{\alpha j}$, the mixing strength between
flavor and mass eigen states is known as the Pontecorvo-Maki-Nakagawa-
Sakata (PMNS) matrix [21].

The time-dependent quantum mechanical neutrino flavor state can
be written as,

$$|\nu(t)\rangle = U^*_{\alpha j}e^{-im_j^2 t/2E}|\nu_j\rangle \tag{1.14}$$

One can derive the neutrino oscillation probability for a neutrino with
flavor α oscillating to a neutrino with flavor β from Eq. (1.14) as

$$
\begin{aligned}
\mathrm{P}_{(\nu_\alpha \to \nu_\beta)} &= |\langle\nu_\beta|\nu(t)\rangle|^2 \tag{1.15}\\
&= \sum_j |U_{\beta j}U^*_{\alpha j}e^{-im_j^2 t/2E}|^2. \tag{1.16}
\end{aligned}
$$

$$
\begin{aligned}
\mathrm{P}_{(\nu_\alpha \to \nu_\beta)} = &\delta_{\alpha\beta} - 4\sum_{i>j}\mathcal{R}(\mathrm{U}^*_{\alpha i}\mathrm{U}_{\beta i}\mathrm{U}_{\alpha j}\mathrm{U}^*_{\beta j})\sin^2\left(\frac{\Delta m_{ij}^2 L}{4E}\right)\\
&+ 2\sum_{i>j}\mathcal{I}(\mathrm{U}^*_{\alpha i}\mathrm{U}_{\beta i}\mathrm{U}_{\alpha j}\mathrm{U}^*_{\beta j})\sin^2\left(\frac{\Delta m_{ij}^2 L}{4E}\right).
\end{aligned}
\tag{1.17}
$$

Two-flavor Oscillation Model

The unitary matrix for a system of two neutrino flavors simplifies as

$$U = \begin{pmatrix} \cos\theta & \sin\theta \\ -\sin\theta & \cos\theta \end{pmatrix}, \tag{1.18}$$

and the probability for $\nu_\alpha(\bar{\nu}_\alpha) \to \nu_\beta(\bar{\nu}_\beta)$ oscillation can be expressed as,

$$P_{\nu_\alpha(\bar{\nu}_\alpha)\to\nu_\beta(\bar{\nu}_\beta)} = \sin^2 2\theta_{\alpha\beta} \sin^2\left(\frac{\Delta m^2_{\alpha\beta}L}{4E}\right), \tag{1.19}$$

where E is the neutrino energy, θ is the mixing angle between the flavor eigenstates (α, β represents the neutrino flavors, μ, e or τ) and the mass eigenstates, and Δm^2 is the mass squared difference of the neutrino mass eigenstates.

Three-flavor Oscillation Model

PMNS matrix for a system of three neutrinos is a 3×3 matrix. A general n×n unitary matrix can be parameterized by n(n-1)/2 rotation angles and (n-1)(n-2)/2 complex phase factors.

$$\begin{pmatrix} \nu_e \\ \nu_\mu \\ \nu_\tau \end{pmatrix} = \begin{pmatrix} U_{e1} & U_{e2} & U_{e3} \\ U_{\mu1} & U_{\mu2} & U_{\mu3} \\ U_{\tau1} & U_{\tau2} & U_{\tau3} \end{pmatrix} \begin{pmatrix} \nu_1 \\ \nu_2 \\ \nu_3 \end{pmatrix}. \tag{1.20}$$

The unitary matrix can be expressed as the product of three rotation matrices as,

$$
\begin{aligned}
\text{U} &= \begin{pmatrix} 1 & 0 & 0 \\ 0 & c_{23} & s_{23} \\ 0 & -s_{23} & c_{23} \end{pmatrix} \begin{pmatrix} c_{13} & 0 & s_{13}e^{-i\delta_{CP}} \\ 0 & 1 & 0 \\ -s_{13}e^{-i\delta_{CP}} & 0 & c_{13} \end{pmatrix} \begin{pmatrix} c_{12} & s_{12} & 0 \\ -s_{12} & c_{12} & 0 \\ 0 & 0 & 1 \end{pmatrix} \\
&= \begin{pmatrix} c_{12}c_{13} & s_{12}c_{13} & s_{13}e^{-i\delta_{CP}} \\ -s_{12}c_{23} - c_{12}s_{13}s_{23}e^{-i\delta_{CP}} & c_{12}c_{23} - s_{12}s_{13}s_{23}e^{-i\delta_{CP}} & c_{13}s_{23} \\ s_{12}s_{23} - c_{12}s_{13}c_{23}e^{-i\delta_{CP}} & -c_{12}s_{23} - s_{12}s_{13}c_{23}e^{-i\delta_{CP}} & c_{13}c_{23} \end{pmatrix}.
\end{aligned}
$$

$$(1.20a)$$

where $c_{ij} = \cos\theta_{ij}$ and $s_{ij} = \sin\theta_{ij}$.

1.5.2   Matter Effect

The above oscillation models were developed for the neutrinos propagating in a vacuum. However in practical situations the most experiments involve the neutrinos traveling through matter, either the Earth or Sun. The oscillation probabilities are drastically changed when we include these matter effects. The process is called Mickeyev–Smirnov–Wolfenstien (MSW) effect [14]. The ordinary matter contains a huge number of electrons but not muon and tau leptons. The electrons contribute an additional potential term, $V_e = \pm\sqrt{2}G_F N_e$, where G_F is Fermi's constant, N_e is the electron number density, the positive sign is for neutrinos and negative for antineutrinos. This potential adds an

additional term to the Schrödinger equation which affects the time evolution of the flavor states and thus a change in the oscillation probability. Following is the easiest way to understand the matter effect, write the time evolution of the two-flavor system,

$$
i \begin{pmatrix} \nu_e(\bar{\nu}_e) \\ \nu_\mu(\bar{\nu}_\mu) \end{pmatrix} = \left[U \begin{pmatrix} \frac{m_1^2}{2E} & 0 \\ 0 & \frac{m_2^2}{2E} \end{pmatrix} U^\dagger + \begin{pmatrix} \pm V_e & 0 \\ 0 & 0 \end{pmatrix} \right] \begin{pmatrix} \nu_e(\bar{\nu}_e) \\ \nu_\mu(\bar{\nu}_\mu) \end{pmatrix}. \qquad (1.21)
$$

After applying some trigonometric identities and dropping the common diagonal terms, Eq. (1.21) reduces to,

$$
i \begin{pmatrix} \nu_e(\bar{\nu}_e) \\ \nu_\mu(\bar{\nu}_\mu) \end{pmatrix} = \frac{1}{4E} \begin{pmatrix} -\Delta m^2{}_{21} \cos 2\theta \pm 4EV_e & \Delta m_{21}^2 \sin 2\theta \\ \Delta m_{21}^2 \sin 2\theta & \Delta m_{21}^2 \cos 2\theta \end{pmatrix} \begin{pmatrix} \nu_e(\bar{\nu}_e) \\ \nu_\mu(\bar{\nu}_\mu) \end{pmatrix}.
$$
$$(1.22)$$

This Hamiltonian can be again diagonalized with another unitary transformation, $H_M = U_M^\dagger H U_M$, which results in,

$$
H_M = \frac{1}{2} \begin{pmatrix} \frac{\Delta m_M^2}{2E} & 0 \\ 0 & \frac{\Delta m_M^2}{2E} \end{pmatrix}, \qquad (1.23)
$$

$$
U_M = \begin{pmatrix} \cos \theta_M & \sin \theta_M \\ -\sin \theta_M & \cos \theta_M \end{pmatrix}, \qquad (1.24)
$$

where

$$
\sin 2\theta_M \equiv \frac{\sin \theta}{A_M}, \qquad (1.25)
$$

$$
\Delta m_M{}^2 \equiv \Delta m^2{}_{21} A_M, \qquad (1.26)
$$

$$A_M \equiv \sqrt{\left(\cos 2\theta \mp \frac{2EV_e}{\Delta m_{21}^2} \right)^2 + \sin^2 2\theta}, \qquad (1.27)$$

The negative sign in A_M is for neutrino and positive for antineutrino. If we set electron density to be zero, V_e goes to zero and we get the vacuum solution. Matter creates a resonant effect pushing θ_M maximally to 45° when the term inside the parenthesis in Eq. (1.27) for A_M is zero.

1.6 Experimental Evidence of Neutrino Oscillations

The standard three flavor neutrino oscillation parameters has been well studied by various solar, atmospheric, accelerator and reactor neutrino experiments. These experiments are designed to have sensitivity to certain oscillation parameters depending on the baseline length neutrino travels and the energy of the neutrino beam used in the experiment.

1.6.1 Solar Neutrino Experiments

The solar neutrino studies performed by Ray Davis in 1968, at the Homestake mine gave the first evidence of neutrino oscillations [15]. The experiment measured the flux of neutrinos coming from the following ^{8}B
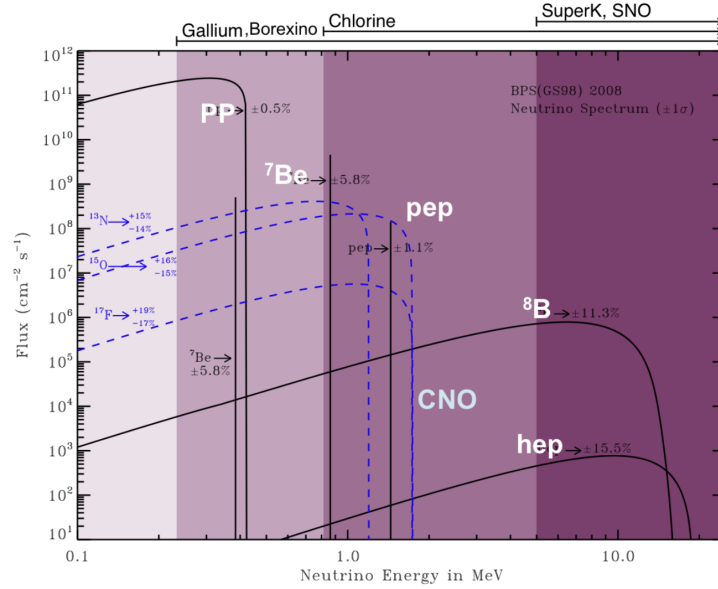
Figure 1.2: Energy spectra of neutrino flux from the *pp* and CNO chains as predicted by the Standard Solar Model. This figure is taken from Ref. [9].

decay process in the Sun,

$$^8B \rightarrow {}^8B^* + e^+ + \nu_e (\approx 10 \text{ MeV}). \qquad (1.28)$$

The detector was filled with C_2Cl_2. When a solar neutrino interacts with the Cl, an Ar atom is produced through the reaction,

$$\nu_e + {}^{37}Cl \rightarrow e^- + {}^{37}Ar. \qquad (1.29)$$
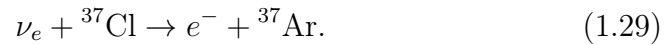
The number of observed ^{37}Ar was half less than the expected. The neutrino flux comes from the different chain of the reaction in the sun is shown in the Figure 1.2. The fusion of hydrogen nuclei into helium is

shown below,

$$p + p \rightarrow d + e^+ + \nu_e (\approx 0.3\text{MeV}). \tag{1.30}$$
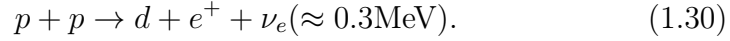
This reaction is studied by SAGE [16, 17] and GALLEX-GNO [18, 19], which are the radio chemical experiments. These neutrinos are studied using the neutrino interactions with the Gallium,

$$\nu_e + {}^{57}\text{Ga} \rightarrow e^- + {}^{71}\text{Ge}. \tag{1.31}$$
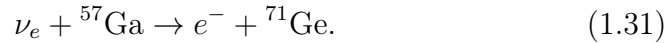
Both of the above experiments observed only half less neutrinos than the theoretical prediction. This problem is well known as the "Solar Neutrino Problem" and later it is identified to be a consequence of neutrino oscillation.

Sudbury Neutrino Observatory

The experiment confirmed the Standard Model solar neutrino flux prediction and attributing the solar neutrino problem to oscillations was Sudbury Neutrino Observatory (SNO), which turned on in 1999 [22, 23]. The SNO is a water Cherenkov detector located about 2 km underground in a mine in Sudbury, Ontario, Canada. The Detector consists of 1000 tons of pure heavy water surrounded by photomultiplier tubes 6010 meters water equivalent underground. The experiment measured the solar neutrino flux using the following three interactions.

$$\nu_e + d \rightarrow p + p + e^- \text{ (CC)}. \tag{1.32}$$

$$\nu_x + d \rightarrow p + n + \nu_x \text{ (NC)}. \tag{1.33}$$

$$\nu_x + e^- \rightarrow \nu_x + e^- \text{ (ES)}. \tag{1.34}$$

In the case of Elastic Scattering (ES) of electrons, the recoil electron direction is strongly correlated with the direction of the incident neutrino and the direction to the Sun. This ES reaction is sensitive to all neutrino flavors. For ν_e, the ES reaction has both charged and NC components, making the cross section for ν_es ≈ 6.5 times larger than that for ν_μs or ν_τs. The CC reaction also has an angular correlation with the Sun and has a cross section roughly ten times larger than the ES reaction for neutrinos within SNO's energy acceptance window. NC process has the advantage that it is equally sensitive to all neutrino flavors, and thus provides a direct measurement of the total active flux of ^{8}B neutrinos from the Sun.

1.6.2 Atmospheric Neutrino Oscillations

The evidence for neutrino oscillations are also reported with atmospheric neutrinos by other experiments like Super-Kamiokande [30]. Atmospheric neutrinos are produced when cosmic rays collide with particles in the atmosphere and decay, predominantly via the following channels.

$$\pi^{+/-} \rightarrow \mu^{+/-} + \nu_\mu/\bar{\nu}_\mu, \tag{1.35}$$

$$\mu^{+/-} \rightarrow e^{+/-} + \nu_e/\bar{\nu}_e + \nu_\mu/\bar{\nu}_\mu. \tag{1.36}$$

The ratio of muon family neutrinos to the electron family neutrinos are expected to be 2. In 1992, Kamiokande measured this ratio and found to be close to 1. Also the ratio seemed to be depended on the zenith angle, the ratio was closer to 2 for the neutrinos coming from directly overhead and dropping down as the zenith angle increased. Super-Kamiokande, improved the measurement in 1998 and gave a stronger evidence to the neutrino oscillations [30].

Super-Kamiokande

Super-Kamiokande experiment instrumented a 50 kton tank of pure water located at one kilometer underground with $\sim 11,000$ photo-multiplier tubes [30]. The experiment measured the flux of atmospheric electron and muon-neutrinos coming from both sides of the Earth, which gives a base-line length of ~ 10 km and $\sim 13,000$ km. The photomultiplier tubes collect the Cherenkov radiation light produced by the charged lepton products in a neutrino interaction. The result of the measurement was a deficit of the muon-neutrinos coming upward through the Earth, but no deficit was observed for the downward-going muon-neutrinos or electron-neutrinos as compared to the theoretical prediction. This was interpreted as the evidence of the oscillation of muon-neutrinos into tau neutrinos since no deficit or excess found in the electron neutrino population. The zenith angle distributions of $e-$like and $\mu-$like events for the Super-Kamiokande measurement are shown in Figure 1.3a. The data can also be binned in units of L/E which highlights the oscillation dip,

shown in Figure 1.3b.

(a)

(b)
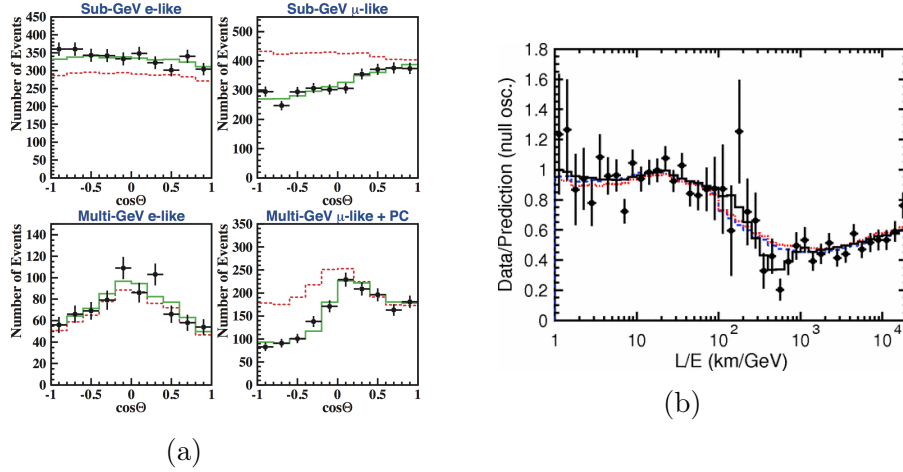
Figure 1.3: (a) Zenith angle distributions for e-like and μ-like events in Super-Kamiokande with visible energy < 1.33 GeV (sub-GeV) and > 1.33 GeV (multi-GeV). The dotted line shows the un-oscillated Monte Carlo prediction and the solid line is the best-fit under the two-flavor oscillation hypothesis. (b) Ratio of the data to the MC events without neutrino oscillation (points) as a function of the reconstructed L/E together with the best-fit expectation for 2-flavor $\nu_\mu \to \nu_\tau$ oscillations (solid line). The error bars are statistical only. Also shown are the best-fit expectation for neutrino decay (dashed line) and neutrino decoherence (dotted line).

The result was supported later by the evidence of the tau neutrino appearance. Super-K detector was not able to detect ν_τs in an event by event approach, also the minimum threshold energy for a ν_τ CC interaction is $\gtrsim 3.4$ GeV. A multivariate analysis on the zenith angle distributions of high energy events has shown 3.8 σ evidence of tau neutrino appearance.

1.6.3   Accelerator Experiments

Accelerator experiments use artificially produced neutrino (anti-neutrino) beam to study the oscillation parameters, which has an advantage that the desired energy neutrinos can be passed through detector for a fixed baseline length so that the experiment can measure the oscillation parameters precisely. The K2K (KEK-to-Kamioka) is the first accelerator based neutrino experiment, which produced a 1.3 GeV muon neutrino beam at KEK accelerator and passed it to the Super-Kamiokande, 250 km away. A near detector is also used in this experiment to study the flux. The experiment confirmed the oscillation parameters measured by Super-K [30].

Another accelerator based long-baseline (LBL) neutrino experiment called MINOS (Main Injector Neutrino Oscillation Search) started operating in 2005, used a ~ 3 GeV muon neutrino beam produced at Fermilab, Batavia, IL and send to a FD located in a mine at Soudan, MN, 735 km away from the source [32]. MINOS ND was located at Fermilab campus, 100 m underground from the Earth surface, 1 km away from the proton beam target. The far and near detectors are functionally identical tracking calorimeters consist of alternate plastic scintillators and steel orthogonal to beam direction. A toroidal magnetic field is used to find the charged muon momentum and energy. MINOS experiment collected data in both neutrino mode and anti-neutrino mode to study the atmospheric oscillation parameters and to test the ratio of the probabilities

of neutrino oscillations and antineutrino oscillations. The result slightly disfavors a maximum value of the θ_{23} and shows an agreement between the neutrinos and anti-neutrinos.

The first off-axis neutrino experiment, T2K (Tokai-to-Kamioka) started operating in 2010, has a base-line length of 295 km uses Super-K detector as the FD [29]. The detectors are located 2.5° off-axis from the muon neutrino beam produced at J-PARC main ring to produce a narrow-band energy beam at the oscillation maximum. The same method of keeping detectors in off-axis is also employed by NOvA experiment, which is 8° off-axis from NuMI beam at Fermilab [31]. T2K was primarily designed to measure θ_{13} using ν_e appearance but also used to measure the maximal value of θ_{23}.

1.6.4   Reactor Neutrino Oscillations

The neutrinos produced in the fission reactions in nuclear reactors are studied in reactor neutrino experiments. The main goal of these experiments are to measure the mixing angle θ_{13}. Double CHOOZ in France [33], Daya Bay in China [34], RENO in Korea ($\sim$ 1 km) [35]and Kam-LAND (LBL $\sim$ 100 km) [36] have reported the non-zero value of θ_{13} in 2012. All these three detectors contain Gadolinium doped liquid scintillator which produces a flash of light due to annihilation of a positron caused by the anti-neutrino absorption on a proton ($\bar{\nu}_e + p^+ \rightarrow e^+ + n^0$).

1.7   Sterile Neutrinos

There have been some experimental results that cannot be explained by oscillations based on the solar and atmospheric mass splitting scales, which could be explained by oscillations based on a larger scale mass splitting using a fourth flavor sterile neutrino. The search for sterile neutrinos is one of the active area of neutrino physics. These are the hypothetical particles still to be experimentally confirmed, if they exist. The first experimental evidence came from the Liquid Scintillator Neutrino Detector (LSND) in 1995 [70]. LSND reported a $\bar{\nu}_e$ excess in the antineutrino beam. MiniBooNE experiment at Fermilab also reported similar excess in 2010 [71].

1.7.1   LSND and MiniBooNE Results

Liquid Scintillator Neutrino Detector (LSND) is an accelerator based SBL experiment using neutrinos produced by LAMPF/LANSCE accelerator. LSND has observed a 3.5σ excess of $\bar{\nu}_e$ in the $\bar{\nu}_\mu$ beam. This excess corresponds to 87.9±22.4±6.0 events. The expectation with 100% transmutation of the $\bar{\nu}_\mu$ is about 33,300±3,300. This gives the $\bar{\nu}_e$ appearance probability as (0.264±0.067±0.045)%. The corresponding best-fit value is

$$(\sin^2 2\theta, \Delta m^2) = (0.003, 1.2 \text{ eV}^2). \tag{1.37}$$

The beam excess observed by LSND experiment is given in Figure 1.4.
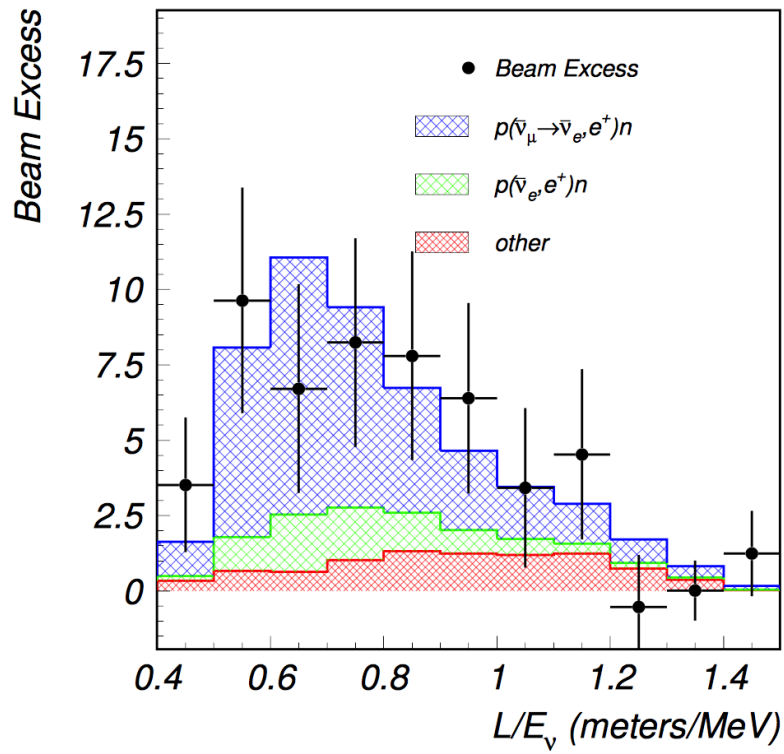
Figure 1.4: The excess observed by LSND experiment. The colored stacked histograms represents different background predictions and black dots are the excess seen in the real data. Figure is adapted from Ref. [70].
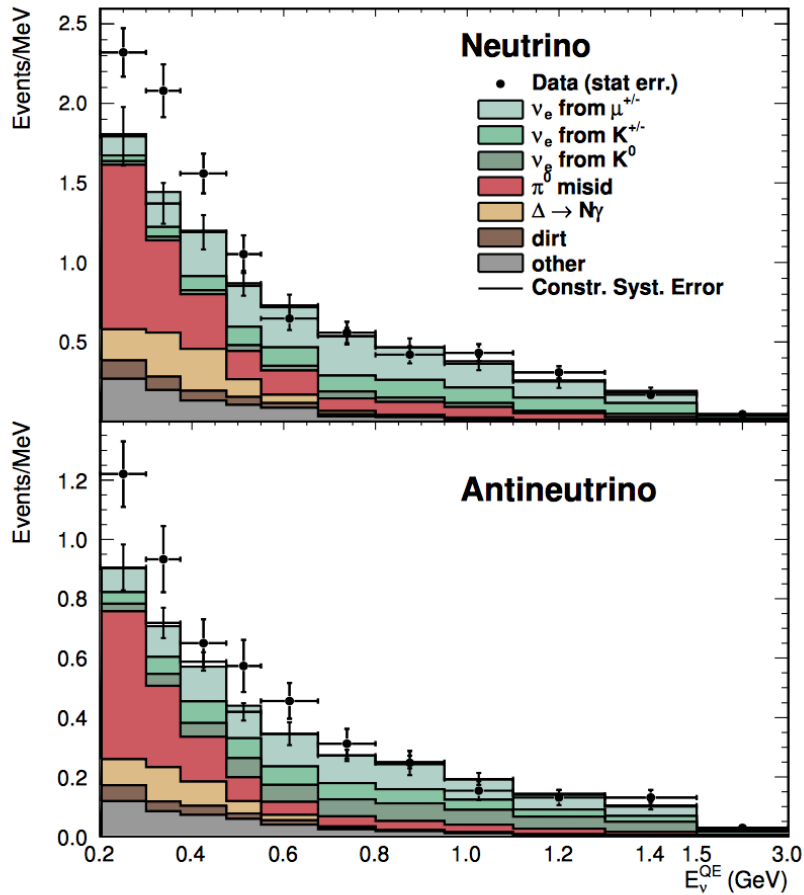
Figure 1.5: The excess observed by MiniBooNE experiment. The neutrino mode (top) and antineutrino mode (bottom) energy distributions for ν_e CCQE data points with statistical errors (black dots) and background histograms with systematic errors (colored stacked histograms). Figure is adapted from Ref. [71].

MiniBooNE experiment has observed the similar excess in both neutrino and anti-neutrino mode. It observed an excess of, in the anti-neutrino mode, 78.4 ± 28.5 events ($2.8\ \sigma$) in the energy range $200 < E_{QE} < 1250$ MeV and in the neutrino mode, 162.0 ± 47.8 events ($3.4\ \sigma$) in the same energy range. The corresponding best-fit value is,

$$(\sin^2 2\theta, \Delta m^2) = (0.002, 3.14\ \text{eV}^2). \tag{1.38}$$

The excess seen by MiniBooNE experiment is shown in Figure 1.5.

1.7.2 Sterile Neutrino Oscillations

The analysis presented in this thesis uses a 3+1 oscillation model approximated to a two-flavor oscillation model, which includes a fourth flavor hypothetical neutrino called the sterile neutrino (ν_s). That adds and additional mass state (ν_4) and hence the PMNS matrix becomes a 4×4 matrix. The ν_μs produced in the NuMI beam travels a maximum distance of 1 km to pass through the NOvA ND and if these ν_μs oscillate to ν_τs within that distance, the active neutrinos (ν_μ, ν_e, ν_τ) to sterile neutrino mixing happens in a larger mass splitting. We do not expect any significant standard 3 flavor neutrino oscillations within that distance. Thus we use a 3+1 oscillation model, the minimal sterile neutrino oscillation model, which can be approximated to a 2 flavor neutrino oscillation model within SBL limit.

$$
\begin{pmatrix} \nu_e \\ \nu_\mu \\ \nu_\tau \\ \nu_s \end{pmatrix} = \begin{pmatrix} U_{e1} & U_{e2} & U_{e3} & U_{e4} \\ U_{\mu1} & U_{\mu2} & U_{\mu3} & U_{\mu4} \\ U_{\tau1} & U_{\tau2} & U_{\tau3} & U_{\tau4} \\ U_{s1} & U_{s2} & U_{s3} & U_{s4} \end{pmatrix} \begin{pmatrix} \nu_1 \\ \nu_2 \\ \nu_3 \\ \nu_4 \end{pmatrix}. \tag{1.39}
$$

where ν_s and ν_4 respectively are the flavor and mass eigen states of sterile neutrino, and $U_{\alpha i}$ (here $\alpha = e, \mu, \tau, s$ and i = 1, 2, 3, 4) represents the mixing between active and sterile neutrino. After applying the SBL approximations, one can write the 2 flavor oscillation probability as shown below: The oscillation probability for $\nu_\mu(\bar{\nu}_\mu) \to \nu_\tau(\bar{\nu}_\mu)$ oscillation can be expressed as,

$$
P^{\text{SBL},3+1}_{\nu_\mu(\bar{\nu}_\mu) \to \nu_\tau(\bar{\nu}_\mu)} = \sin^2 2\theta_{\mu\tau} \sin^2 \frac{\Delta m^2_{41} L}{4E}, \tag{1.40}
$$

where $\sin^2 2\theta_{\mu\tau} \equiv 4|U_{\mu4}|^2|U_{\tau4}|^2 = \cos^4 \theta_{14} \sin^2 2\theta_{24} \sin^2 \theta_{34}$.

Similarly, $\nu_\mu(\bar{\nu}_\mu) \to \nu_\mu(\bar{\nu}_\mu)$ disappearance probability from Equation (1.17) can be written as,

$$
\begin{aligned}
P^{\text{SBL},3+1}_{\nu_\mu(\bar{\nu}_\mu) \to \nu_\mu(\bar{\nu}_\mu)} &= 1 - 4|U_{\mu4}|^2(1 - |U_{\mu4}|^2)\sin^2 \frac{\Delta m^2_{41} L}{4E} & (1.41) \\
&= 1 - \sin^2 2\theta_{\mu\mu} \sin^2 \frac{\Delta m^2_{41} L}{4E}. & (1.42)
\end{aligned}
$$

where $\sin^2 2\theta_{\mu\mu} \equiv 4|U_{\mu4}|^2(1-|U_{\mu4}|^2)$ and $\sin^2 2\theta_{\mu\mu} = \cos^2 \theta_{14} \sin^2 \theta_{24}$.

1.7.3 Other Sterile Neutrino Oscillation Searches

The third anomaly was observed by reactor neutrino experiments in the predicted reactor spectra. The KARMEN [37], ICARUS [38] and NO-MAD [80] experiments also searched for $\nu_\mu \rightarrow \nu_e$ appearance oscillations, but not with the sensitivity to fully exclude the MiniBooNE and LSND signals. CCFR [24], CDHS [25], MINOS, MINOS+, and Sci-BooNE [26]/MiniBooNE [28] are some of the other two detector experiments tried to probe into sterile neutrino oscillations. The radio-chemical Gallium experiments GALLEX [19] and SAGE [17] observed a deficiency in the anti-electron neutrino interaction rate. These results can also be explained by introducing one or more additional sterile neutrinos. The NEOS reactor experiment at Hanbit nuclear power complex is also searching for sterile neutrinos, which is situated 24 m from the reactor core, and has observed no evidence for the sterile neutrinos [27].

Chapter 2

A Brief History of Tau Neutrinos

After the discovery of the τ lepton in 1975 [41], it was expected that a neutral partner also must exist. The precision measurements of the invisible part of the decay width of the Z boson at LEP provided strong evidence that there are only three neutrino states with $m_\nu < \frac{1}{2}m_Z$ [12]. Indirect ν_τ evidence was collected at different collider experiments [42–44] and finally, ν_τs were successfully detected by the DONUT (Direct Observation of the NU Tau, E872) experiment at Fermilab in 1997 [39]. A source of charmed mesons produced using the protons from the Tevatron at Fermilab was used for the production of tau neutrinos detected by this experiment. The direct detection of the ν_τ CC interactions was performed in this experiment by identifying the τ lepton as the only lepton created at the interaction vertex. The experiment reported 12 instances of a neutrino interacting with an atomic nucleus to produce a tau lepton,

which is the signature of a tau neutrino. Another experiment, OPERA was designed with emulsion technology similar to the DONUT experiment, to discover ν_τ appearance in a ν_μ beam [45]. OPERA succeeded in discovering ν_τ appearance [46]. However, since the atmospheric mass splitting is $\Delta m^2_{31} = 2.5 \times 10^3$ eV^2, the experiment operated 700 km from the beam source, and the beam had a peak energy of 20 GeV, the appearance was suppressed by a factor of 0.01, and only 5 ν_τ CC events were observed.

2.1   DONUT Experiment

The DONUT experiment used the neutrinos produced by directing 800 GeV/c protons from the Fermilab Tevatron to a 1m Tungsten target [39, 40]. The detectors consist of a scintillation counter veto wall, the hybrid emulsion target, trigger hodoscopes and a charged particle spectroscope. The hybrid emulsion target provides a very good spacial resolution of ~ 1 μm which is well fit to detect the τ decays. The experiment also measured the charged current tau neutrino interaction cross section per nucleon based on the direct observation of ν_τ CC interactions. A graphical representation of the DONUT detector is shown in Figure 2.1.

DONUT Detector

Identification of muons coming from tau decay

Calorimeter determines energy of decay products

Drift chambers record decay particle tracks

Magnet spreads tracks of charged particles

Emulsion target with planes of scintillation fibers

Steel shield to block particles other than neutrinos

15 meters (about 50 feet)

Neutrino beam

DONUT Detector for direct observation of tau neutrinos (ν_τ)

Figure 2.1: A graphical representation of the DONUT detector. Figure is adapted from [78].

2.2   OPERA Experiment

The Oscillation Project with Emulsion-tRacking Apparatus (OPERA) is a collaboration between CERN in Geneva, Switzerland, and the Laboratori Nazionali del Gran Sasso (LNGS) in Gran Sasso, Italy. OPERA uses the CERN Neutrinos to Gran Sasso (CNGS) neutrino beam. The protons produced at Super Proton Synchrotron (SPS) at CERN being directed to a carbon target to produce pions and kaons. These particles decay to muons and neutrinos. OPERA collected data up to 3rd December 2012. The experiment detected five tau neutrinos in total. The τ's resulting from the ν_τ CC interactions are observed in "brick" weighs 8.3 kg each, of photographic films and nuclear emulsion interleaved with lead sheets. Two OPERA super-modules contain 150,000 bricks arranged into parallel walls interleaved with plastic scintillator counters. Each super-module is followed by a magnetic spectrometer, which helps to identify momentum and charge of the particles inside detector. A neutrino interaction and its corresponding brick are tagged in real time by the scintillators and spectrometers. These bricks are extracted from the walls asynchronously with respect to the beam for film development, scanning and identifying the τ decay and its products.
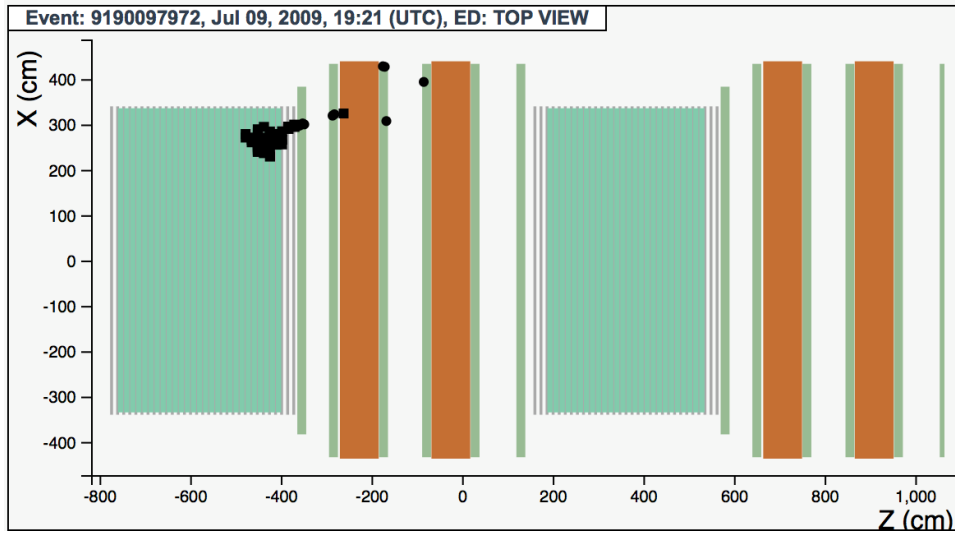
Figure 2.2: A ν_τ CC interaction recorded in OPERA detector on July 9, 2009. Figure is adapted from Ref. [79].
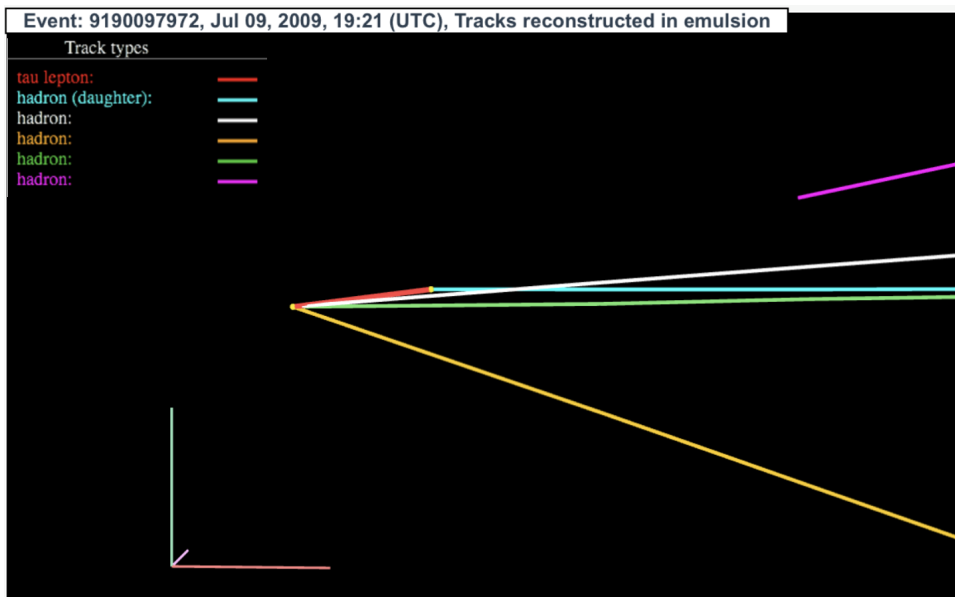
Figure 2.3: When reconstructed the particle trajectories of a ν_τ CC interaction recorded in OPERA detector on July 9, 2009. This is the same event shown in Figure 2.3. The τ lepton is shown in red color. Figure is adapted from Ref. [79].

Decay Mode	Branching(%)
$\tau^- \to e^- \bar{\nu}_e \nu_\tau$	17.8
$\tau^- \to \mu^- \bar{\nu}_\mu \nu_\tau$	17.4
$\tau^- \to h^- \nu_\tau$	11.5
$\tau^- \to h^- \pi^0 \nu_\tau$	26.0
$\tau^- \to h^- \pi^0 \pi^0 \nu_\tau$	9.5
$\tau^- \to h^- h^+ h^- \nu_\tau$	9.8
$\tau^- \to h^- h^+ h^- \pi^0 \nu_\tau$	4.8
Other modes with hadrons	3.2
All modes containing hadrons	**64.8**

Table 2.1: Approximate branching fractions (%) of different τ decay modes, $h^{(+/-)}$ represents a charged hadron (either a pion or a kaon).

2.3 τ Decay Modes and Branching

The τ lepton has a lifetime of 2.9×10^{-13} s and a mass of 1776.82 MeV. As the life time is very short, the range of τ is mainly set by their decay length, which is too small to identify in most of the neutrino detectors. The τ meson is the only lepton that can decay into hadrons, the other leptons do not have the necessary mass to decay to hadrons. τ decays hadronically $\sim 64.79\%$ of the time and $\sim 17.82\%$ into a ν_τ, e and $\bar{\nu}_e$ and $\sim 17.39\%$ of the time into a ν_τ, μ and $\bar{\nu}_\mu$. The branching fractions of τ decays are given in Table 2.1. The main challenge in identifying hadronic τ decays in NOvA is to distinguish it from huge NC background events, as they differ only by either one or three additional hadrons coming from τ decay. Also it should be noted that NOvA detector resolution is not enough to identify the τ particle. However it is possible to identify the decay products coming out of a τ lepton.

2.4 Anomalous τ Neutrino Appearance Searches

NOMAD experiment [80] and CHORUS experiment [82] are the two other competitive experiments searched for the anomalous ν_τ appearance using high energy neutrino beams. Both experiments found no evidence for the ν_τ appearance.

2.4.1 NOMAD Experiment

The NOMAD [80] experiment was designed in 1991 to search for ν_τ appearance from neutrino oscillations in the CERN wide-band neutrino beam produced by a 450 GeV proton synchrotron. The hot dark matter hypothesis predicted a ν_τ mass in the range of 1–10 eV, thus the main aim of the experiment was to search for $\nu_\mu \rightarrow \nu_\tau$ oscillations by searching for ν_τ CC interactions and observing the production of the lepton through its various decay modes. The experiment is sensitive to mass squared differences, $\Delta m^2 > 1$ eV^2. In the two-flavor oscillation formalism this result excludes a region of the $\nu_\mu \rightarrow \nu_\tau$ oscillation parameters which limits $\sin^2 2\theta_{\mu\tau}$ at high Δm^2 to values smaller than 3.3×10^{-4} at 90% C.L. and to values smaller than 0.7 eV^2 at $\sin^2 2\theta_{\mu\tau} = 1$ [80].

2.4.2   CHORUS Experiment

The CHORUS [82] experiment was designed to search for SBL $\nu_\mu \to \nu_\tau$ oscillations through the observation of ν_τ CC interactions, $\nu_\tau + \mathrm{N} \to \tau + $ $-\mathrm{X}$ followed by the decay of the τ lepton, directly observed in a nuclear emulsion target. CHORUS used the same SPS wide-band neutrino beam used by NOMAD. CHORUS is a hybrid detector which consists of an emulsion target followed by a real time electronic detector. CHORUS made use of the spatial resolution offered by nuclear emulsion which is of the order of 10 μm with a hit density of 300/nm, which is ideal for the short-lived particle identification.

In the two-flavor oscillation formalism this result excludes a region of the $\nu_\mu \to \nu_\tau$ oscillation parameters which limits the maximum mixing for $\Delta m^2 > 0.8$ eV^2 at 90% C.L. and in the large Δm^2 limit $\nu_\mu \to \nu_\tau$ oscillations are excluded for $\sin^2 2\theta_{\mu\tau} > 9.2 \times 10^4$ [81,82]. The final results from NOMAD and CHORUS experiments represented in the (Δm^2, $\sin^2 2\theta$) plane are shown in Figure 2.4.
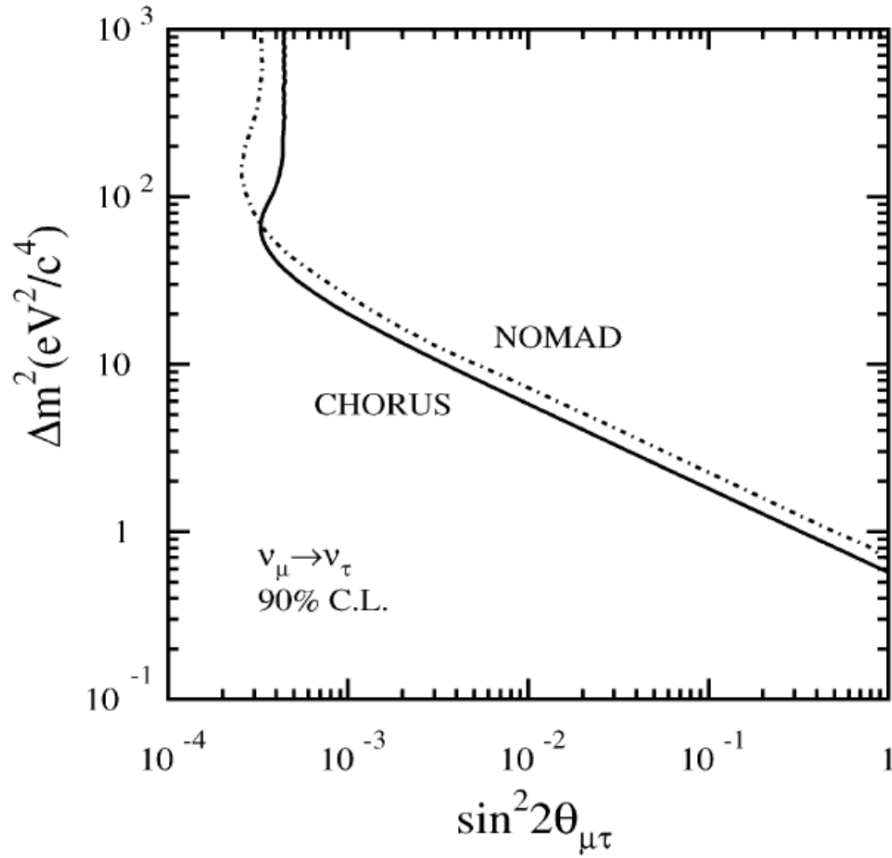
Figure 2.4: Experimental results from CHORUS and NOMAD experiments represented in the $(\Delta m^2, \sin^2 2\theta)$ plane, the figure is adapted from Ref. [81].

Chapter 3

The NOvA Experiment

The NuMI Off-axis ν_e Appearance (NOvA) experiment uses high intensity Neutrinos at the Main Injector (NuMI) which was originally built for the Main Injector Neutrino Oscillation Search (MINOS) experiment and has undergone upgrades for the NOvA experiment. The NOvA experiment consists of two finely segmented functionally identical liquid scintillator detectors, a ND which is located at Fermilab in Batavia, IL, and a FD located at Ash River, MN. Both ND and FD are located 14 mrad off-axis from the NuMI beam line as it provides an approximately mono-energetic beam peaks at an energy of 2 GeV, which helps to a precise measurement of θ_{13}. Both detectors consist of extruded cells of PVC plastic filled with liquid scintillator to form a three dimensional tracking calorimeter. The PVC extrusions are stacked in alternating horizontal and vertical planes to provide three dimensional tracking of the particles. The cells are coated with titanium dioxide, TiO_2, which is 90% reflective for 430 nm wavelength light. The radiation length for an electromagnetic shower in liquid scintillator is 41 cm with a Moliere radius of 10.5 cm

and the mean free path for photon conversion is 53 cm.

3.1   NuMI Beam

The NuMI beam is generated by protons accelerated to 120 GeV in the Main Injector at Fermilab. A schematic of the accelerator complex at Fermilab with main injector is shown in Figure 3.1. These protons are sent to a graphite target producing a shower of hadrons, the pions and kaons which decay into leptons. The pions decay yield muons and muon neutrinos as follows:

$$\pi^+ \rightarrow \mu^+ + \nu_\mu,$$
$$\pi^- \rightarrow \mu^- + \bar{\nu}_\mu, \tag{3.1}$$

and the kaons decay to yield muons and muon neutrinos as:

$$K^+ \rightarrow \mu^+ + \nu_\mu. \tag{3.2}$$

3.2   Beam Flux and Kinematics

The NOvA detectors are 14.6 mrad off-axis to NuMI neutrino beam at Fermilab to maximize the sensitivity to the $\nu_\mu \rightarrow \nu_e$ oscillations. The knowledge about the kinematics of pions and kaons are utilized to pro-

Fermilab Accelerator Complex
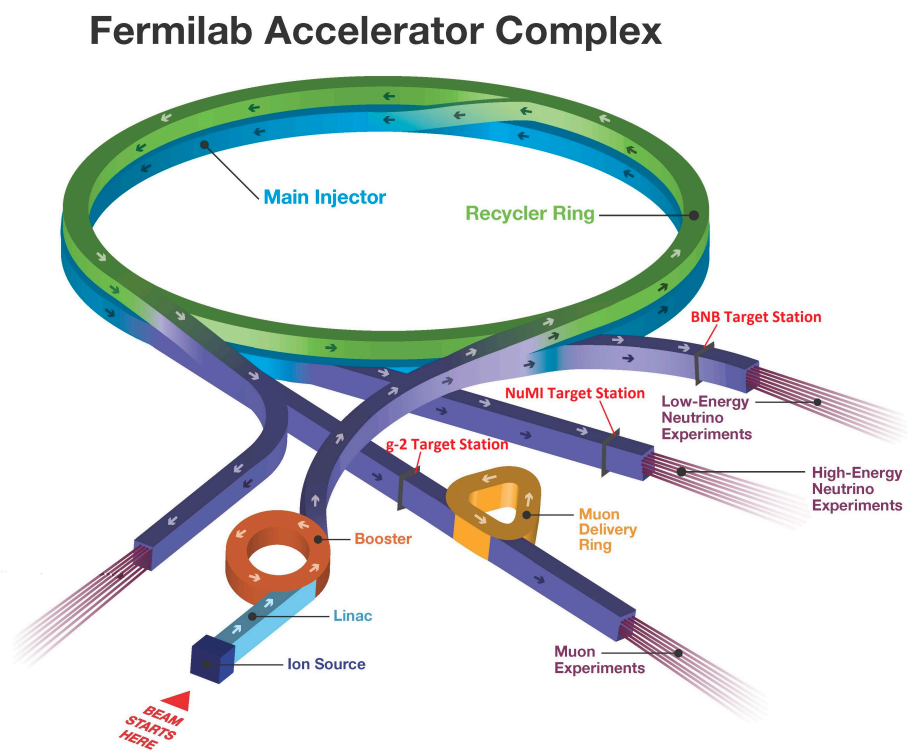
Figure 3.1: Schematic of the Fermilab accelerator complex, upgraded for NOvA.
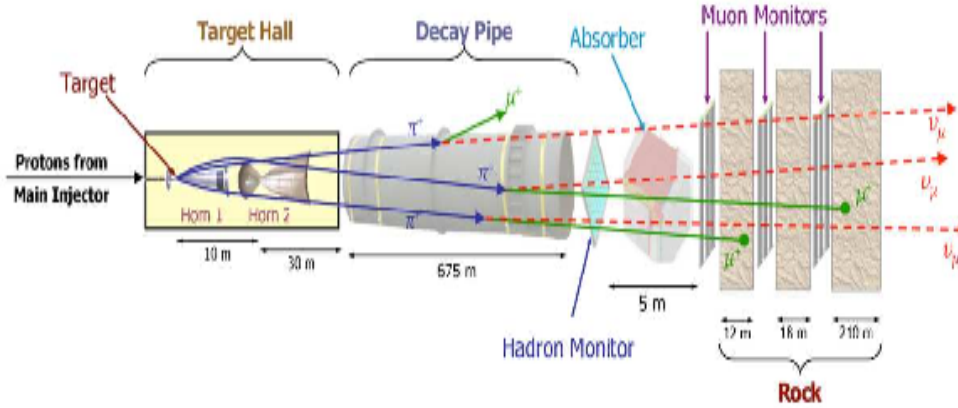
Figure 3.2: Schematic of the NuMI beamline [47].

duce the mono-energetic neutrinos. The pions and kaons decay isotropically in the rest frame producing the mono-energetic neutrinos. The schematic of the NuMI neutrino beam production is shown in Figure 3.2. The protons are sent to a graphite target of approximately 1 m length. The carbon-proton interactions produce secondary mesons which are focused using two magnetic horns. These mesons decay in flight to produce the neutrinos in a volume of 675 m long pipe. The magnetic horns polarity can be adjusted to focus any one of the opposite sign hadrons at a given time to produce either neutrinos or anti-neutrinos.

3.3   Off-axis Detectors

NOvA detectors are located at 14.6 mrad off-axis from the NuMI beamline which greatly affects the neutrino energy spectrum. The main decay mode for the charged pions (99.99%) and kaons (63.56%) are the two
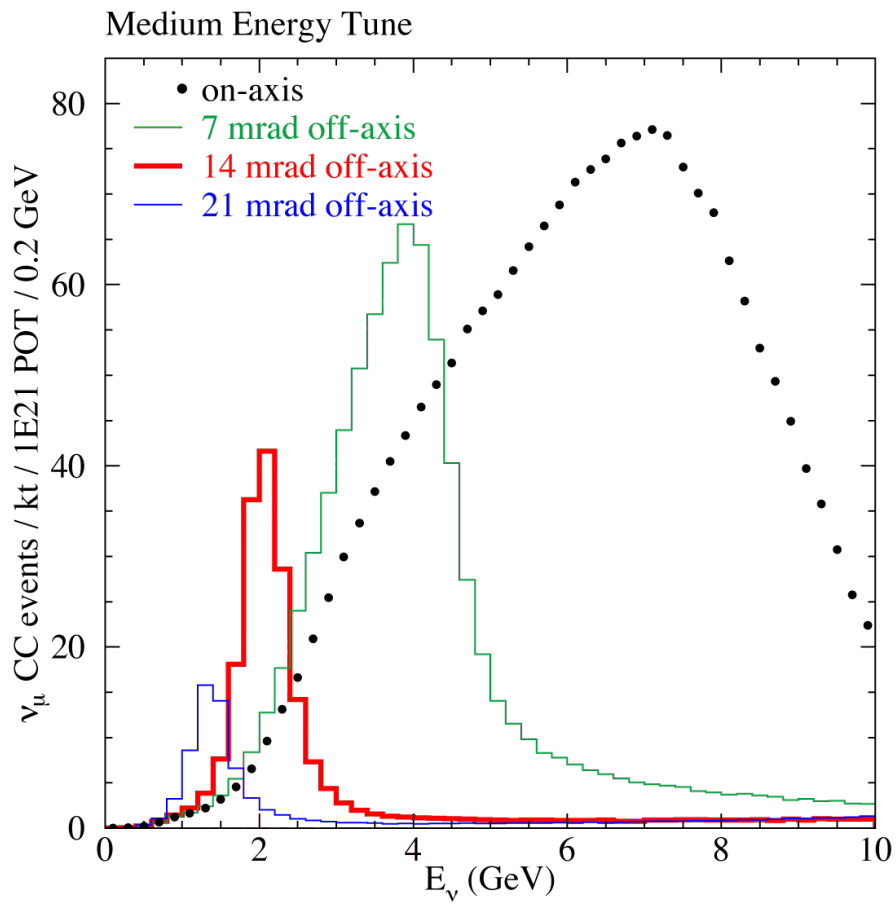
Figure 3.3: Simulated neutrino energy spectra at the NOVA far detector baseline of 810 km. The off-axis location of NOvA gives a sharp energy peak at 2 GeV.

Decay	Channel	Branching Ratio (%)
1	$\pi^{\pm} \to \mu^{\pm} + \nu_\mu(\bar{\nu}_\mu)$	99.99
2	$\pi^{\pm} \to e^{\pm} + \nu_e(\bar{\nu}_e)$	0.01
3	$K^{\pm} \to \mu^{\pm} + \nu_\mu(\bar{\nu}_\mu)$	63.55
4	$K^{\pm} \to \pi^0 + e^{\pm} + \nu_e(\bar{\nu}_e)$	5.07
5	$K^{\pm} \to \pi^0 + \mu^{\pm} + \nu_\mu(\bar{\nu}_\mu)$	3.35
6	$K^{\pm} \to \pi^{\pm} + e^{\mp} + \nu_e$	40.55
7	$K^{\pm} \to \pi^{\pm} + \mu^{\mp} + \nu_\mu$	27.04
8	$\mu^{\pm} \to e^{\pm} + \nu_e(\bar{\nu}_e) + \bar{\nu}_\mu(\nu_\mu)$	100.00

Table 3.1: Main decay modes and the branching fractions of charged pions, charged kaons, neutral kaons and muons to neutrinos.
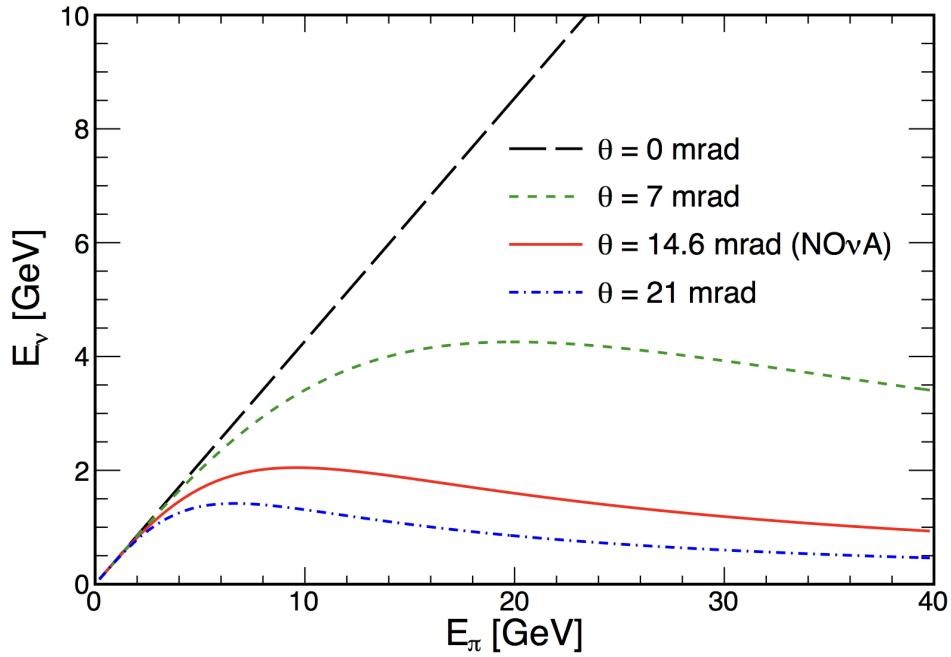
Figure 3.4: Simulated pion energy vs. neutrino energy spectra at different off-axis angles from NuMI beamline.

body decay to a muon and muon-neutrino. The main decay modes and the branching fractions of the pions, kaons and muons to neutrinos are given in Table 3.1. In the center of mass frame of mesons, it is a deterministic, isolated decay. However in the lab frame it is a highly boosted decay resulting in the following flux and energy spectrum for the detector of an area A and a distance L from the decay point. The true energy distribution of neutrinos at different off-axis angles from NuMI beamline is given in Figure 3.3. The correlation between the true pion energy and the outgoing neutrino energy for different off-axis angles are shown in Eq. (3.4) and in the corresponding Figure 3.4. The red curve shows the energy spectrum at 14.6 mrad off-axis, which is used by NOvA experiment.

$$F = \left(\frac{2\gamma}{1 + \gamma^2 \theta^2} \right)^2 \frac{A}{4\pi z^2}, \tag{3.3}$$

$$E_\nu = \frac{0.43 E_\pi}{1 + \gamma^2 \theta^2}. \tag{3.4}$$

3.4   The NOvA Detector Design

A PVC rectangular structure filled with liquid scintillator is the basic unit of the NOvA detectors. Each detector module is formed using 32 such cells and are equipped with 32 Avalanche Photo Diodes (APD) and one Front End Board (FEB). These modules are glued to make planes and the planes form blocks and blocks form diblocks. All the FEBs are connected to a Data Concentrator Modules (DCM). Every cell has a
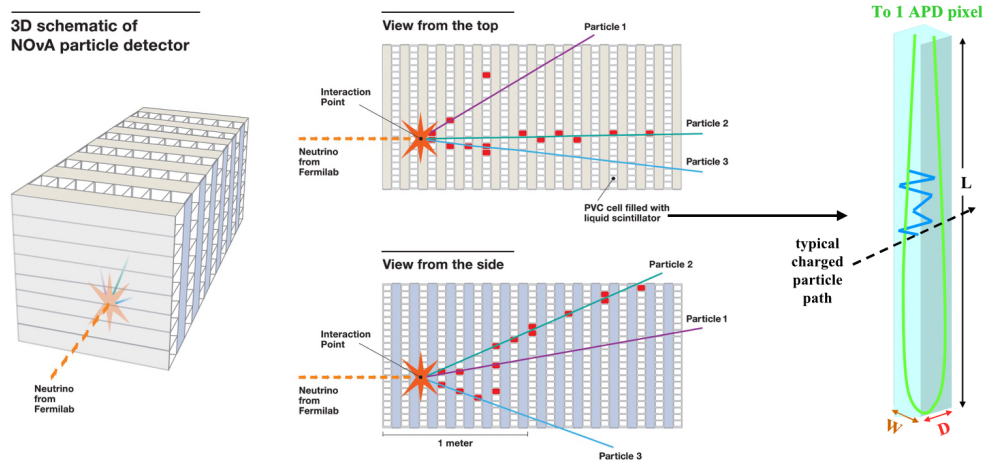
Figure 3.5: A cut-out of the NOvA detectors and a cell indicating the orthogonal arrangement of cells in adjacent planes.

wavelength shifting fiber, which has two ends connected to two different APDs. When particle travels through the detector, the scintillation light is produced and is collected by these wavelength shifting (WLS) fibers and fed to APDs. The APD converts the light signal to electrical signal and then digitized by the FEBs and then sent to the Data Acquisition (DAQ) system. The DAQ system stores the light hit in each cell with a time stamp and is stored to make useful data for various analyses. This chapter draws heavily from the NOvA Technical Design Report [48].

3.4.1   The NOvA Unit Cell

The NOvA detectors consist of rectangular PVC cells with cross section ~ 4 cm $\times$ 6 cm extruded to make a single layer which forms a plane of

the detector. The adjacent planes are arranged orthogonal to each other to provide 3D reconstruction of the particle positions as shown in Figure 3.5. Each cell is filled with the liquid scintillator in which a loop of WLS optic fiber is immersed to collect the scintillation light produced when a particle interacts in the detector. The light from 32 such cells is read out by 32 pixels of an APD module. The inner volume of the cells are 3.6 cm wide and 5.6 cm deep which defines the granularity of the NOvA detectors. A cell is 15.5 m long in the FD and 4 m long in the ND. There are 384 cells per plane in the FD, and 48 in ND. A schematic of the NOvA detector structure and the unit cell is given in Figure 3.5.

3.4.2   Liquid Scintillator

The constituents of the liquid scintillator by mass are 94.63% mineral oil, 5.23% pseudocumene (scintillator), 0.14% PPO (wavelength shifter), 0.0016% bis-MSB (wavelength shifter), 0.001% Stadis-425 (anti-static) and 0.001% Vitamin E (anti-oxidant). When a neutrino interaction happens the scintillation light is produced in the near ultraviolet and shifts it to the visible region of 380–450 nm. A 0.7 mm double-clad Kuraray WLS fiber is looped down the entire cell length in a U shape, both ends of which are read out by a single photo-detector which improves collection efficiency. The wavelength-shifting fiber absorbs light in the violet-blue range and emits in the blue-green (450–600 nm) range. Out of the total mass of the NOvA detectors, almost 65% is in the liquid scintillator [53].

3.4.3   Optical Fiber

The optical fiber used in the detectors contains WLS agents. The Y11 dye in the fiber is excited by the violet light ($\sim$ 425 nm) emitted by the NOvA scintillator. The dye emits blue-green light in the wave-length range 450-650 nm. Due to the overlap between the absorption and emission spectrum of the dye, the wavelengths below 520 nm are severely attenuated in the fiber. The fiber core is made of polystyrene, which has a refractive index of 1.59. The cladding include an inner acrylic cladding (n = 1.49) and an outer fluorinated-polymer cladding (n = 1.42). The inner cladding improves the acceptance angle for total internal reflection of light in the core and also provides an additional layer of protection for the core. In the NOvA cells, the fiber is placed in a loop, with its plane oriented along the diagonal of the cell cross section, like the green line shown in the right side of the Figure 3.5. The bending radius of the fiber has to be as little as 3 cm. For this reason the fiber has a radius of 7 mm. The looped fiber provides twice the light-collection fraction than a single strand. It is also more efficient than two separate strands of fiber because it does not suffer from imperfect reflection from the fiber ends. The two ends of the fiber in a single cell terminate at one pixel of a 32 pixel APD array.

3.4.4 Avalanche Photodiode

An APD is a highly sensitive semiconductor diode that exploits the photoelectric effect to convert light to electric signal through avalanche multiplication. With a high reverse bias voltage, the electron and hole pairs excited by photons are accelerated in the strong internal electric field and these electrons strike other electrons and cause them to be freed. This process is repeated, which is called impact-ionization, which leads to a significant amplification of the photo-current.

APDs are operated at a low temperature of -15°C to minimize the dark current noise (the current produced by thermal electrons even in the absence of a light signal). Each APD carries a thermoelectric cooler (TEC) to maintain this operational temperature. A water cooling system has been designed which circulates water chilled to 15°C to keep the APDs in the operating voltage. To reduce the surface current due to moister or dust particles, the surface of the APD is coated with Parylene, a transparent epoxy, and it is ventilated with dry-air which helps to prevent accumulation of moisture. A schematic of the APD and FEB electronics are shown in Figure 3.6. The APD performance is further degraded by an excess noise factor generated due to the current fluctuations. This excess noise is a function of the gain and the carrier ionization ratio, κ, which is defined as the ratio of ionization probabilities of holes to electrons and is about 1:50 in NOvA APDs. The APDs are operated at a voltage close to 425 V to produce a gain of ~ 100. The excess noise
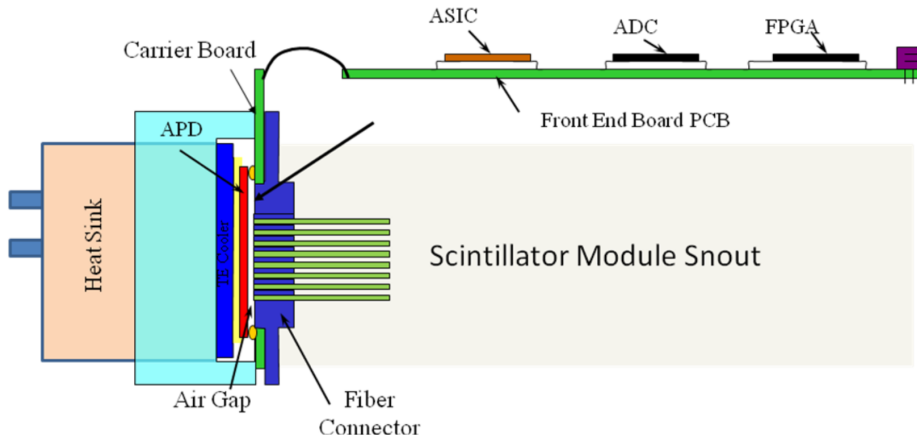
Figure 3.6: Schematic of the APD and front-end electronics.

factor is well-modeled and are included in the NOvA simulation. The operational conditions have been designed to produce a signal to noise ratio of 10:1 for majority of the APDs.

3.4.5   PVC Modules

PVC cells are extruded in groups of 16 cells for easy and reliable extrusion, with a minimum PVC stress and maximum light reflectivity. The outer extrusion walls are 4.8 mm thick and the inner walls between cells are 3.3 mm thick and the corners of the cells are rounded or scalloped to reduce the stress concentration at the corners, which makes the wall thickness constant and helps in uniform cooling in the extrusion process. Each of these 16 cell two extrusions are glued together to form 32 cell extrusions. Each cell has a loop of optical fiber. The end of the loop is mounted on a plastic ring, with a groove to hold the fiber in place,

which is aligned along the diagonal of the cell's cross section. The high light-yield of NOvA is in part due to the reflectivity of the PVC modules, which is boosted by adding TiO_2 to it and 90% reflectivity is attained at the peak wavelength (430 nm) of scintillator emission. Adhesive epoxies that are inert to the liquid scintillator were used for the assembly of the extrusions. A schematic of the PVC modules is shown in Figure 3.7.

3.5 The Far Detector

Each far detector plane consists of twelve 32 cell modules assembled in units of blocks glued together in alternating horizontal and vertical planes. Fully assembled detector consists of 896 planes and 28 such blocks in total. After filling the liquid scintillator in each cell, the modules are outfitted with APDs and FEBs. A front view of NOvA far detector is shown in Figure 3.8.

3.6 The Near Detector

Near Detector is functionally identical to FD. The ND consists of 3 modules per plane and 24 planes per block, half of which are horizontal and the remaining half in vertical positioning, 8 such blocks in total. In addition to that, the downstream end of the ND has a muon catcher re-
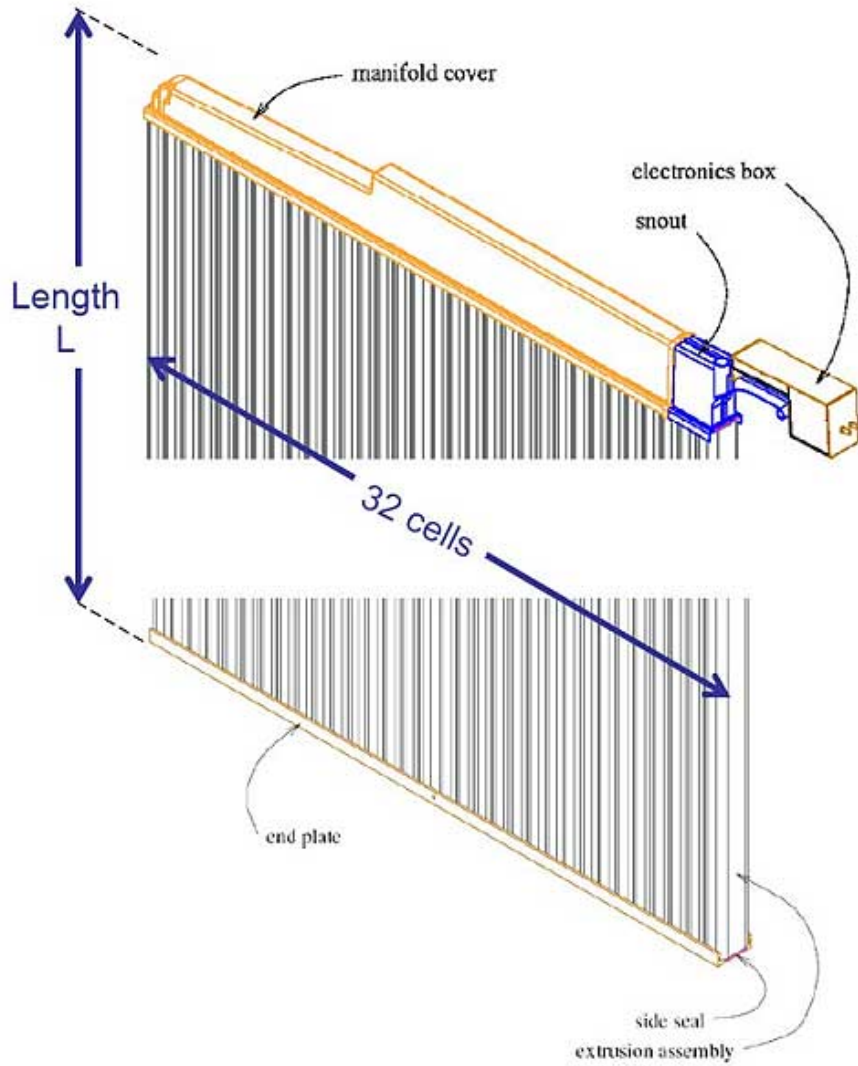
Figure 3.7: Schematic of the PVC module.

Figure 3.8: NOvA far detector. The beam comes from the back of the photograph and out of the page. The red and yellow structure is a pivoter used, not a part of the detector.

Figure 3.9: The NOvA ND view from where the beam enters the detector. A person is seen on the right for the scale.

gion which contains 10 planes of steel of thickness 4.03 inches which has a height of 2 modules and width of 3 modules interspersed with three vertical and two horizontal PVC planes for detecting muons. The total number of the active liquid scintillator filled PVC planes in the ND is 214. The NOvA ND view from the beam downstream is shown in Figure 3.9.

3.7   Data Acquisition and Triggering System

NOvA FD is located 810 km away from Fermilab which makes difficulties in the triggering of readout in advance of an NuMI spill. Using an activity

based trigger to record the NuMI data is more difficult in the FD since it is exposed to a very large cosmic flux of frequency 120 Hz. The detectors are operated in continuous readout mode which minimizes these issues.

3.7.1   DAQ System

A Front-end Electronics Board (FEB) receives the pulses from the 32 channels of each APD module, which time stamps and shape the signal. Data from 64 such FEBs are aggregated by a Data Concentrator Module (DCM), which is a custom built computer. Each DCM arrange the data into 50 μs long units called micro-slices. These micro-slices are aggregated by an event builder module in DCM into 5 ms chunks or milli-slices. Duration of these aggregation units are optimized for the transmission over the internal bus and Ethernet. These 5 ms milli-slices are dispatched by DCMs to a pool of buffer nodes such that these pulses from DCMs reach in the same buffer node.

A single DCM readouts two consecutive modules in 32 consecutive planes from the same view. Since each block contains only 16 modules per view, a DCM encompasses two blocks which is called a diblock and the readout is organized in units of diblocks in NOvA.

3.7.2   Clock and Triggering

The readout components are synchronized to an external wall clock through the timing chain at the head of which is a Master Timing Distribution Unit (MTDU). A high precision GPS receiver is connected to MTDU to drive the master clock. There are slave TDUs (STDU) synchronize each diblock, which are driven by the MTDU. All channels are synchronized to each other so that the channels which measure an above threshold energy deposit record a hit with the time stamp. MTDU is connected to the accelerator network at Fermilab, which decodes accelerator time stamp into NOvA time stamp, when a beam spill occurs [49]. The spill is transmitted to both FD and ND at the same time, after applying the corrections to include the time of flight of neutrinos in the Earth. When a spill is received the buffer nodes search the milli-slices for the hits that are happened in the time window and the selected hits are stored in the permanent storage. Figure 3.10 shows schematic of the distributive timing system deployed at the ND.

3.7.3   Readout

The ND records multiple neutrino interactions per spill due to its proximity to the NuMI beam. The separation between the hits requires a more timing resolution to distinguish the different neutrino interactions. The FEB in which an APD is mounted houses an Application Specific
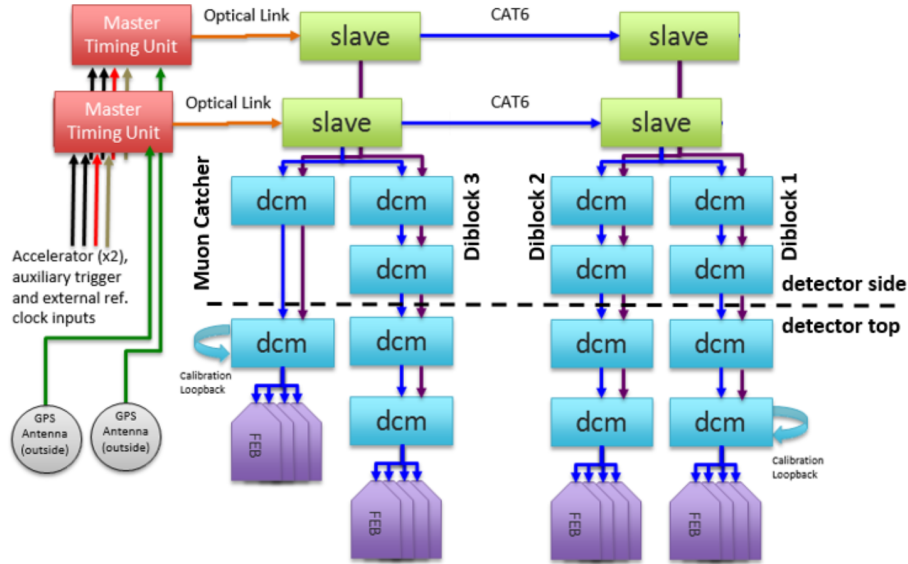
Figure 3.10: Schematic of the distributive timing deployed in the ND.

Integrated Circuit (ASIC) which shapes the signal and an Analogue to Digital Converter (ADC), which convert analogue signal to a digital signal. ASIC uses a 2:1 multiplexing so that each of 32 pixels of an APD gets 8 MHz sampling frequency, which helps to distinguish the hits from different neutrino interactions. However in the FD, only one neutrino interaction is expected at a time and requires only a less sampling rate, which is set to be 2 MHz. Hence the FD FEBs are driven by a 16 MHz clock and the ASIC uses 8:1 multiplexing to readout the 32 channels of an APD. A pulse in the ND is shaped with a rise-time of 140 ns and a fall time of 4500 ns and the far detector ASIC shapes the pulse with a 460 ns rise-time and a 7000 ns fall-time. These shaping parameters are calculated and fixed from measuring the APD leakage current and shot noise to get a signal to noise ratio of 10:1 from the far end of the cell.

A Dual Correlated Sampling (DCS) is used to determine if a pulse is a signal or not.

3.7.4   APD Sag and Ringing

Bench-top charge-injection tests of APDs have shown that when any particular channel on an APD is triggered, the other 31 channels exhibit a a drop in the output. Also the observed APD output itself is diminished by the same amount of voltage that the other APDs drop. This drop is linearly correlated to the amount of charge injected to the channel and is about 1.86% of the total charge injected. The consequence of APD sag is the APD ringing or flashing which is observed after a very a highly ionizing interaction takes place. APD flashes usually happen several microseconds after the initial charge deposition and are well-separated from the main event in time.

3.7.5   Timing Peak

The activity that is registered in the ND is mostly due to the interaction of neutrinos, as the ND is 100 m underground from Earth's surface, which prevents the cosmic interactions. The neutrino interactions occur within the 10 μs NuMI spill, which is easy to discriminate from electronics noise arise from various electronic components in the FEBs and DCMs. The NuMI beam peak is visible by just plotting the hit times within the
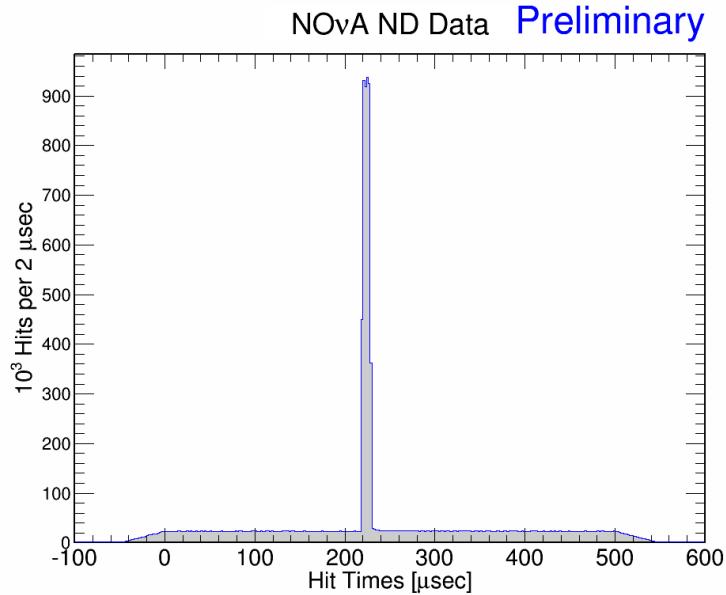
Figure 3.11: ND timing peak, over the full 500 μs window.

500 μs NuMI trigger window, with no cuts applied. The location of the beam spill in the 500 μs trigger window is found to be consistent with the expectation of 218–228 μs. The ND timing peak is shown in Figure 3.11 and the batch structure in NuMI spills is visible in Figure 3.12. The NuMI spill is composed of six batches of protons.

3.8 Experiment Simulation

The simulation used in the SBL ν_τ appearance analysis of the NOvA data is discussed briefly in this section. The full chain simulation is a long multi-step process which reduces the complexity and gives more opportunity for the validation in each step. The maximum information is
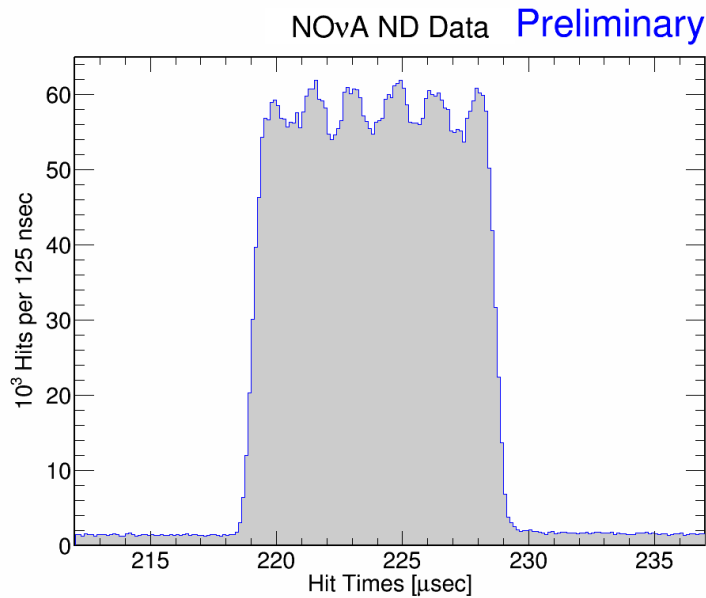
Figure 3.12: ND timing peak, over the full 500 μs window zoomed-in to show the NuMI beam structure.

stored for a minimal effort to reproduce future results and trace any errors that may occur at any stage. Simulation chain has mainly two stages, which are the beam simulation and detector response simulation.

3.8.1   Particle Simulation

Beam

The NOvA simulation chain starts with the simulation of hadron production and decay in the NuMI beam-line. This simulation is performed using FLUGG [54] package, an interface between FLUKA (for simulat-

ing particle interactions and decay) [55,56] and GEANT4 (for simulating the geometry, the environment with which the particle interact in and with) [94]. FLUKA simulates proton interactions and the hadron production in the NuMI target. GEANT4 is a tool kit for simulating the particle propagating through matter, which in NOvA for propagating the target interaction products through the NuMI beamline.

The decay of the spin 0 hadrons is isotropic in their rest frame and hence the probability for decay of neutrinos pass through the detector is just the fractional solid angle that the detector subtends at the point of hadron's decay, which makes the simulation a time consuming process and expensive on computing resources. The information about the neutrino parents like the particle type, energy, momentum and decay point are stored in the output files of the FLUGG simulation. The next step of the flux simulation is repackaging of the `flugg` format files to a unified format called `Dk2Nu`, which has the same format for any experiment using the NuMI beam. However to reduce the computation time, `Dk2Nu` files are further sampled over a 'window' that shadows the detector of interest, ND or FD of NOvA. The output from the flux simulations are in the `GSimpleNtpFlux` format or simply called as `gsimple` files.

Neutrinos

The interactions of the neutrinos in the NOvA detectors are performed with GENIE event generator which reads the FLUKA generated files.

The generator uses the interaction cross section and detector geometry information from the input files and determines if and where the neutrino interaction happens and also the kinematics of the interaction products. A hadronisation model is used in GENIE for determining the nature of Final State Particles (FSI) and their kinematics. The generator uses a sub-package called INTRANUKE to simulate the FSIs while they are still inside the nucleus [57]. FSI rates are determined from the the free hadron cross sections and the density of the nucleus. A huge uncertainty on this models arise due to the difficulties for the measurement of these interactions directly effect the observed energy of the neutrinos in the experiments.

Cosmic rays in NOvA are generated using the Cosmic RaY (CRY) [58] generator , which generates the primary cosmic ray particles between 1 GeV and 100 TeV and secondaries between 1 MeV to 100 MeV.

Particles in Detector

A Geometry Description Markup Language (GDML) by CERN is used to code the geometry of the NOvA detectors and detector surrounding including the rock around ND, which is parsed by ROOT's geometry class. GENIE and CRY simulates the particles from a neutrino interaction and cosmic showers and then that is passed to the GEANT4 simulation package for simulation of their propagation, energy loss and possible decays. the high beam intensity at ND causes many neutrinos to interact in the

rock in front of the detector. Simulating these interactions requires allowing GEANT4 to propagate muons through a very large rock volume which is a slow process, and only a few of these muons will make it into ND. To account this, simulation includes many neutrino interactions with a mother volume including a large rock volume in front of the detector and keep only those that leave energy in the detector. In the normal simulation this 'rock interactions' are overlaid at a rate determined at the time of the generation of flux files after the GEANT4 stage. The physics processes are modeled using a Physics list. NOvA simulation uses the `QGSP_BERT_HP` list, which consists of quark gluon string (QGS) model for modeling high energy hadrons with Bertini cascade model for hadronic processes with less than 10 GeV energy. Also, it has a high precision neutron model that tracks thermal neutrons (< 20 MeV) accurately. The output from the GEANT4 at this stage contains the list of particles involved in the detector interaction and the full suit of information which mainly includes the energy deposited and the positions.

3.8.2   Detector Response Simulation

Photon Transport

The NOvA detectors are composed of many identical readout cells, however the collection of scintillation photons by the fiber, the transport of light up the fiber, and the response of the APD to captured light are taken into account and photon transport is performed by the *Improved-*

Transport modules in the *PhotonTransport*. The detector is treated as uniform in this process and any individual differences between cells is removed by the downstream calibration at a later stage. The individual photons are not traced from emission to the APD due to the limitation in the computation time. A ray tracing algorithm was developed to understand the collection of scintillation photons by the fiber, which assumes a scintillator emission time of 9 ns, a uniform wall reflectivity of 87.7%, an oil index of refraction of 1.46, and an exponential photon capture probability with a capture length of 30.66 cm which was determined by matching the behavior of the attenuation curves for cosmic ray muons near the ends of cells in data and MC. The collection rate template as a function of collection time relative to the time of the energy deposit (ΔT) and the collection location along the fiber relative to the position where the energy was deposited (ΔZ) is shown in Figure 3.13. The reflectivity of the cell walls as a function of wave length is shown in Figure 3.14. The photons transported up the fiber is used to determine the number of photons absorbed by the APDs as a function of time. For a given bin in the ΔZ, half of the collected photons are transported through the long path around the fiber loop while the other half are transported through the short path. The mean number of the photons survive after transport are determined by an attenuation curve.
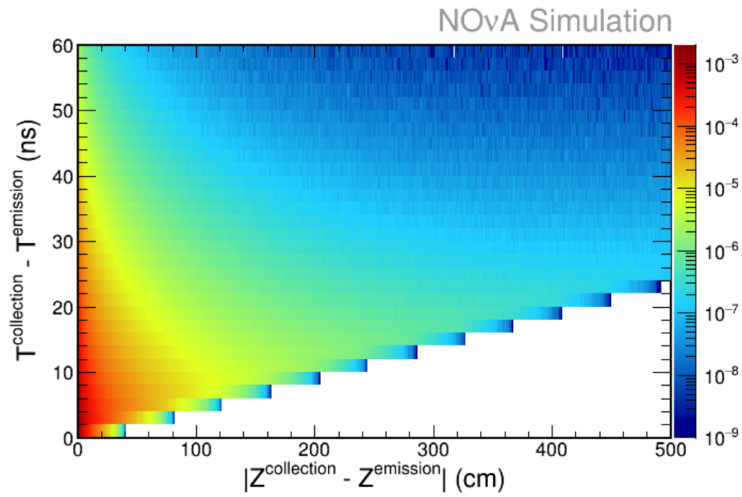
Figure 3.13: Distributions used in the photon transport simulation. Collection rate as a function of time and distance traveled from scintillator emission.
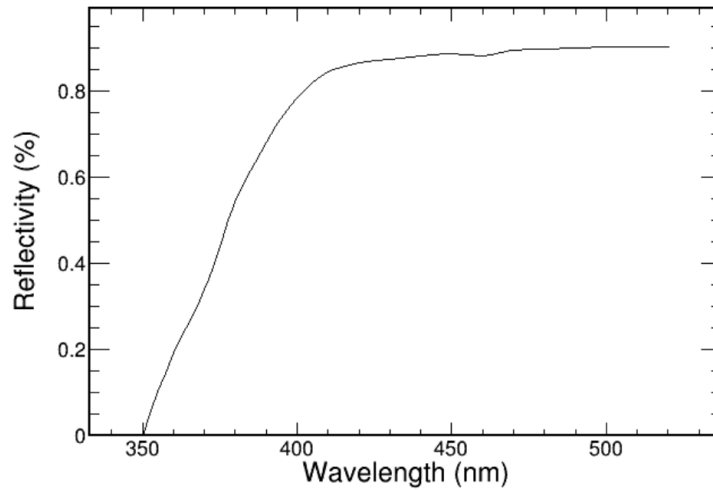
Figure 3.14: Distributions used in the photon transport simulation. Cell wall reflexivity as a function of wavelength.

Electronic Readout Simulation

The last part of the simulation models the electronics readout simulation. The APD is modeled to have an average efficiency of 85% quantum efficiency and a gain of 100 with 5% variation. The distribution of the excess noise expanded photo-electrons are converted as a function of time from the photon transport stage into digital signals similar to those collected from the detector. FEBs emulates contain three chips, an ASIC which performs the pulse shaping, an ADC which converts the shaped analog signal to the digital signals and a FPGA which performs the real-time zero suppression. The pulse shaping in the ASIC is performed by a CR-RC circuit in data as:

$$f(t) = N_{pe} \frac{F}{F - R} \left(e^{-(t-t_0)/F} - e^{-(t-t_0)/R} \right) , \qquad (3.5)$$

where R and F are the rise and fall times, N_{pe} is the number of the photo-electrons collected and t_0 is the time at which the pulse occurred. To simulate the current and voltage variations, the shaped pulse is distorted and converted in ADC based on a predetermined *PE* to ADC conversion factor which is determined from the charge-injection studies.

Tuning to data

The cosmic trigger data and simulation are used to tune the simulation to the raw detector response. The pulse height per each cell per path length

as a function of distance from the APD in the simulation are compared to the distribution from the data to tune the absolute scintillator light level. The tuning results are shown in Figure 3.19. The ND data is used for various effects and found two major effects are missing in the simulation, as discussed below.

APD Sag Simulation

The APD pixels share a common voltage source driving the avalanche multiplication, which causes the baseline of all other pixels to sag when a large deposit occurs in one pixel. The comparisons of path length normalized pulse heights in muons in ND data showed a clear and non-negligible effect due to this sag. For the muons which leave multiple hits in a plane, the $d(PE)/dx$ in the plane for the muons drops around 1.87% of the total charge deposited on the APD. Including this effect in the simulation makes a better agreement with the data.

Scintillator Quenching

When the ionization density due to the particle passage in the liquid scintillator increases beyond a limit, the light output is no longer proportional to the dE/dx of the particle due to the quenching of the primary fluorescence process.

Diblock and Bad Channel Masking

The DAQ system for di-blocks are independent and can switch on or off independently. The data from different period varies since detector was not fully commissioned at the beginning of the data taking. This results in different diblock configurations in the first few months of NOvA data. The information that which diblocks were active during a run is stored in the database and is associated with a run number. Also in any subrun some of the channels are masked due to the high noise levels or lower than the acceptable data rate. The channel mask information is also stored in the database in subrun basis. To make the the simulation close to the real detector data, use this masking information in the simulation. For the better statistics in the simulation, these information are used repeatedly in the simulated files by weighting by POT collected in that data time.

3.9   Event Reconstruction

An above threshold charge deposits in a detector cell or noise are stored as a vector of hits in the raw data. However this information is not enough to proceed with an analysis, hence the data should be reconstructed for the further physics investigations. The first and foremost step is to apply correct calibration weights to the data files so that the hits can be translated to a set of energy depositions consistent everywhere in the
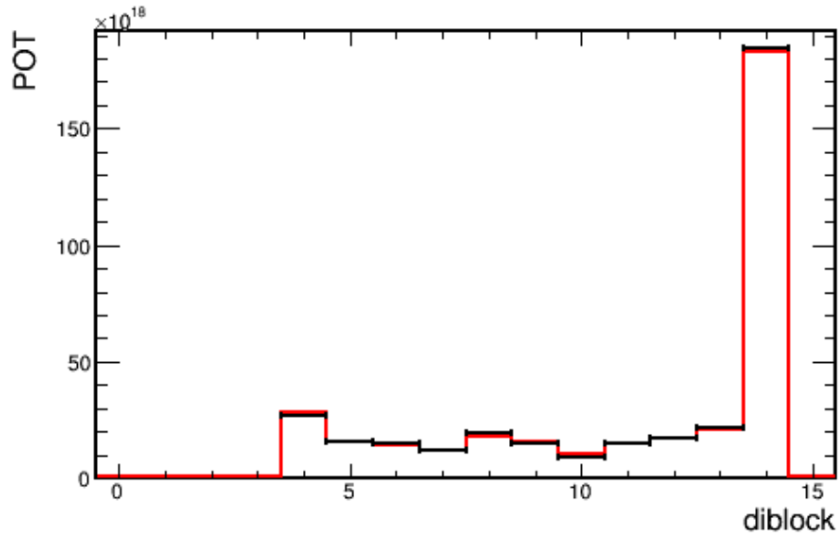
Figure 3.15: The relative exposure in each diblock configuration in data and simulation. The red line represents the simulation and the black line data. The simulation is area normalized to data.

detector. The algorithms for new objects and features are developed to make this data useful for different physics goals.

3.9.1   Calibration

The cosmic ray data is used for the calibration of NOvA detectors to ensure the uniform detector response. A tracking algorithm is used which reconstructs the cosmic rays in the detector and a set of quality cuts applied to the muons to make sure that the reconstructed tracks are muons. The energy deposited in a cell is normalized by the path length in a cell and the channel response is then calibrated. The path length
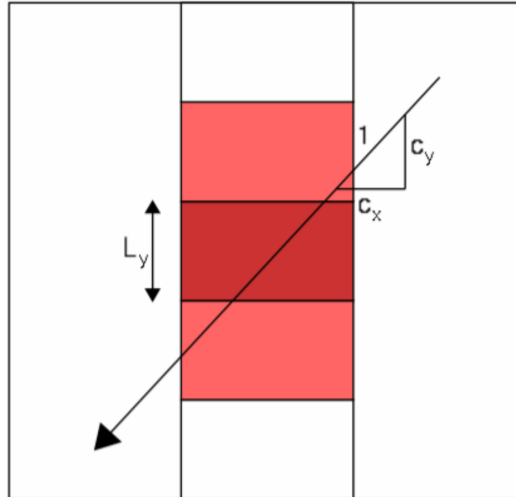
Figure 3.16: Selection of tricells associated with a track. The dark red cell is a tricell because its neighbors are triggered by the same cosmic ray. The path length in cell is given by Ly/Cy.

on a cell by cell basis is difficult to reconstruct and hence a set of three adjacent cells (tricells) are used, which are triggered by the same cosmic ray as shown in Figure 3.16. This also corrected by the direction cosine in that view to make sure that the particle entered through the top wall and exited through the bottom wall, The process of calibration has two major steps, the relative and absolute calibration. While relative calibration accounts the threshold effects and the attenuation across a single cell, the absolute calibration creates a scales factor for each detector to convert the calibrated *PE* scale from the relative calibration into an energy unit.

Relative Calibration

Relative calibration accounts the threshold effects and the attenuation in the wavelength shifting fibers and corrects PE value, the PE_{Corr}. The 3D tracks are produced using a window tracking algorithm, which fits the straight lines through the hits. Only tricell hits are used for this calibration. The distance from the readout is labeled as W and if $W{=}0$, that means the center of the cell and positive values are closure to the readout. Individual histograms of PE/cm vs. W are constructed for each cell and finally the relative calibration applies the corrections to these histograms. The correction factor applied is:

$$T = \frac{PE}{\lambda} \times \frac{E_{\text{True}}}{E_{\text{MIP}}}. \qquad (3.6)$$

Where PE is the number of simulated photons that the electronics register, T is the correction factor, λ is the number of photons that is seen without fluctuations, E_{True} is the true energy deposited in the scintillator, and E_{MIP} is the energy that would be deposited based only on the path length through the cell. PE/λ accounts for the threshold correction as λ depends only on path length. The histograms used in Figure 3.17 are the examples which used to correct the corresponding data and MC. In the second step of the relative calibration, a general form of the attenuation correction is applied. Tricell hits are grouped by cell and fitted to a double exponential considering the long and short path. The
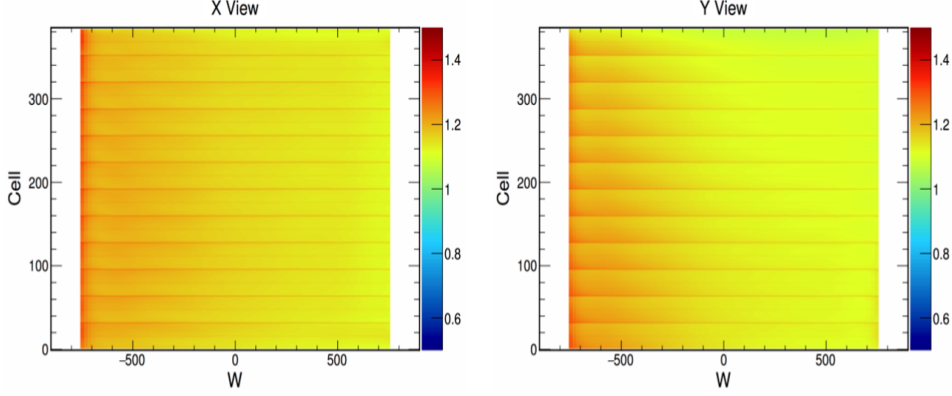
Figure 3.17: Correction factor for the threshold and shielding effects at the FD as a function of number of cells and distance W from the readout. Cells in the X view is in the left and Y view is in the right.

exponentials are given in the following eq:

$$y = C + A \left(\exp\left(\frac{W}{X}\right) + \exp\left(-\frac{L+W}{X}\right) \right). \qquad (3.7)$$

Where L is the full length of the detector. The parameters, X, the attenuation length C and A are the free parameters. The fit excludes the hits in the close and furthest distance to the readout. The final step is to apply the attenuation correction at the ends of the cells and the residuals from the above in the central part of the cells. A polynomial function is added to the above exponential form at the two ends of the cells given by,

$$y = \begin{cases} 1 - \alpha_R(W - W_R)^4 & : W > W_R \\ 1 - \alpha_L(W - W_L)^4 & : W < -W_L \\ 1 & : \text{otherwise}. \end{cases} \qquad (3.8)$$

A LOWESS (Locally WEighted Scatter plot Smoothing) fit is done on the residuals from the exponential fit to smooth the cell response to fix the issue of fiber performance variation.

Absolute Energy Scale

Absolute energy calibration converts the attenuation corrected response into energy units. The cosmic muons enter from outside the detector at which of them are stopped inside the detector are used for this purpose. According to Bethe-Bloch curve, the stopping muons deposits the energy in a better estimate. We use a 1 m long window on the track, which is 1 m away from the stopping point to measure the detector response as dE/dx is approximately flat in this region. PE_{Corr}/cm distribution is used to find the scale factor between data and MC. This scale factor is used to convert PE_{Corr}/cm in data to MeV/cm. dE/dx as a function of the distance from the stopping point of the incoming muon is shown in the Figure 3.18. Attenuation corrected dE/dx is shown in Figure 3.19. the difference in the response between MC and data is used as a scale factor to determine the PE_{Corr} to MeV conversion factor for the data.

Timing Resolution

For determining the timing resolution in ND the muon candidates from the neutrino interactions happen in the surrounding rock at ND is used
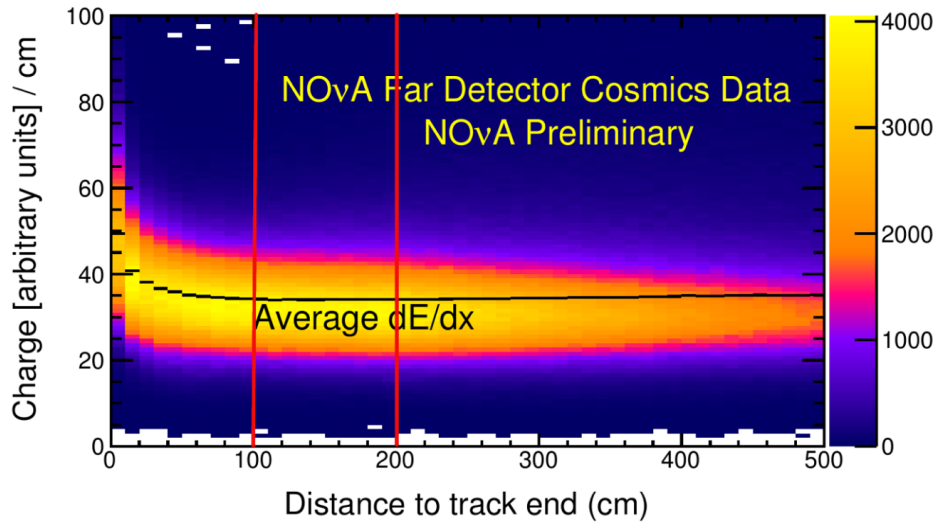
Figure 3.18: dE/dx as a function of distance from the stopping point of muon. the hits between two red lines of 1 m window is used for the absolute calibration.
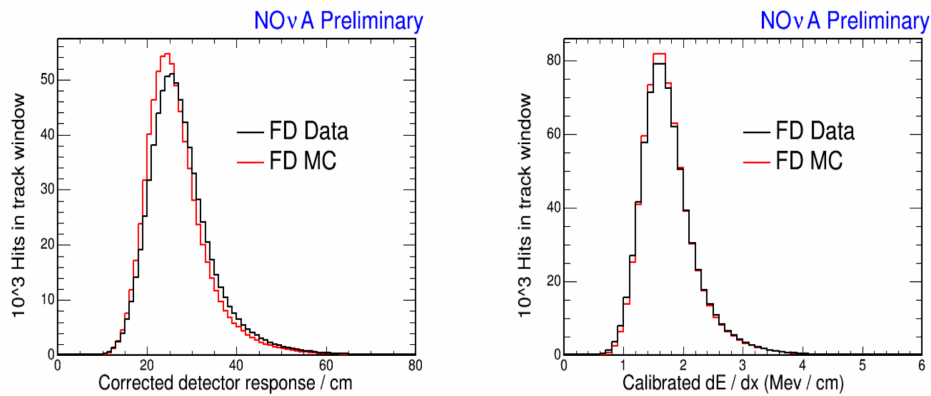
Figure 3.19: Left: The attenuation corrected dE/dx is different for data and MC. Right: Calibrated dE/dx in MeV using this conversion factor.
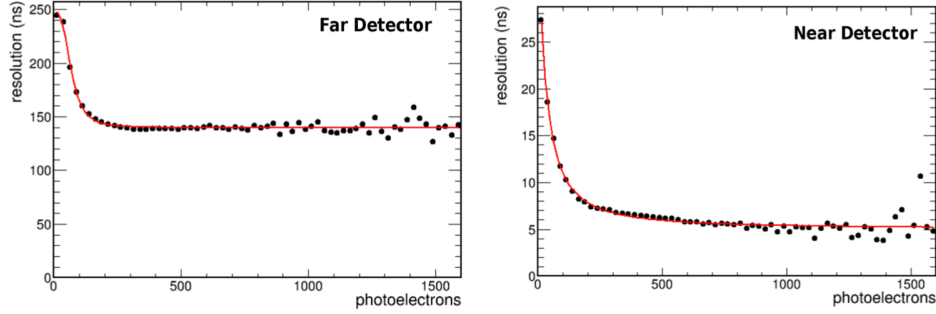
Figure 3.20: Left: Timing resolution as a function of *PE* for the far detector. Right: Timing resolution as a function of *PE* for ND.

and in far detector, the through-going cosmic muons are used. The hits are corrected for the time of flight of the muon and the time of flight of the light in the WSF to the APD. The time resolution is calculated as follows:

$$\sigma_t = \frac{p_0}{p_1 + n_{p_e}^{p_2} + p_3},\tag{3.9}$$

where σ_t is the timing resolution, $n_{p_e}^{p_2}$ is the number of photo-electrons. The timing resolution as a function of *PE* for FD and ND are shown in Figure 3.20.

3.9.2 Reconstruction Chain

The neutrino interactions in the detectors have different topologies based on the interaction type and the nature of the final state particles. The ν_μ CC interactions leaves a long muon track in the detector while ν_e CC interaction produces an electromagnetic shower. The NC interactions

leave the hadronic shower in the detector. And if a ν_τ CC interaction happens in the detector, the additional particles coming from the tau decay are also visible in the detector in addition to the hadrons coming out of the nuclear scattering. The process of reconstruction of ν_μ CC is mainly using a tracking algorithm to find the long muon tracks, while the ν_e CC are reconstructed using a clustering algorithm, which helps to reconstruct the electromagnetic shower. It is important to understand all the algorithms and methods used for the reconstruction of all types of interactions in the detector since $\nu\mu, \nu_e$ CC interactions and NC are the major background in the ν_τ appearance analysis. Even though the τ particle coming out of a ν_τ CC interaction are not visible in the detector due to it's short lifetime and decay length, however it is possible to identify the τ decay products in the detector. The different event topologies in the NOvA ND are shown in Figure 3.21. The raw data contains the information about the cell hits with the cell, plane, energy and time at which that hit happened. A slicing algorithm is used to cluster this hits into a single slice if they belongs to a single interaction. A slice is an independent, but self-contained interaction and hence all further reconstruction are done on the hits which are in the same slice.

3.9.3   Slicing Algorithm

A Density-Based Spacial Clustering of Application with Noise (DBSCAN) algorithm is used for slicing in NOvA, which groups the points that are close enough in the parameter space and marks the points that lie in the
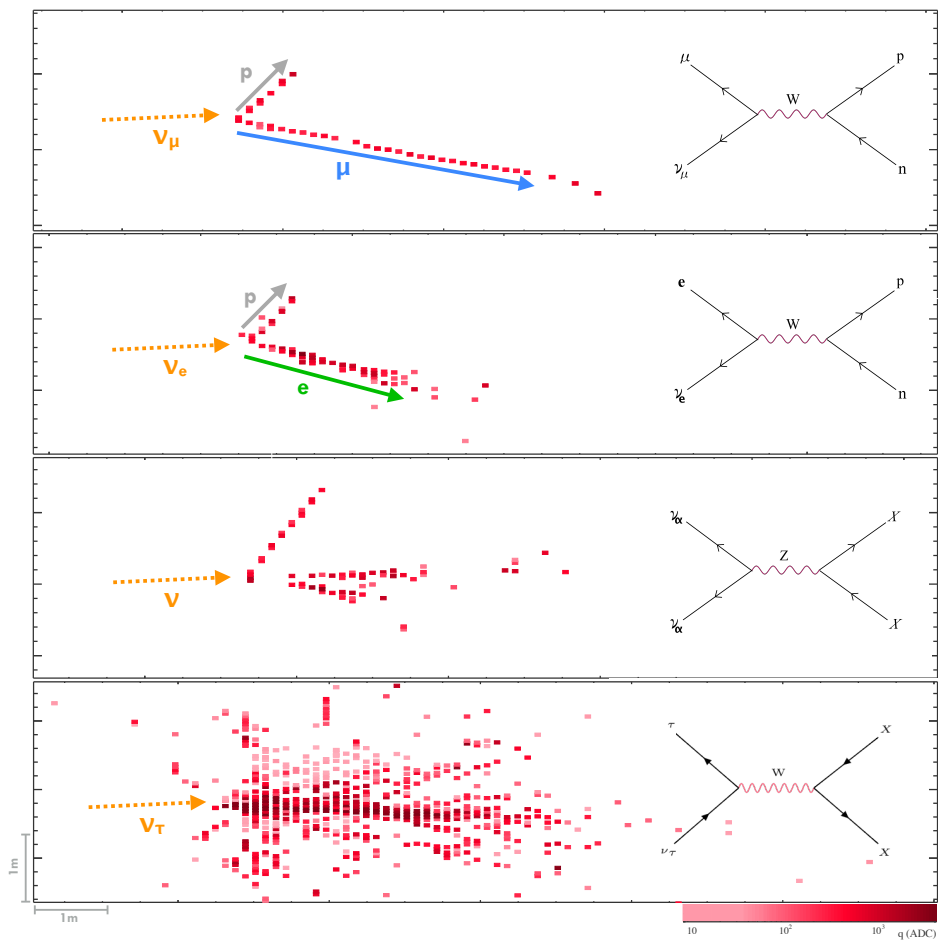
Figure 3.21: Different event topologies in the NOvA ND.

low density points as noise [52]. A core-point is determined using the condition that the point contains more than a certain number of close points, $MinPts$, within its distance ϵ from itself. The neighborhood points are considered as directly-reachable from the core-point and the points on the edge of the clusters are as border points even though they do not have a minimum number of hits in their ϵ neighborhood but they are neighbors of the core-points. A border point is considered as directly reachable from a core-point if the points connect these two are itself core-points. The points that are not falling in this category are considered as loners, treated as noise.

The clustering algorithm scans all the points and find a core-point and all its neighbors and the border-points then the algorithm returns to find the next core point. The algorithm has two free parameters, ϵ and $MinPts$, which are tuned based on the density of the clusters and noise. A distance function is defined for the two hits in the same view:

$$D = \left(\frac{\Delta T - \Delta \vec{r}/c}{T_{\text{res}}}\right)^2 + \left(\frac{\Delta Z}{D_{\text{pen}}}\right)^2 + \left(\frac{\Delta(X \text{ or } Y)}{D_{\text{pen}}}\right)^2 + \left(\frac{PE_{\text{pen}}}{PE}\right)^5. \tag{3.10}$$

Where T_{res} is the timing resolution of the hits added in quadrature, PE is the number of photo-electrons in both hits added in quadrature, D_{pen} is the distance penalty, PE_{pen} penalty term for the number of photo-electrons. $\Delta \vec{r}$ is the 2D distance between the two hits, ΔZ and ΔX or Y are the 1D distances between the hits in Z and X/Y directions. The last term prevents the addition of noise hits into the clusters since the noise hits are of low density. Term has a power of 5 since the noise spectrum
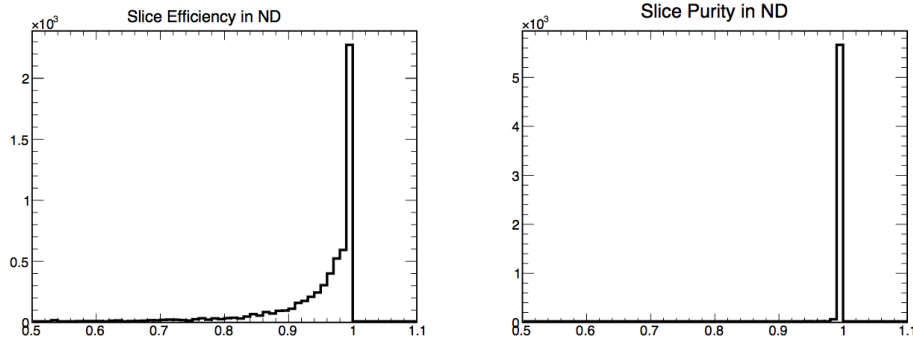
Figure 3.22: Left: Efficiency of the slices in ND simulation. Right: Slice purity in ND simulation. $\sim 80\%$ of slices have $> 90\%$ efficiency and $\sim 95\%$ have $> 90\%$ purity.

drops off as $PE^{-2.5}$. The free parameters are tuned independently for FD and ND as they have different event rates. The efficiency and purity terms are defined, where efficiency is the measure of the fraction of hits from an interaction that are contained in the slice and purity is the fraction of hits in a slice that come from the leading interaction in the slice, which are considered as the measure of the slicer performance. The example of efficiency and purity plots in ND are shown in Figure 3.22.

3.9.4 Hough Transform Line Finding

The ν_e reconstruction chain starts with identifying the line like features in a slice. A modified Hough Transform is used to achieve this as described in Ref. [59]. A brief summary is given below. The lines are

parameterized in a polar space(ρ, θ) to deal with the vertical lines. The *XZ* and *YZ* views in the detectors are parameterized separately using a Gaussian smear vote for the lines passing through each pair of points. The expression for the vote is given below.

$$w = e^{-\frac{(\rho - \rho_0)^2}{2\sigma\rho^2}} e^{-\frac{(\theta - \theta_0)^2}{2\sigma_\theta}}. \tag{3.11}$$

Where $\sigma_\rho = \frac{3}{\sqrt{12}}$, $\sigma_\theta = \frac{3}{d\sqrt{6}}$ and d is the distance between the two points. 3 cm is the width of the cell and σ_ρ is the uncertainty due to the top-hat distribution. The peak due to the true lines in the Hough polar space are grouped together to form a peak in the Hough space and are represented by a weighted mean around the peak. The peaks in the Hough-space below certain threshold are not reconstructed into a line. An iterative process is used to find the line and the Hough map is formed after each iteration removing the most prominent Hough-line, which ensures the remaining lines in a slice are not affected by the prominent ones.

3.9.5   Elastic Arms Vertex Reconstruction

The elastic arms vertex reconstruction algorithm uses the Hough lines as the seeds for finding the original vertex of the neutrino interaction. The algorithm is otherwise known as the method of deformable templates since the arms that reconstructs the particles may be deformed or adjusted to better represent an event. The following energy function is used

to find the seed vertex and the arm direction [50].

$$E = \sum_{i}^{N} \sum_{a}^{n} V_{ia} d_{ia} + \lambda \sum_{i}^{N} \left(\sum_{a}^{n} V_{ia} - 1 \right)^2 + \frac{2}{\lambda_v} \sum_{a}^{n} D_a. \qquad (3.12)$$

Where n and N the total number of arms and the hits in the slice, d_{ia} is the distance of the ith hit from the ath arm, which is normalized by the detector spatial resolution. The third term assigns a penalty to arms those start more than a distance λ_ν away from the event vertex, where $\lambda_\nu = 7/9X_0$, which is the photon radiation length and V_{ia} is a measure of the strength of association of the ith hit to the ath arm which is given by:

$$V_{ia} = \frac{e^{-\beta d_{ia}}}{e^{-\beta\lambda} + \sum_{b=1}^{n} e^{-\beta d_{ib}}}. \qquad (3.13)$$

The parameter β can be interpreted as inverse of temperature. The final minimization step is the minimization of all scanned vertex seeds and arm directions set that minimize the equation using root's MINUIT class. Fitting starts at low values of β to avoid local minima in the energy function, and slowly increased to close-in on the final event vertex.

3.9.6 Fuzzy K-Means Clustering

Fuzzy-K algorithm follows elastic arm reconstruction to cluster the hits from different particles into different prongs. Fuzzy-K uses *XZ* and *YZ* views separately to construct 2D prongs using the vertex from the elastic arms as the origin. Fuzzy-K treats prongs from different particles as

the energy peaks as an angular distributions in that view, which further reduces to a 1D distribution [51].

The method is based on a Fuzzy-K means clustering algorithm that extended to a situation where the number of clusters are unknown to begin with. This method allows a hit to belong to more than one cluster and the boundaries of the clusters are fuzzy. Every hit including noise is allowed to be associated with at-least one prong, however an extension of this algorithm allows its application to remove the association normalization constraint and allows the noise hits to remain dissociated to a prong. The algorithm first calculates the association of hits to the prongs by seeding the prongs and updating the prong centers. The prongs are seeded in an angular space based on a density matrix w:

$$\omega_k = \sum_i^n e^{\left(\frac{\theta_i - \theta_k}{\sigma}\right)^2},\tag{3.14}$$

with

$$\theta_k = -\pi + \frac{k * \pi}{180},\tag{3.15}$$

where k is varied from 0 to 360 with increment of 1 each time. The angular separation between the ith cluster core, which is defined as the line passing through the vertex at the seed angle and the jth hit are calculated using:

$$d_{ij} = \left(\frac{\theta_j - \theta_i}{\sigma_j}\right)^2.\tag{3.16}$$

The numerator is limited in between -π and π. The cluster membership

is assigned using:

$$\mu_{ij} = e^{-\frac{md_{ij}\sqrt{a}}{\beta}}.$$ (3.17)

Where a is the number of clusters in the slice, m is the measure of the fuzzyness of the clusters and set to be 2, β the expected spread of the hits around the cluster is set to be 4. The cluster centers are then updated using:

$$\theta'_i = \theta_i + \frac{\sum\limits_{j}^{n} \frac{\mu_{ij}}{\sigma_j^2} (\theta_j - \theta_i)}{\sum\limits_{j}^{n} \frac{\mu_{ij}}{\sigma^2_j}}.$$ (3.18)

The iteration process is continued until the separation between the new cluster centers and the previous ones is less than a predefined tolerance limit. The 2D clusters in both XZ and YZ views are matched to form 3D prongs. A 2D cluster is matched with 2D cluster in the other view to find the best matching clusters. If the 2D cluster is matched correctly with a cluster in the other view, the energy profile should be very similar in the two views. To do this, cumulative energy response as a function of distance is plotted and a Kuiper metric, $K = min(D+, D-)$ is used to find the best match for a prong. Where $D+$ and $D-$ are the magnitude of the lowest negative or largest positive distances between the profiles. Thus the prongs with the lowest scores are matched and all other pairs are removed, iteration continues until there are no remaining possible matches.
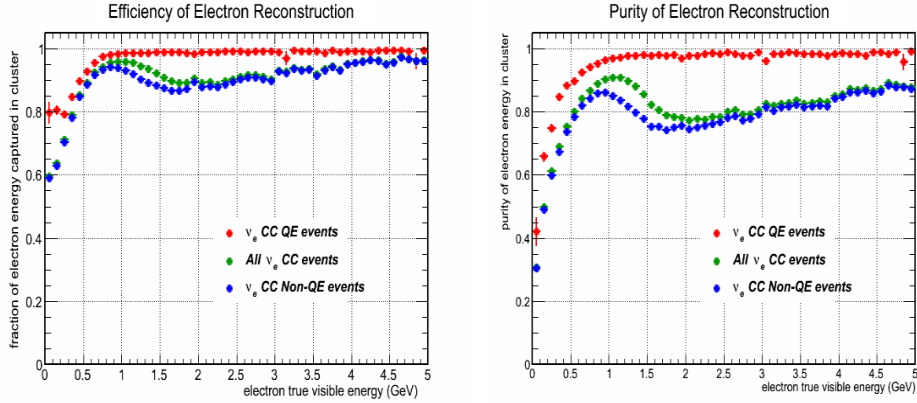
Figure 3.23: Left: Efficiency of the the reconstructed Fuzzy-K prongs. Right: The purity of the reconstructed Fuzzy-K prongs. Purity and efficiency $> 80\%$ corresponds to the true electrons. Low efficiency and purity shows a significant hadron showers due to the rise in the non-QE modes of neutrino interactions.

3.9.7   Kalman Tracking

A Kalman filter is used to start with the reconstruction of the ν_μs. The algorithm identifies the track like features from the hits in the slice. Reference [60] details of the algorithm used to describe the reconstruction of the Kalman tracks.

3.10 Particle Identification Algorithms

3.10.1 Convolutional Neural Networks (CNN)

Recently, the field of computer vision has improved the machine learning algorithms to extract the feature maps by implementing the deep learning CNN. The multi-layered networks used by the deep learning can mitigate the drawbacks of the traditional networks. The CNN considers the spatial structure of the input images. It consists of several convolutional layers that extract features from the input image deeply as each input image is transformed into different convolutional layers and each layer extract different features of the image.

The input data is transformed to a convolutional layer as follows,

$$(k * g)_{p,q} = \sum_{l=-\infty}^{\infty} \sum_{m=-\infty}^{\infty} \sum_{n=0}^{c} k_{l,m,n} g_{p-l,q-m,n}. \tag{3.19}$$

Where k is the kernel or the filter consists of the filter weights, g is the pixel intensity sequence. (p, q) is the position of the hidden neuron in the hidden layer. Each hidden layer extracts one feature of the image, which is called a feature map between the input layer and the hidden layer. CNNs apply a technique called pooling that reduces the dimension of the input layer by employing a 'max pooling technique'. In max pooling, every n×m sub-region in the previous convolutional layer is replaced with a hidden neuron corresponding to a maximum weight. To avoid the

information loss, the pooled regions are chosen to overlap [63].

The NOvA experiment uses the CNN to classify neutrino interactions. The CNN used in NOvA is called Convolutional Visual Network (CVN) in which we use a deep network architecture developed by Google called GoogLeNet [61]. The NOvA CVN is implemented using the caffe framework which provides a relatively fast training on graphics processing units [62]. The CVN network layers used in NOvA is shown in Figure 3.24. The two separate views in NOvA detectors for the neutrino interactions, X-view and Y-view is trained separately using the three inception modules. Then concatenated the two views to obtain the final output which is then fed to the final inception module which extract the combined features of these views. The average pooling is done on the final output for further downsampling. The final score is obtained from the softmax function which classifies the event. CVN classifies the neutrino interactions both into CC or NC and by the neutrino interaction modes; QE, RES and DIS.
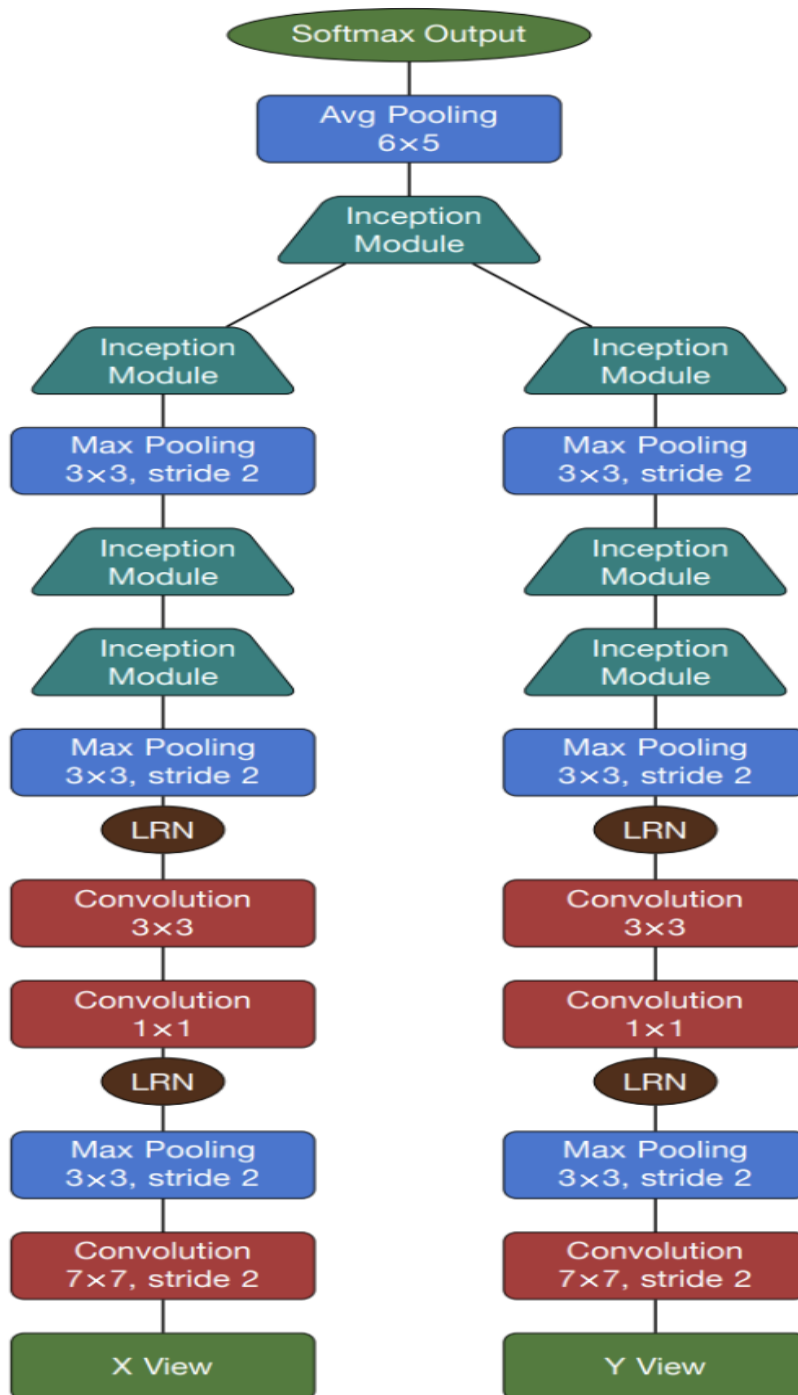
Figure 3.24: The block diagram of CVN architecture used in NOvA.

Chapter 4

Particle Identifiers for Hadronic ν_τ CC Events

This chapter summarizes the particle identification method employed for hadronic mode CC τ neutrino interactions in NOvA ND. We used 15 variables as inputs to different training methods listed in root-TMVA [64] package for the PID training and found BDT (Boosted Decision Trees - Gradient) gives the best results when the selection cuts are optimized for a figure of merit defined as the ratio of the signal events to the background events (FoM = S/B). We trained BDT separately for NC and ν_e, ν_μ CC backgrounds assuming the signal ν_τ CC events are dominated by hadronic mode τ decays. This method gives a better figure of merit (S/B) than training over all background together and returning a single PID.

The challenging problem in SBL ν_τ appearance analysis is the selection of high energy ν_τ CC interactions with maximal signal purity. The ν_τ CC interactions produce a τ lepton that typically decays to one or

three charged particles. The τ is the only lepton that can decay into hadrons - the other leptons do not have the necessary mass (τ mass = 1776.82 ± 0.16 MeV/c^2) to decay into hadrons. The primary background to the τ sample are ν_e or ν_μ CC interactions together with a failure in the lepton identification constituents. The NC events also are the major background to the ν_τ CC interactions.

The CVN classifier (production-3 version) [66] we use in this analysis was trained for the FD ν_τ CC interactions without classifying them on the basis of τ decay modes since they were trained for the standard oscillation analyses in the FD. This BDT training is done specifically for ν_τ CC interactions with hadronic decay of τ leptons (ν_τ^{had} CC) as this analysis looks only for hadronic mode of ν_τ CC interactions.

4.1   Data Sets

Following are the MC NuMI data sets used for the training and testing samples. We divided the total MC dataset to two equal halves for training and testing BDT.

- **MC data used for ν_τ CC hadronic signal:**
  `prod_caf_R17-03-01-prod3reco.k_nd_genie_nonswap_fhc`
  `_nova_v08_full_cycle0_v1_nutaucc-overlay`

- **MC data used for ν_μ CC, ν_e CC and NC backgrounds:**
  `prod_caf_R17-03-01-prod3reco.d_nd_genie_nonswap`

`_fhc_nova_v08_full_v1`

- **ND NuMI data used for sideband study:**

  `prod_caf_R17-03-01-prod3reco.d_nd_numi_fhc_full_v1_goodruns`

The total data set used for this study corresponds to 8.06×10^{20} POT and the MC files used is 3.54×10^{21}, which is scaled to the data POT for data MC comparison. We applied `kPPFXFluxCVWgt * kXSecCVWgt2017` weights for MC files.

4.2   Preselection Cuts

A set of preselection cuts are used before preparing the input samples which remove a huge number background events. Also the fiducial volume and containment cuts are used to remove the background arising due to the interactions happening outside the detector volume. The maximum possible background rejection are achieved using cuts based on a figure of merit defined as, FoM = Signal/Background, on CVN ν_μ and NC classifiers which rejects ν_μ CC and NC respectively without loosing ν_τ^{had} CC signal events. The event quality cuts (a minimum of one reconstructed vertex, one reconstructed track and one reconstructed shower) are also applied before preparing the input samples. A cut on calorimetric energy (kCaloE > 4.2 GeV) is applied to remove the majority of low energy background interactions. Details of the preselection cuts are shown in Table 4.1. These are the same preselection applied in this

Cut	Details
kNDFiducial	Fiducial volume cut
kNDContain	Containment cut
CVNm < 0.1	CVN numu classifier
kCVNnc < 0.6	CVN nc classifier
kCaloE > 4.2	Calorimetric Energy (GeV)
kNVtx > 0	Number of vertices
kNTrks > 0	Number of tracks
kNShw > 0	Number of showers

Table 4.1: Preselection cuts used in BDT while training. Those cuts should be applied while using these BDT outputs for the best performance.

analysis [69].

4.3　BDTG Training

We trained three BDTs separately for ν_e CC, NC and ν_μ CC backgrounds assuming the signal ν_τ CC events are dominated by hadronic mode τ decays. The details of training and testing these three BDTs are given below.

We used a BDT that uses gradient boosting for the training of particle discriminants. More details of BTD training are given in Ref. [65]. The gradient boosting is applying the method of gradient descent to the idea of boosting, which says that a set of weak learners (those which label slightly better than random guessing) when combined in a methodical manner, usually weighted, can create a stronger learner. Seminal work

on this subject was done by J. H. Friedman [67] in 2001.

4.3.1 $\nu_e - \nu_\tau{}^{\mathbf{had}}$ Discriminant

For $\nu_e - \nu_\tau{}^{\mathrm{had}}$ discriminant, we trained BDT assuming ν_e CC interactions are the only background events and signal events are defined as the hadronic ν_τ CC interactions. We trained over 100k signal and same number of background events and tested over the remaining 100k signal and background events.

Input variables

We tried around 50 different variables as input variables to BDT and found a set of 15 variables gave the best figure of merit (S/B) when tested on ν_e CC background vs. hadronic ν_τ CC signal events. These all input variables are well defined in CAFAna package (`CAFAna/Vars`). A brief description of these variables are given Table 4.2. Figures 4.1 and 4.2 show the signal vs. background input variables used for training $\nu_e - \nu_\tau{}^{\mathrm{had}}$ discriminant. The blue histograms show the signal events and red histograms show the background events.

Rank	Variable	Details
1	kNHit	Number of hits in slice
2	kShwNHit	Number of hits on primary shower
3	kCVNm	CVN ν_μ classifier
4	kTrkNHits	Number of hits on a track
5	kShwStartX	Shower X Start
6	kCVNe	CVN ν_e classifier
7	kCVNnc	CVN NC classifier
8	kReMIdMeasFrac	RemId input variable, plane fraction
9	kShwStartY	Shower Y Start
10	kShwStopY	Shower Y Stop
11	kShwStopX	Shower X Stop
12	kPtp	Transverse momentum fraction in slice
13	kCVNt	CVN ν_τ classifier
14	kShwEFrac	Fraction of slice energy in shower
15	kInelasticity	(slc.calE-shwlid.calE)/slc.calE

Table 4.2: The ranking of the input variables used in BDT while training $\nu_e - \nu_\tau{}^{\text{had}}$ discriminator. The variable rank, variable name and the details are given. The variable names used here are exactly the same as used in CAFAna.

Figure 4.1: The input variables used while training BDT for $\nu_e - \nu_\tau{}^{\text{had}}$ discriminant. Continued in the Figure 4.2.

Figure 4.2: The input variables used while training BDT for $\nu_e - \nu_\tau^{\mathrm{had}}$ discriminant.

Figure 4.3: The BDT input variables linear correlation matrix for (a) signal and (b) background of $\nu_e - \nu_\tau{}^{\mathrm{had}}$ discriminant.

Input variables linear correlation

The performance for regression is based on the correlation strength between input variables and the regression target and between the MVA method response and the target. Several correlation metrics are implemented in the framework to characterize any dependencies. More details are in Ref. [65]. Figure 4.1 and 4.2 show the signal (red) vs. background (blue) separation performance for each BDT input variable post-training. Figure 4.3 is the resultant linear correlation matrices for the input variables when considering (a) signal and (b) background.

Training Results

The final BDT response is shown in Figure 4.4a. The BDT weight files are then used to produce a ν_τ^{had} PID data product and consequently fill CAF

(a)   (b)

Figure 4.4: (a) The BDT training and testing output for $\nu_e - \nu_\tau^{\text{had}}$ discriminator and (b) the BDT outputs when add to the CAF files. Preselection cuts mentioned in Table 4.1 are used. The two-flavor oscillation parameters used are $\Delta m^2 = 22$ eV^2 and $\theta_{\mu\tau} = 0.175$ rad.

files with this product in order to produce Figure 4.4b, which breaks down the signal and background via the various neutrino interaction types: ν_μ CC, NC, ν_e CC, ν_τ CC and ν_τ^{had} CC.

We consider a two-flavor oscillation model to produce Figure 4.4b because we can approximate a 3+1 sterile oscillation model to a two-flavor model in the SBL approximation. We set the two-flavor parameters to a best sensitive parameter $\Delta m^2 = 22$ eV^2 and a mixing angle, $\theta = 0.175$ rad.

4.3.2   NC $- \nu_\tau^{\text{had}}$ Discriminant

For NC $- \nu_\tau^{\text{had}}$ discriminant, we train BDT assuming NC interactions are the only background events and signal events are the hadronic ν_τ CC

interactions.

Input variables

We considered only NC background as the total background while training NC $-\nu_\tau^{\text{had}}$ discriminant. We tried around 50 different variables as input variables to BDT and found a set of 15 variables gave the best figure of merit (S/B) when tested on NC background versus hadronic ν_τ CC signal events. These all input variables are well defined in CAFAna package (`CAFAna/Vars`). A brief description of these variables are given Table 4.3. Figures 4.5 and 4.6 show the signal vs. background input variables used for the training NC $-\nu_\tau^{\text{had}}$ discriminant. The blue histograms show the signal events and red histograms show the background events.
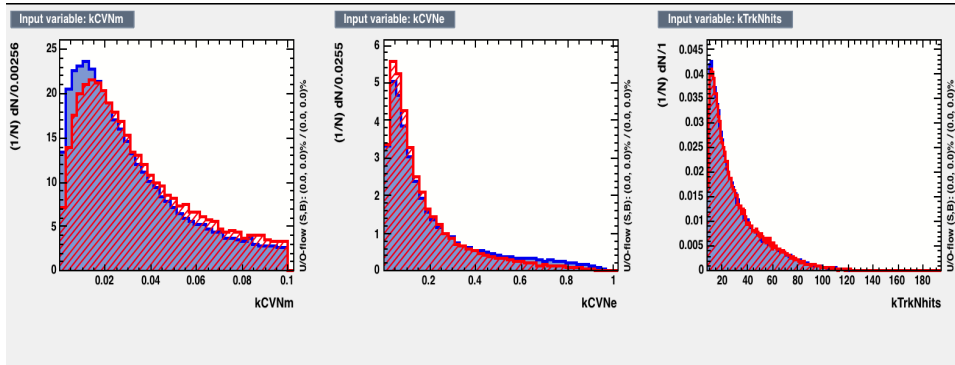
Figure 4.5: Input variables used while training BDT for NC $-\nu_\tau^{\text{had}}$ discriminant. Continued in the Figure 4.6.

Rank	Variable	Details
1	kNHit	Number of hits on track
2	kTrkNHits	Number of hits on track
3	kShwNHit	Number of hits in primary shower
4	kCVNnc	CVN NC classifier
5	kShwStartX	Shower X Start
6	kShwStopX	Shower X Stop
7	kShwEFrac	Fraction of slice energy in shower
8	kCVNm	CVN ν_μ classifier
9	kPtp	Transverse momentum fraction in slice
10	kShwStartZ	Shower Z Start
11	kCVNt	CVN ν_τ classifier
12	kRemIdMeasFrac	ReMId input variable, plane fraction
13	kRemIdScatLLH	Log-likelihood value from scattering angle
14	kShwWidth	Width of the primary shower
15	kCVNe	CVN ν_e classifier

Table 4.3: The ranking of the input variables used in BDT while training $NC-\nu_\tau^{\text{had}}$ discriminant. The variable rank, variable name and the details are given. The variable names used here are exactly the same as used in CAFAna.
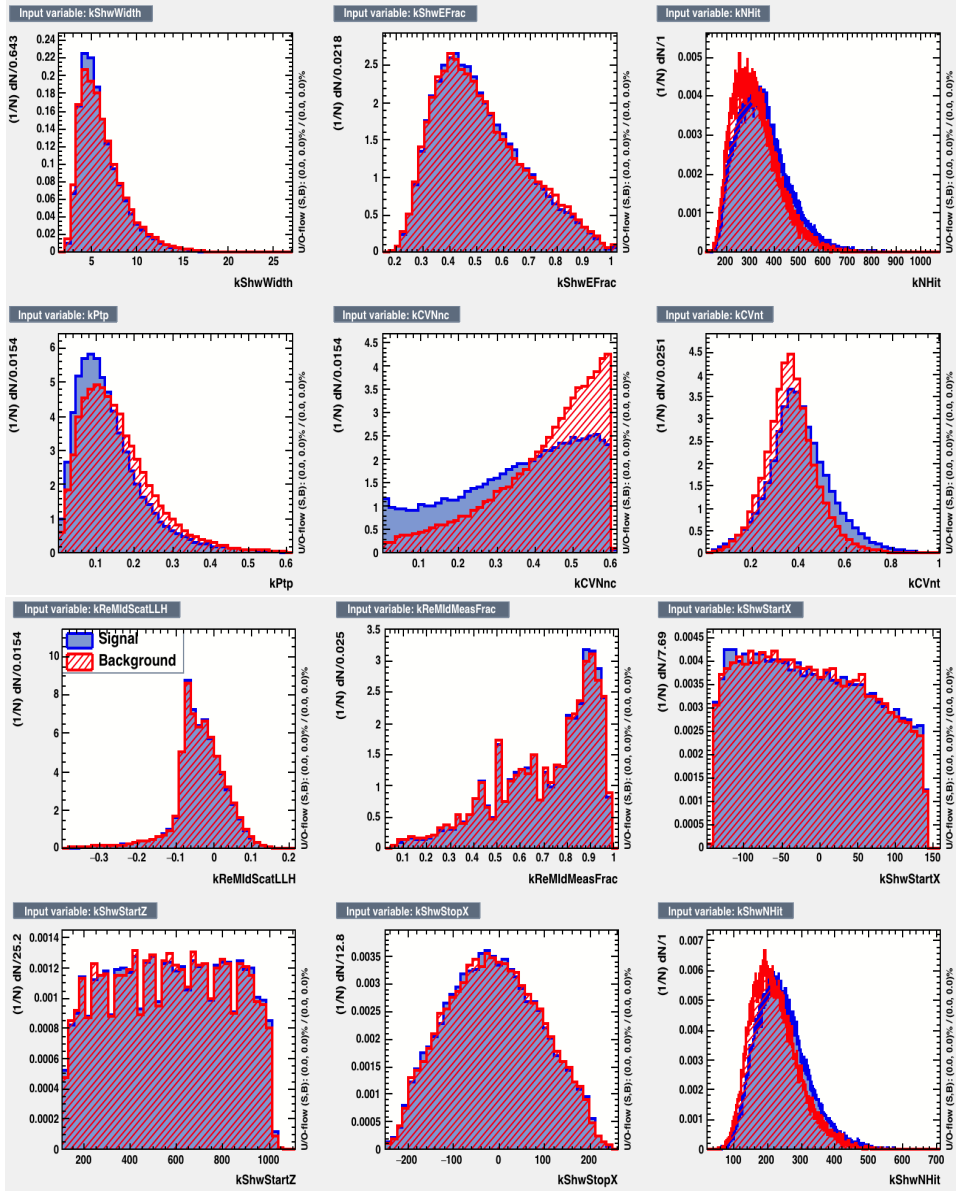
Figure 4.6: Input variables used while training BDT for NC $-\nu_\tau^{\text{had}}$ discriminant.

(a)   (b)
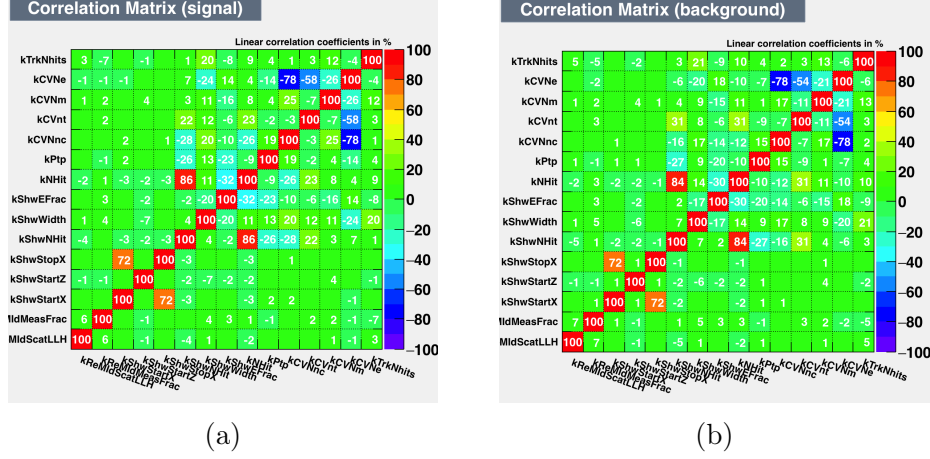
Figure 4.7: The linear correlation matrix for (a) ν_τ^{had} CC signal events and for (b) NC background events.

Input variables linear correlation

Figures 4.5 and 4.6 show the signal (blue) vs. background (red) separation performance for each BDT input variable post-training. Figure 4.7 is the resultant linear correlation matrices for the input variables when considering (a) signal or (b) background.

Training Results

The final BDT response is shown in Figure 4.8a. The BDT weight files are then used to produce a ν_τ^{had} PID data product and consequently fill CAF files with this product in order to produce Figure 4.8b, which breaks down the signal and background via the various neutrino interaction types: ν_μ CC, NC, ν_e CC, ν_τ CC and ν_τ^{had} CC.

(a) (b)
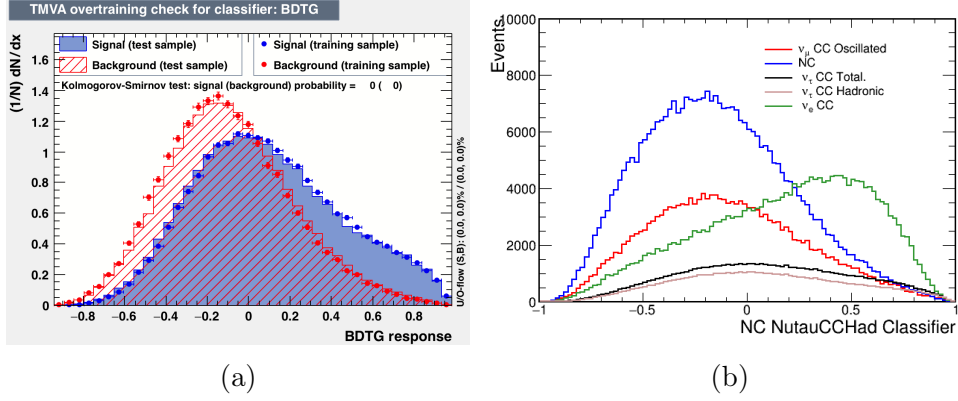
Figure 4.8: (a) BDT training and testing output for NC - ν_τ^{had} discriminator and (b) the BDT outputs when add to the CAF files. Preselection cuts mentioned in Table 4.1 are used. The two-flavor oscillation parameters used are $\Delta m^2 = 22$ eV^2 and $\theta_{\mu\tau} = 0.175$ rad.

We consider a two-flavor oscillation model to produce Figure 4.8b because we can approximate a 3+1 sterile oscillation model to a two-flavor model in the SBL approximation. We set the two-flavor parameters to a best sensitive parameter $\Delta m^2 = 22$ eV^2 and a mixing angle, $\theta = 0.175$ rad.

4.3.3 $\nu_\mu - \nu_\tau^{\text{had}}$ Discriminant

For $\nu_\mu - \nu_\tau^{\text{had}}$ discriminant, we train BDT assuming ν_μ CC interactions are the only background events and signal events are the hadronic ν_τ CC interactions.

Input variables

We considered only ν_μ CC background as the total background while training $\nu_\mu - \nu_\tau^{\text{had}}$ discriminant. We tried around 50 different variables as input variables to BDT and found a set of 15 variables gave the best figure of merit (S/B) when tested on ν_μ CC background versus hadronic ν_τ CC signal events. These all input variables are well defined in CAFAna package (`CAFAna/Vars`). A brief description of these variables are given Table 4.4. Figure 4.9 and 4.10 show the signal vs. background input variables of BDT training used for $\nu_\mu - \nu_\tau^{\text{had}}$ discriminant. The blue histogram shows the signal events and red histogram shows the background events.
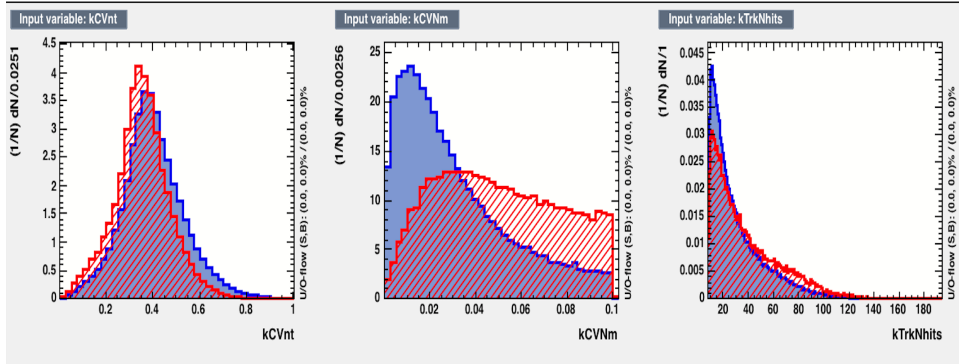
Figure 4.9: Input variables used while training BDT for $\nu_\mu - \nu_\tau^{\text{had}}$ discriminant. Continued in the Figure 4.10.

Rank	Variable	Details
1	kShwNHit	Number of hits on primary shower
2	kNHit	Number of hits in slice
3	kTrkNHits	Numberof hits in track
4	kCVNm	CVN ν_μ classifier
5	kPtp	Transverse momentum fraction in slice
6	kShwStopZ	Shower Z Stop
7	kShwStopX	Shower X Stop
8	kRemIdMeasFrac	RemId input variable, plane fraction
9	kShwStopY	Shower Y Stop
10	kShwEFrac	Fraction of slice energy in shower
11	kInelasticity	(slc.calE-shwlid.calE)/slc.calE
12	kCVNt	CVN ν_τ classifier
13	kELLT	Transverse log likelihood for electron
14	kTrkPlaneGap	No. of planes b/w reco vtx and start of track
15	kRemIdScatLLH	Log-likelihood value from scattering angle

Table 4.4: The ranking of the input variables used in BDT while training $\nu_\mu - \nu_\tau^{\mathrm{had}}$ discriminant. The variable rank, variable name and the details are given. The variable names used here are exactly the same as used in CAFAna.
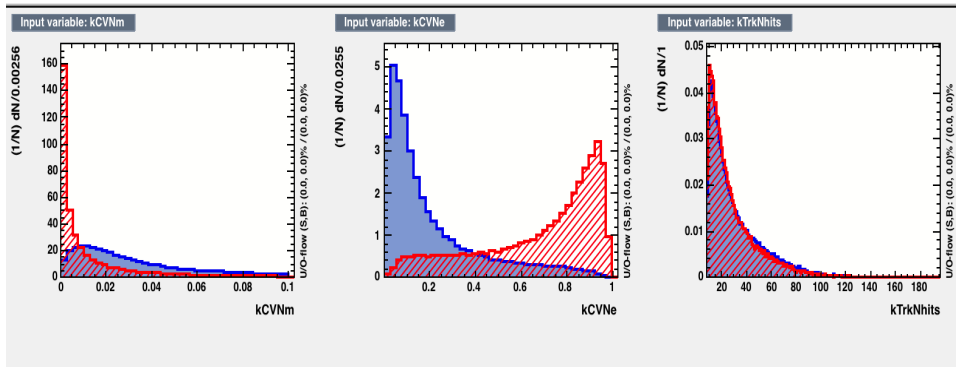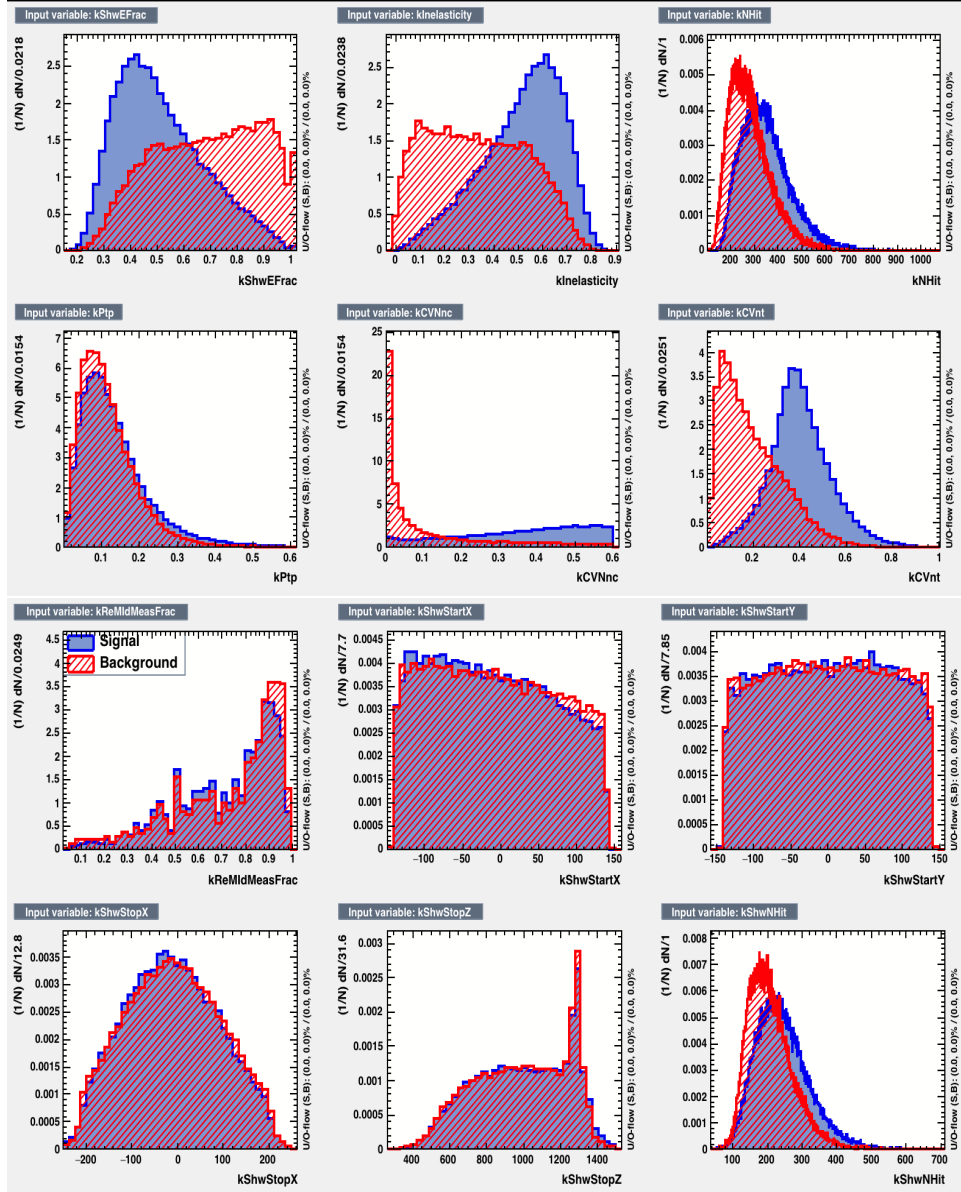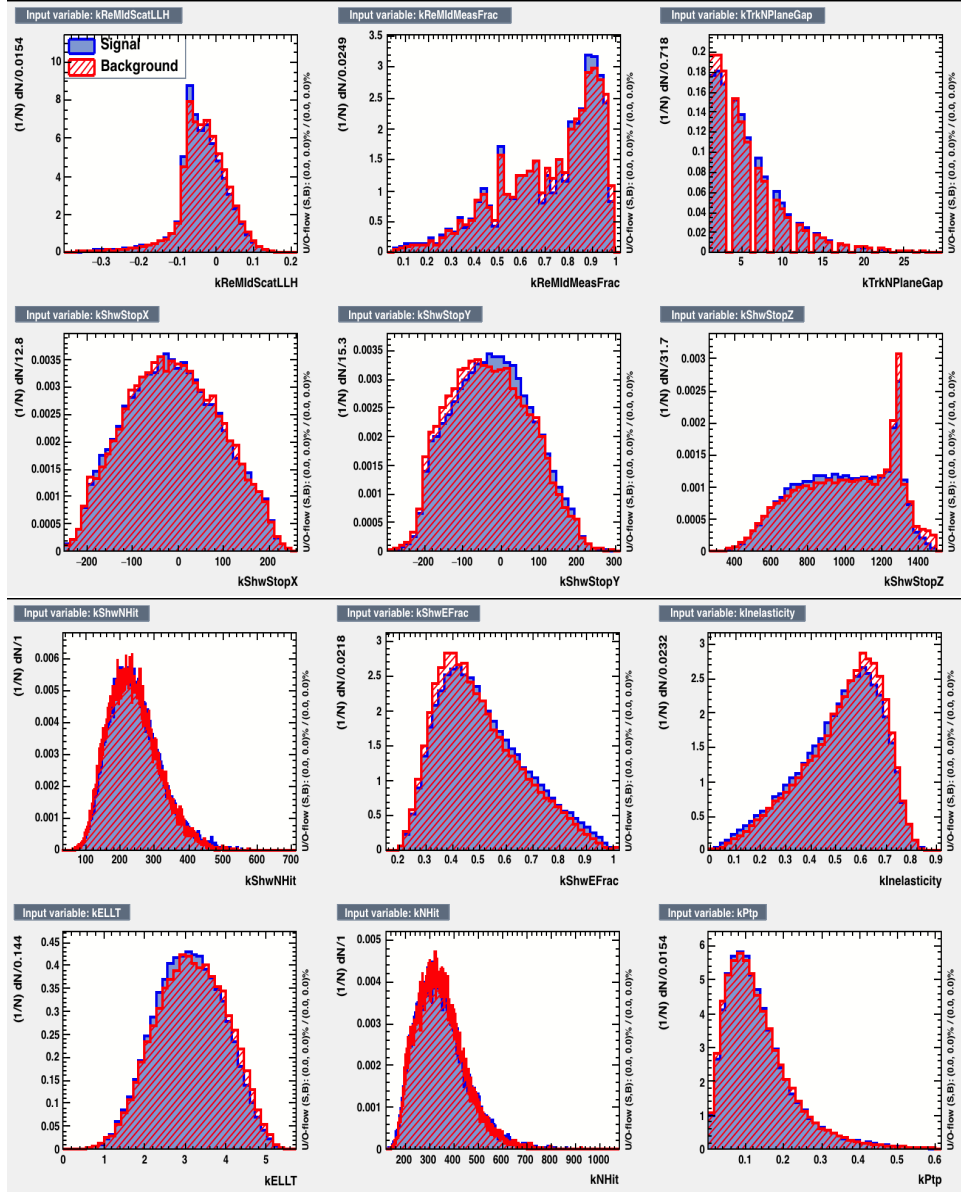
Figure 4.10: Input variables used while training BDT for $\nu_\mu - \nu_\tau^{\text{had}}$ discriminant.

Input variables linear correlation

Figures 4.9 and 4.10 show the signal (blue) vs. background (red) separation performance for each BDT input variable post-training. Figure 4.11 is the resultant linear correlation matrices for the input variables when considering (a) signal or (b) background.
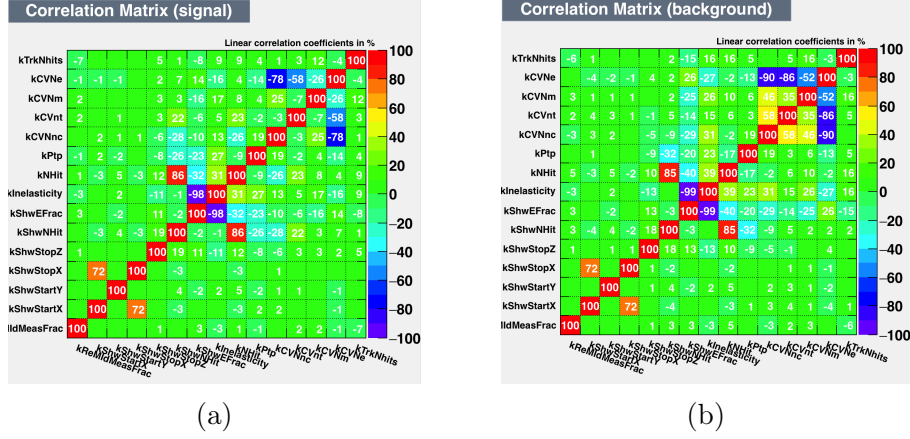

(a)   (b)
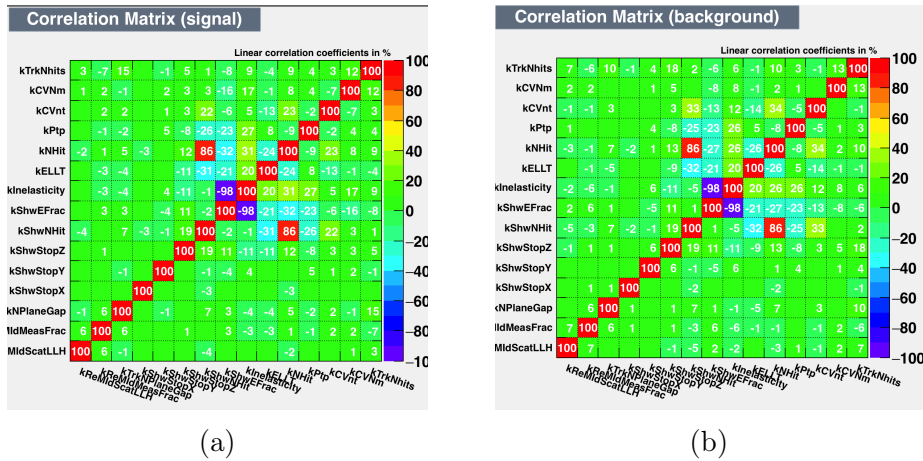
Figure 4.11: The BDT input variables linear correlation matrix for (a) signal and (b) background of $\nu_\mu - \nu_\tau^{\text{had}}$ discriminant.

Training Results

The final BDT response is shown in Figure 4.12a. The BDT weight files are then used to produce a ν_τ^{had} PID data product and consequently fill CAF files with this product in order to produce Figure 4.12b, which breaks down the signal and background via the various neutrino interac-
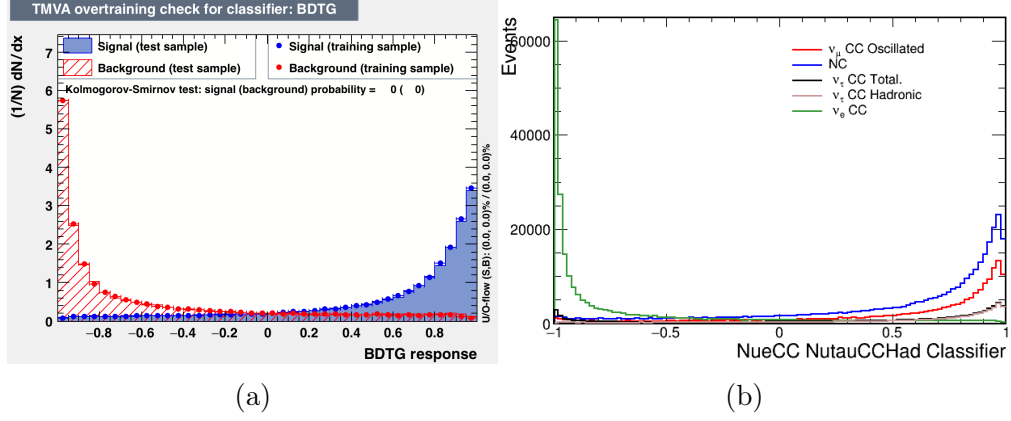
(a) (b)
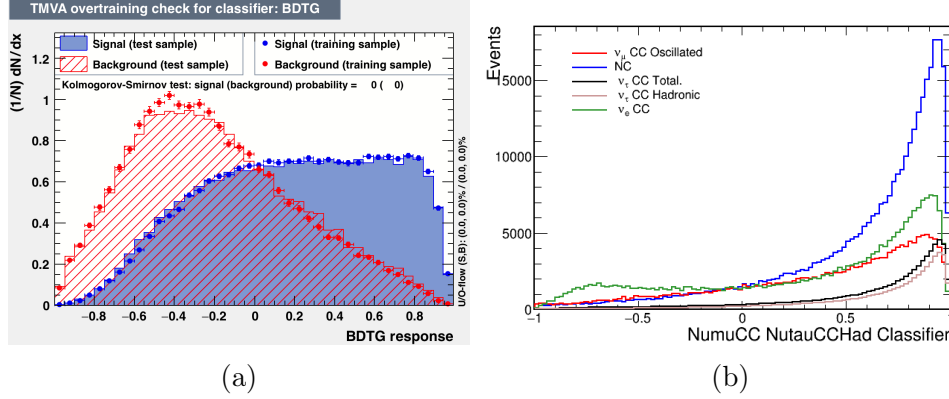
Figure 4.12: The BDT training and testing output for ν_μ - ν_τ^{had} discriminant (a) and the BDT outputs when add to the CAF files (b). Preselection cuts mentioned in Table 4.1 are used. The two-flavor oscillation parameters used are $\Delta m^2 = 22$ eV^2 and $\theta_{\mu\tau} = 0.175$ rad.

tion types: ν_μ CC, NC, ν_e CC, ν_τ CC and ν_τ^{had} CC.

We consider a two-flavor oscillation model to produce Figure 4.12b because we can approximate a 3+1 sterile oscillation model to a two-flavor model in the SBL approximation. We set the two-flavor parameters to a best sensitive parameter $\Delta m^2 = 22$ eV^2 and a mixing angle, $\theta = 0.175$ rad.

4.4   Sideband Studies

For validating the newly implemented BDT for ν_τ^{had} CC signal events, we used a low energy sideband region (calorimetric energy < 4.2 GeV) with all other preselection cuts mentioned in the Table 4.5. Data and MC events are studied using N-1 cut plots. The details are given below.

Cut Level	Cut Name	Cut Details
0	NoCut	kStandardSpillCuts
		kCaloE < 4 GeV
1	Fiducial Volume	+ kNDTauFiducial
2	Containment	+kNDTauContain
3	ν_μ Rejection	+CVNm < 0.1 (CVN numu classifier)
4	NC Rejection	+kCVNnc < 0.6 (CVN nc classifier)
5	Event Quality	+ kNTrks > 0(Number of tracks)
		+ kNShw > 0(Number of showers)

Table 4.5: The selection cuts used for the sideband study conducted for validating BDTs.

The cut flow used in BDT (These all are the cuts used for BDT training) are shown in Table 4.5. The data and MC event rates for each cut level are shown in Table 4.6. The number of events are summed over the calorimetric energy bins, MC events are scaled to data POT. The Figure 4.13 shows the N-1 cut plots for the side band cut levels shown in Table 4.6. The PIDs and calorimetric energy (GeV) distributions after all preselection cuts are shown in Figure 4.14.
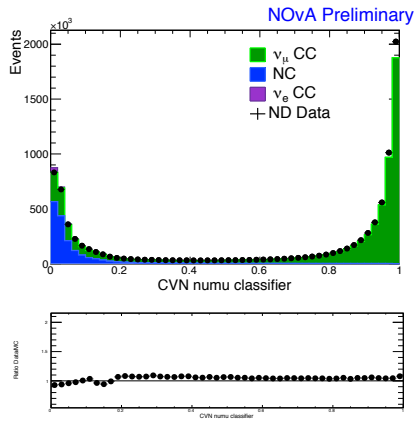
(a) CVN numu classifier
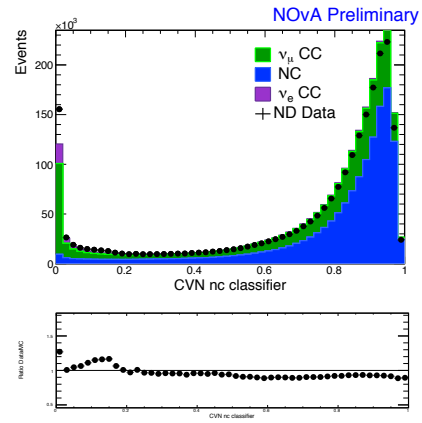
(b) CVN nc classifier
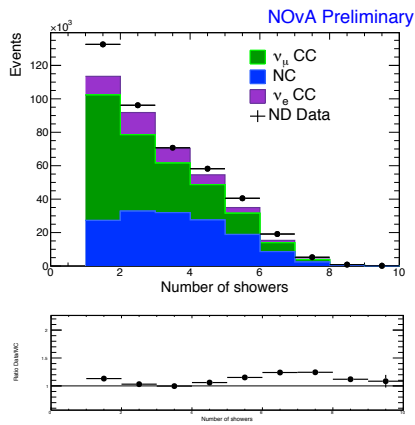
(c) Number of showers

Figure 4.13: The cut flow for sideband studies used for BDT validation. N-1 selection cuts are applied to all variables.
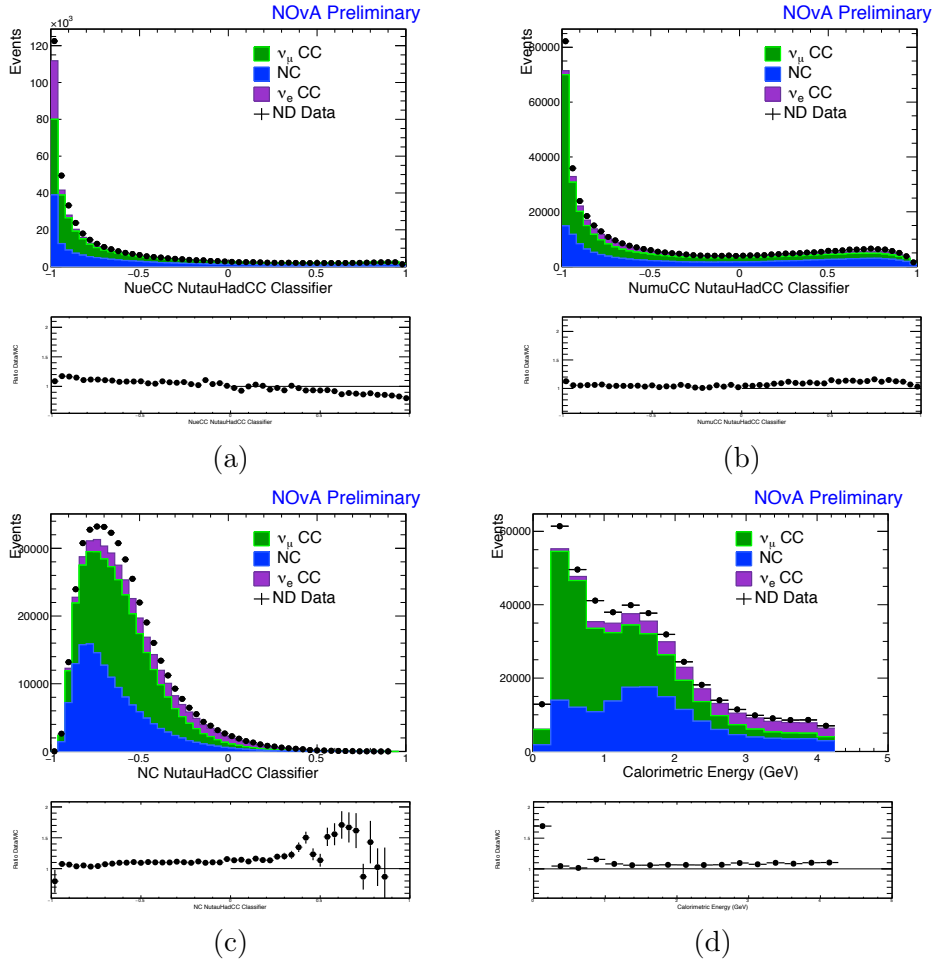
Figure 4.14: (a) $\nu_e - \nu_\tau^{\mathrm{had}}$ discriminant, (b) $\nu_\mu - \nu_\tau^{\mathrm{had}}$ discriminant, (c) NC $- \nu_\tau^{\mathrm{had}}$ CC discriminant and (d) calorimetric energy(GeV) distributions after all preselection cuts.

Cut Level	Cut Name	Data	MC	NC	ν_μ CC	ν_e CC	Ratio(Data/MC)
0	NoCut	1.29e+08	1.16e+08	1.39e+07	1.01e+08	1.27e+06	1.11
1	Fiducial Volume	1.05e+07	9.99e+06	2.28e+06	7.61e+06	98834.8	1.06
2	Containment	1.02e+07	9.65e+06	2.20e+06	7.35e+06	92783.2	1.06
3	ν_μ Rejection	2.25e+06	2.32e+06	1.40e+06	842027	65651.8	0.97
4	NC Rejection	538072	494718	180535	267396	46786.5	1.09
5	Event Quality	423456	385410	149888	191361	44160.3	1.10

Table 4.6: The data and MC event rates for each cut level. The number of events are summed over the calorimetric energy bins. MC events are scaled to data POT.

4.5   Results and Conclusions

We implement three different BDT outputs, based on BDTG variant, for separating ν_μ CC, ν_e CC and NC backgrounds from hadronic ν_τ CC signal events. The sideband studies shows they are showing good agreement with Data in the non-signal sideband region, before applying any cut on these BDTs. More details of signal selection optimization is shown in Ref. [69] and Chapter 5.

Chapter 5

Event Selections

This chapter describes the full process of event selection for the first SBL joint $\nu_\mu - \nu_\tau$ analysis in the NOvA ND. This SBL analysis uses an event topology-based event classifier called CVN in addition to a hadronic τ-decay mode particle identifier based on a boosted decision tree algorithm for the selection of ν_τ CC interactions. The event selection is performed giving priority to signal purity for reducing the large systematic uncertainties in the high energy region. We use a high energy ν_μ sample in addition to the ν_τ sample which helps to constrain most of the highly correlated systematics in the fit. Using these selected samples and all ND neutrino data of 8.06×10^{20} POT and prod-3 MC files, the final sensitivity to the 4-flavor parameters, Δm_{41}^2, $\sin^2 2\theta_{\mu\tau}$ and $\sin^2 \theta_{24}$, under 3+1 model assumption will be shown in Chapter 7.

5.1   Motivation

We investigate the SBL oscillations due to sterile neutrinos using the NOvA ND. The standard three-flavor neutrino oscillation parameters have been studied extensively by a wide range of neutrino experiments. However, the anomalous results, such as electron anti-neutrino excesses seen by LSND [70] and MiniBooNE [71], do not fit the three-flavor paradigm. This can be interpreted with an additional fourth flavor, a light sterile neutrino, at a larger mass scale than the existing three flavor neutrinos. The NOvA experiment consists of two finely segmented, liquid scintillator detectors operating 14.6 mrad off-axis from the NuMI muon neutrino beam. The NOvA ND is located at Fermilab campus, 105 m underground from the surface, 1 km from the beam source. This gives an L/E of 0.1–1 km/GeV for NOvA, comparable to the stated LSND L/E. This makes the ND well suited to search for anomalous SBL oscillations. This chapter will present a novel method for selecting ν_τ interactions at the ND using particle identifiers based on convolutional neural network and multivariate analysis technique.

5.2   3+1 Oscillation Model

We do not expect to observe any three-flavor neutrino oscillations in the ND nor any ν_τ produced in the beam. If we see ν_τ CC appearance in the ND, we can claim these arise from $\nu_\mu \to \nu_\tau$ oscillations. This can be

explained by adding a 'sterile neutrino' flavor to the standard three-flavor oscillation model, which can be further reduced to a two-flavor oscillation model using SBL approximations. The mixing of four neutrino flavors can be expressed as:

$$
\begin{pmatrix} \nu_e \\ \nu_\mu \\ \nu_\tau \\ \nu_s \end{pmatrix} = \begin{pmatrix} U_{e1} & U_{e2} & U_{e3} & U_{e4} \\ U_{\mu1} & U_{\mu2} & U_{\mu3} & U_{\mu4} \\ U_{\tau1} & U_{\tau2} & U_{\tau3} & U_{\tau4} \\ U_{s1} & U_{s2} & U_{s3} & U_{s4} \end{pmatrix} \begin{pmatrix} \nu_1 \\ \nu_2 \\ \nu_3 \\ \nu_4 \end{pmatrix},
\tag{5.1}
$$

where ν_s and ν_4 respectively are the flavor and mass eigenstates of the sterile neutrino, and $U_{\alpha i}$ (here $\alpha = e, \mu, \tau, s$ and i =1, 2, 3, 4) represents the mixing matrix element for active and sterile neutrinos.

For demonstration, we can approximate this four-flavor oscillation model to a two-flavor oscillation model in the SBL limit as shown below. Assuming no significant standard three-flavor oscillations in the ND, the probability for $\nu_\mu(\bar{\nu}_\mu) \to \nu_\tau(\bar{\nu}_\tau)$ appearance can be expressed as,

$$
P^{\text{SBL,3+1}}_{\nu_\mu(\bar{\nu}_\mu) \to \nu_\tau(\bar{\nu}_\tau)} = \sin^2 2\theta_{\mu\tau} \sin^2 \frac{\Delta m^2_{41} L}{4E},
\tag{5.2}
$$

where $\sin^2 2\theta_{\mu\tau} \equiv 4|U_{\mu4}|^2|U_{\tau4}|^2 = \cos^4 \theta_{14} \sin^2 2\theta_{24} \sin^2 \theta_{34}$, and oscillation probability for $\nu_\mu(\bar{\nu}_\mu) \to \nu_\mu(\bar{\nu}_\mu)$ disappearance can be written as,

$$
P^{\text{SBL,3+1}}_{\nu_\mu(\bar{\nu}_\mu) \to \nu_\mu(\bar{\nu}_\mu)} = 1 - \sin^2 2\theta_{\mu\mu} \sin^2 \frac{\Delta m^2_{41} L}{4E}.
\tag{5.3}
$$

where $\sin^2 2\theta_{\mu\mu} = \cos^2 \theta_{14}\sin^2 \theta_{24}$, E is the neutrino energy, $\theta_{\mu\tau}$ and $\theta_{\mu\mu}$
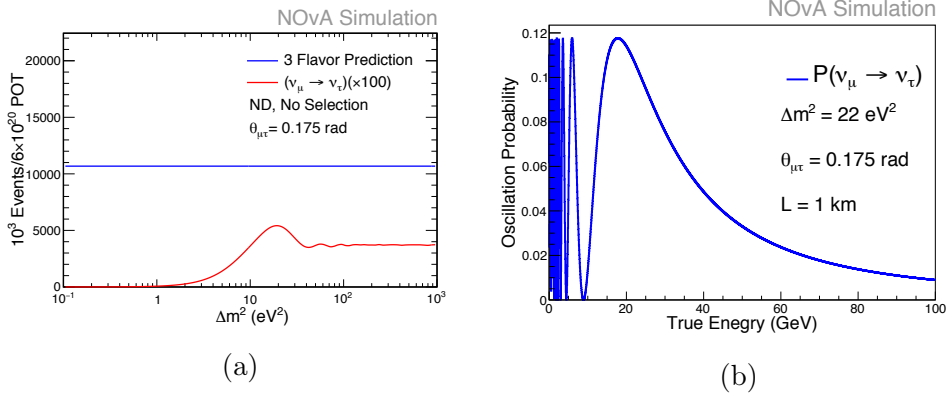
Figure 5.1: (a) ND event rates for different Δm^2 values, before selection. (b) Probability for $\nu_\mu \rightarrow \nu_\tau$ oscillations. The maximum ν_τ signal events are obtained at $\Delta m^2 = 22$ eV^2.

respectively are the mixing angles between the flavor eigenstates and mass eigenstates, and Δm_{41}^2 is the squared difference of the neutrino mass eigenstates.

The two-flavor approximation would not consider the oscillations of the significant backgrounds. Hence we use 3+1 oscillation model which is the simplest extension of the three-flavor model though there exist many others. This analysis will show the results of a 3+1 oscillation model based joint $\nu_\mu - \nu_\tau$ fit for the parameters Δm_{41}^2, $\sin^2 2\theta_{\mu\tau}$ and $\sin^2 \theta_{24}$. The expected ν_τ event rates before any selection as a function of Δm^2 with a fixed mixing angle, $\theta_{\mu\tau} = 0.175$ rad (an angle chosen as it is close to the point where we expect 90% C.L. sensitivity after adding all systematics) are shown in Figure 5.1a. The blue line shows the three flavor oscillated background prediction and the red line shows the signal event rates ($\times 100$). From Figure 5.1a, it is clear that the ν_τ appearance signal

gets maximized at $\Delta m^2 = 22$ eV^2. The two-flavor oscillation probability for $\nu_\mu \to \nu_\tau$ oscillations (blue line) with fixed parameters, $\Delta m^2 = 22$ eV^2 and $\theta_{\mu\tau} = 0.175$ rad. is shown in Figure 5.1b as a function of the true energy.

5.3 ν_τ Constraints from Previous Experiments

The NOMAD [80] and CHORUS [82] experiments are the two experiments which constrained oscillation parameters for the SBL $\nu_\mu \to \nu_\tau$ oscillations. No evidence for oscillation has been found and the new upper limits on the oscillation probability P($\nu_\mu \to \nu_\tau$) are more than an order of magnitude lower than the previous best experiment E531 [72] which ran at Fermilab in the 1980's.

5.4 Data and MC Samples, POT and Periods

The details of MC and data files used for this analysis are given below. All MC files used are processed in prod3. A special MC files for the ν_τ signal prediction in ND, which is more realistic than 'tau-swap' files, and full data files available are used in this analysis. We used 2017 cross section

and PPFX weights to the MC files (`kPPFXFluxCVWgt*kXSecCVWgt2017`).

5.4.1   Data files

Datasets were produced by the production group as a part of prod3. The ND data contains 8.06×10^{20} POT and data sets used are as follows,

- `prod_caf_R17-03-01-prod3reco.d_nd_numi_fhc_full`
  `_v1_goodruns`

5.4.2 ν_τ CC Overlay Samples

The nonswap samples for the background prediction and "tau-singles overlay" specialized files for the signal prediction are used. "tau-singles overlay" samples are made by switching ν_μ flavor to ν_τ flavor at the flux level and simulates one neutrino interaction per spill and then overlaid that one ν_τ event on the top of the nonswap files. This enables a more realistic files than the standard swap files, as we have one ν_τ on background of ν_μ events. More details of ND overlay samples can be found in Ref. [77].

The ND nonswap MC contains a total 3.5×10^{21} POT and is defined as,

- `prod_caf_R17-03-01-prod3reco.d_nd_genie_nonswap`
  `_fhc_nova_v08_full_v1`

The ND Tau Overlay MC is defined in the parent caf is of an overall POT of 2.9×10^{21} POT and is defined as,

- `prod_caf_R17-03-01-prod3reco.l_nd_genie_nonswap`
  `_fhc_nova_v08_full_cycle0_v1_nutaucc-overlay`

5.5 Analysis Framework

For three-flavor oscillations, the ND can be treated as being at a fixed oscillation length (L), but in the case of four-flavor oscillations we need to include the varying L to reflect the position at which the neutrino was produced assuming oscillations in ND. A neutrino could be produced anywhere in between the hadron production point and ND. For calculating the oscillation probability weights, we have to use the true distance each neutrino travels before interacting in the detector. The SBL framework makes a 2D histogram of 'True Length (km)/ True Energy (GeV)' vs. 'The Variable of Interest', analogous to oscillatable spectra in the standard CAFAna framework. Subsequently, events are weighted by the oscillation probability to get a 1D histogram of that variable. More details of the SBL-framework implemented in CAFAna are given in the technical note listed in Ref. [77].
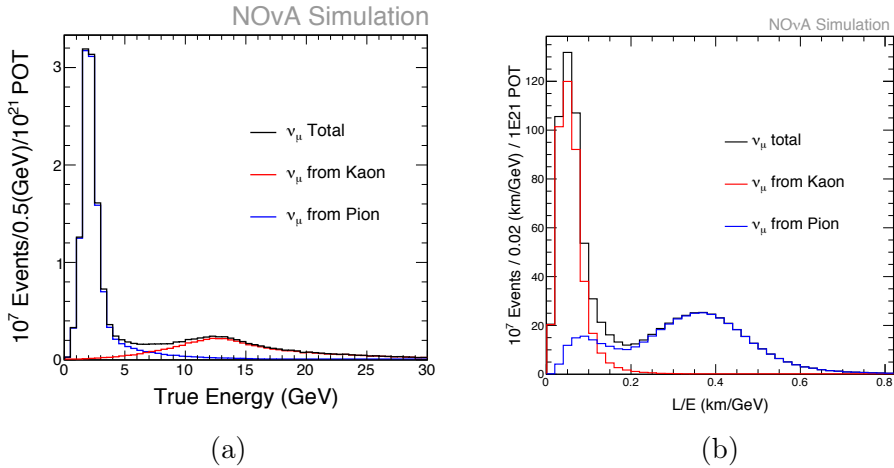
Figure 5.2: (a) True Energy (GeV) and (b) True Length (km)/True Energy (GeV) for ν_μs originating from pions and kaons in ND.

The true energy distribution of ν_μs originating from pion (blue line) and kaon (red line) are shown in Figure 5.2a. The True Length (km)/True Energy (GeV) distribution for the same ν_μs originating from pions (blue) and kaons (red) are shown in Figure 5.2b. The LSND and MiniBooNE experiments had an $L/E \geq 0.4$ km/GeV [70, 71], but the high energy tail of events from kaons gives access to lower L/E and sensitivities for $\Delta m^2 > 10$ eV^2.

5.6   Signal Selection and Prediction

The detection of an oscillation signal relies on the identification of ν_τ CC interactions using neutrino interaction event topology. The spatial resolution of the detector (~ 5 cm) does not resolve the τ decay ver-

tex (mean lifetime $\sim 3 \times 10^{-13}$ s and decay length $\sim$ mm) from the ν_τ CC interaction. The identification of ν_τ CC events is achieved by exploiting different neutrino interaction event topologies in the detector in addition to other properties of particles when the τ leptons decay in the detector.

The majority of events are likely to have a large amount of additional hadronic activity due to the hadronic recoil associated with these high energy events. An example hadronic ν_τ CC interaction is shown in Figure 5.3. This interaction is caused by an incoming neutrino with an energy of 13.9 GeV. The color indicates the charge deposited in the detector. Upper and lower plots are the top and side views, respectively in ND. In this interaction the τ lepton created decays to only hadrons, which is called a hadronic mode decay of the τ particle. The τ lepton will decay hadronically approximately 64.79% of the time and 17.82% into a ν_τ, e and $\bar{\nu}_e$ and 17.39% of the time into a ν_τ, μ and $\bar{\nu}_\mu$. The Table 2.1 shows the approximate branching fractions (%) of different τ decay modes, $h^{(+/-)}$ represents a charged hadron (either a π or a K). A hand scan ν_τ selection in ND showed $> 90\%$ of the selected ν_τ CC events are hadronic mode τ decays. Hence we decided to look at the hadronic ν_τ CC interactions in this analysis. We developed several BDTs for distinguishing ν_τ events from various background categories which use CVN event ID scores as well as other event properties assuming the signal events are hadronic mode ν_τ CC interactions.

Background arise from both misidentified NC, ν_μ CC and ν_e CC in-
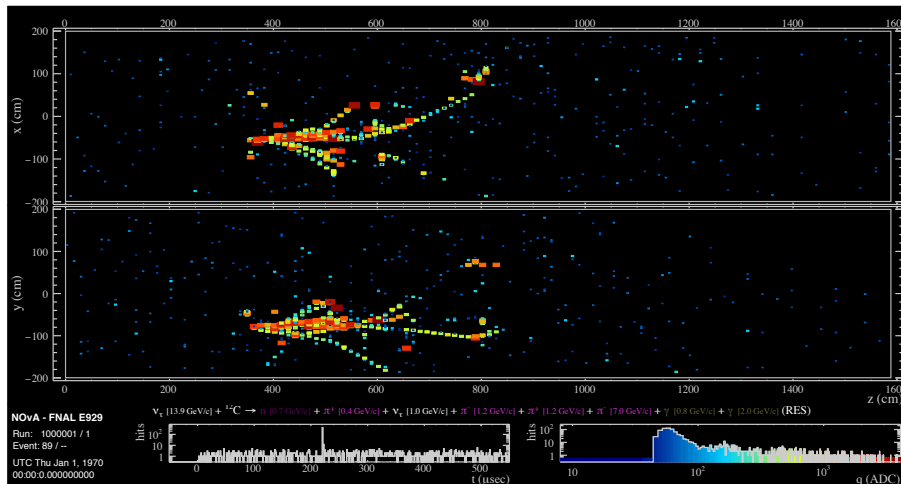
Figure 5.3: A simulated 13.9 GeV hadronic ν_τ CC event in the NOvA ND. Color indicates the charge deposited in the calorimeter. Upper and lower plot are the top and side views, respectively of this event in the detector.

teractions, and from neutrinos interacting outside the detector volume. In the background NC neutrino interactions, the neutrino leaves the detector with reduced energy and products of nuclear fragmentation remain behind. This hadronic recoil appears in the detector as an isolated cluster of energy deposits which may be mimicking hadronic ν_τ CC interactions. NuMI beam ν_μ CC and ν_e CC events, typically with high momentum transfer to the hadronic system, can be produced where the lepton may be mimicking a leptonic ν_τ CC interaction. The source of external background events are neutrino events interacting in the periphery of ND and in the surrounding cavern.

This analysis applies a rate only four-flavor joint fit for the parameters Δm_{41}^2 and $\theta_{\mu\tau}$ using $\nu_\mu \to \nu_\tau$ and $\nu_\mu \to \nu_\mu$ selections in ND. The

high energy $\nu_\mu \to \nu_\mu$ selection helps to constrain the correlated systematic uncertainties in the analysis. We use BDTs for ν_τ signal selection and the ν_μ CVN classifier (CVNm) for ν_μ signal selection as the primary classifiers as described below, and use a preselection that further improves the rejection of detector external activities arising from events in rock around the detector. The preselection includes a fiducial volume cut, which selects only the events with a reconstructed neutrino interaction vertex within a defined region inside the detector volume and a loose containment cut, which rejects the events in rock surrounding the detector.

5.6.1 CVN Event Classifier

NOvA has developed CVN [73] using tools to classify neutrino interactions, which is based on the GoogLeNet CNN architecture. The CNN's have been widely applied in the computer vision groups to solve complex problems in image recognition and analysis. The CVN treat each interaction as an image, and pass these images through layers consisting of banks of learned filters to extract the features of these images. These features are then used to classify events according to neutrino flavor and interaction type. Currently CVN is also used in the ν_e appearance [74], NC disappearance and ν_μ disappearance analyses in NOvA [75,76]. The files used for this analysis are prod3 version files in which the CVN2017 [73] version is implemented.

5.6.2 Hadronic ν_τ CC Event Selectors

The current CVN classifier we used in this analysis was trained for the FD ν_τ CC interactions without sub-classifying them on the basis of τ decay modes. The BDT training is done specifically for ν_τ CC interactions with hadronic decay of τ leptons. We tried different training methods listed in ROOT TMVA package for the PID training and found BDT gives the best results. We trained three BDT for separating ν_τ hadronic (ν_τ^{had}) events from NC, ν_e CC and ν_μ CC backgrounds [84]. As of now, those BDTs are called:

- NC $- \nu_\tau^{\mathrm{had}}$ discriminant

- $\nu_e - \nu_\tau^{\mathrm{had}}$ discriminant

- $\nu_\mu - \nu_\tau^{\mathrm{had}}$ discriminant

For $\nu_e - \nu_\tau{}^{\mathrm{had}}$ discriminant, we trained BDT assuming ν_e CC interactions are the only background events and signal events are defined as the hadronic ν_τ CC interactions. For NC $- \nu_\tau^{\mathrm{had}}$ discriminant, we trained BDT assuming NC interactions are the only background events and signal events are the hadronic ν_τ CC interactions. We considered only ν_μ CC background as the total background while training $\nu_\mu - \nu_\tau{}^{\mathrm{had}}$ discriminant. We trained over 100k signal and same number of background events and tested over the remaining 100k signal and background events.

A set of preselection cuts are used before preparing the input sam-

ples to BDT which remove a huge number background events. Also the fiducial volume and containment cuts are used to remove the detector external activities. The maximum possible background rejection are achieved using cuts based on a figure of merit defined as, FoM = Signal/Background, on CVN ν_μ and NC classifiers which rejects ν_μ CC and NC respectively without loosing ν_τ^{had} CC signal events. The event quality cuts (a minimum of one reconstructed vertex, one reconstructed track and one reconstructed shower) are also applied before preparing the input samples. A cut on calorimetric energy (kCaloE > 4.2 GeV) is applied to remove the majority of low energy background interactions. The detailed description of the BDT training is given in Chapter 4 [84].

5.7 Selection Details

As discussed before we have two samples, a ν_μ and a ν_τ sample. The details of both the selections are covered in this section. The ν_τ event selection is performed giving priority to signal purity for reducing the large systematic uncertainties in the high energy region of the backgrounds. More details of the selections are given below.

Fiducial Volume and Containment

For both the selections, a fiducial volume and a containment cut are applied to remove events originating outside of the detector. The fiducial

Cut Name	Reconstructed Quantity	Metric for Event to Pass
Fiducial Volume	Reco. Vertex X Coordinate	$-140\,\mathrm{cm} \leq vtxX \leq 140\,\mathrm{cm}$
	Reco. Vertex Y Coordinate	$-140\,\mathrm{cm} \leq vtxY \leq 140\,\mathrm{cm}$
	Reco. Vertex Z Coordinate	$100\,\mathrm{cm} \leq vtxZ \leq 1000\,\mathrm{cm}$
Containment	Reco. Slice Box Z Coordinate	$50\,\mathrm{cm} \leq boxminZ$

Table 5.1: Fiducial and containment cuts applied to events in the ND.

volume cut is a cut on the location of the reconstructed neutrino vertex. The containment cut rejects the event if the start or stop point is too close to the ND front wall (if it is < 50 cm from front wall). Unlike other analyses, no side or back containment is required, as this analysis selects very high energy events which are not often contained in the ND. These cuts are optimized for maximum selection efficiency. The same cuts are found to be optimal for both selections. The cut definitions, the reconstructed quantity over which each cut is applied and the metric to pass the events are given in Table 5.1.

ν_τ Selection

Two of the cuts in this selection, defined as 'kNDFiducial' and 'kND-Contain' are the same fiducial volume and containment cuts defined in Table 5.1. Table 5.2 summarizes the preselection cuts used for training the BDT. The details of the events passing each preselection cut for each component in the ν_τ prediction are given in the Table 5.3. Table 5.4 shows the cut flow up to the final selection. The corresponding N-1 cut plots which pass each selection cut stage in Tables 5.2 and 5.3 are shown in Figures 5.4 and 5.5 where each figure is a stacked prediction compo-

nent and the red dotted line shows the value of that variable over which we apply the cut, the arrow points in the direction of included region in the selection. The events are scaled to a data POT of 8.06×10^{20}.

Cut Level	Cut	Details
Data Quality	kStandardSpillCuts	Standard NuMI Spill Cuts Defined in CAFAna
Event Quality	+(kNTrks > 0)	Number of tracks
	+(kNShw > 0)	Number of showers
	+kNDFiducial	
	+kNDContain	Details are given in Table 5.1
BDT Preselection	+(4.2 < kCaloE < 40.)	Calorimetric Energy (GeV)
	+(kCVNm < 0.1)	CVN ν_μ classifier
	+(kCVNnc < 0.6)	CVN NC classifier

Table 5.2: Preselection cut applied in ν_τ selection.

Cut Level	ν_τ CC	NC	ν_μ CC	ν_e CC	Tot. Bkg.	Ratio(%) S/B
Data Quality	364269	1.51187e+07	1.12707e+08	1.65769e+06	1.29983e+08	0.28
Event Quality	81887	2.71764e+06	9.54503e+06	221597	1.24843e+07	0.66
BDT Preselection	40943	182202	95554	113485	391242	10.47

Table 5.3: The number of events that pass the ν_τ preselection cuts. Scaled to 8.06×10^{20} POT, $\Delta m^2_{41} = 22$ eV^2 and $\theta_{\mu\tau} = 0.175$ rad.

Cut Level	ν_τ CC	NC	ν_μ CC	ν_e CC	tot.bkg	Ratio(%) S/B
Preselection	40943	182202	95554	113477	391232	10.47
+($\nu_e - \nu_\tau^{\mathrm{had}}$ Discriminant > 0)	28597	151698	80377	15401	247476	11.56
+($NC - \nu_\tau^{\mathrm{had}}$ Discriminant > 0.8)	934	666	636	567	1869	49.96
+($\nu_\mu - \nu_\tau^{\mathrm{had}}$ Discriminant > 0)	866	591	460	541	1591	54.44

Table 5.4: The number of events that pass the ν_τ selection cuts at ND (scaled to 8.06×10^{20} POT, Δm_{41}^2 = 22 eV^2 and $\theta_{\mu\tau}$ = 0.175 rad.).

ν_μ Selection

The ν_μ selection is performed using CVN ν_μ classifier and a set of preselection cuts. The preselection includes the same fiducial and containment cuts defined in Table 5.1, a calorimetric energy cut (4.2 GeV < kCaloE < 40 GeV) to select the high energy ν_μ events which disappear when ν_τ events appear. In addition to that we used the same standard NuMI spill cuts for ND. The details of ν_μ selection cuts are shown in Table 5.5 and the number of events passing those selection cuts are shown in Table 5.6. Figure 5.6 shows the N-1 cut plots passing the selection cuts defined in Tables 5.5 and 5.6. The plots are scaled to a data POT of 8.06×10^{20} and used a fixed four-flavor oscillation parameters, $\Delta m_{41}^2 = 22$ eV^2 and $\theta_{\mu\tau} = 0.175$ rad.
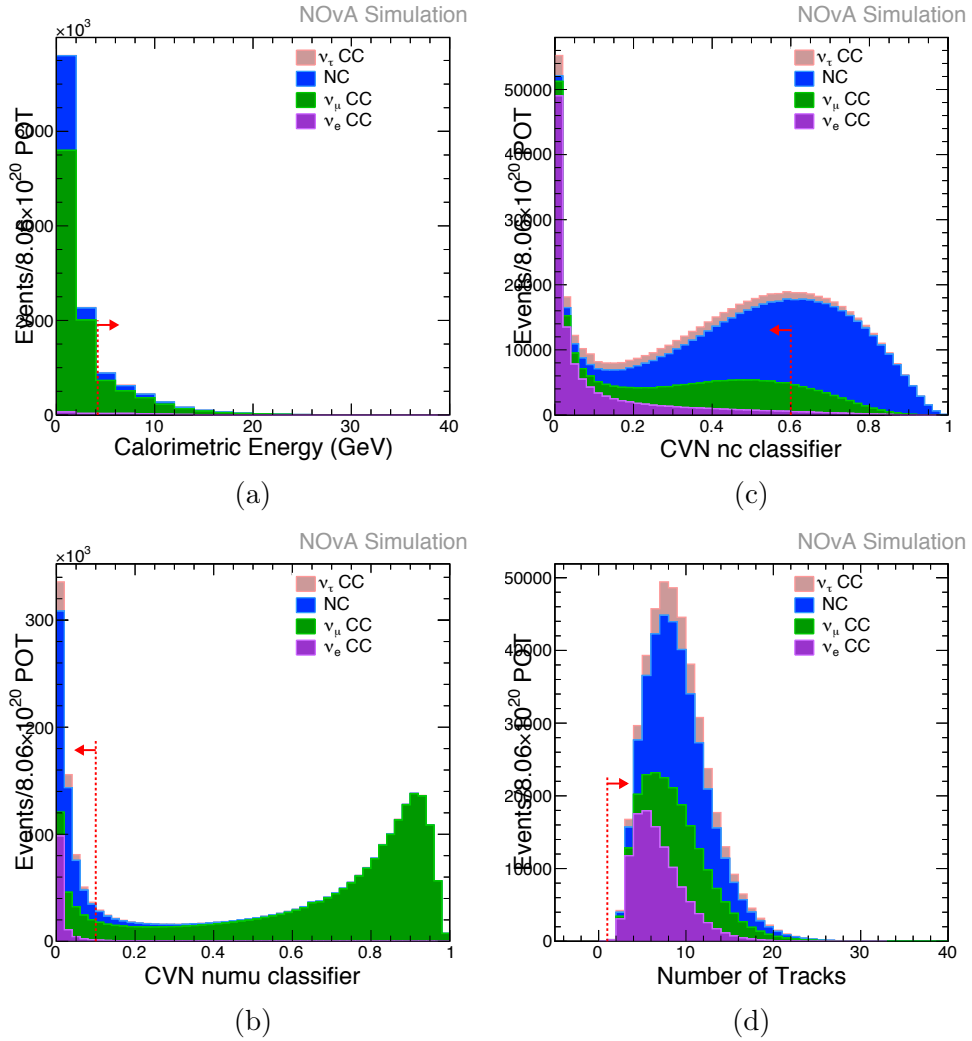
Figure 5.4: N-1 cut plots for ν_τ selection at ND. The plots are scaled to a data POT of 8.06×10^{20} and used a fixed four-flavor oscillation parameters, $\Delta m^2_{41} = 22$ eV^2 and $\theta_{\mu\tau} = 0.175$ rad. Continued in the Figure 5.5
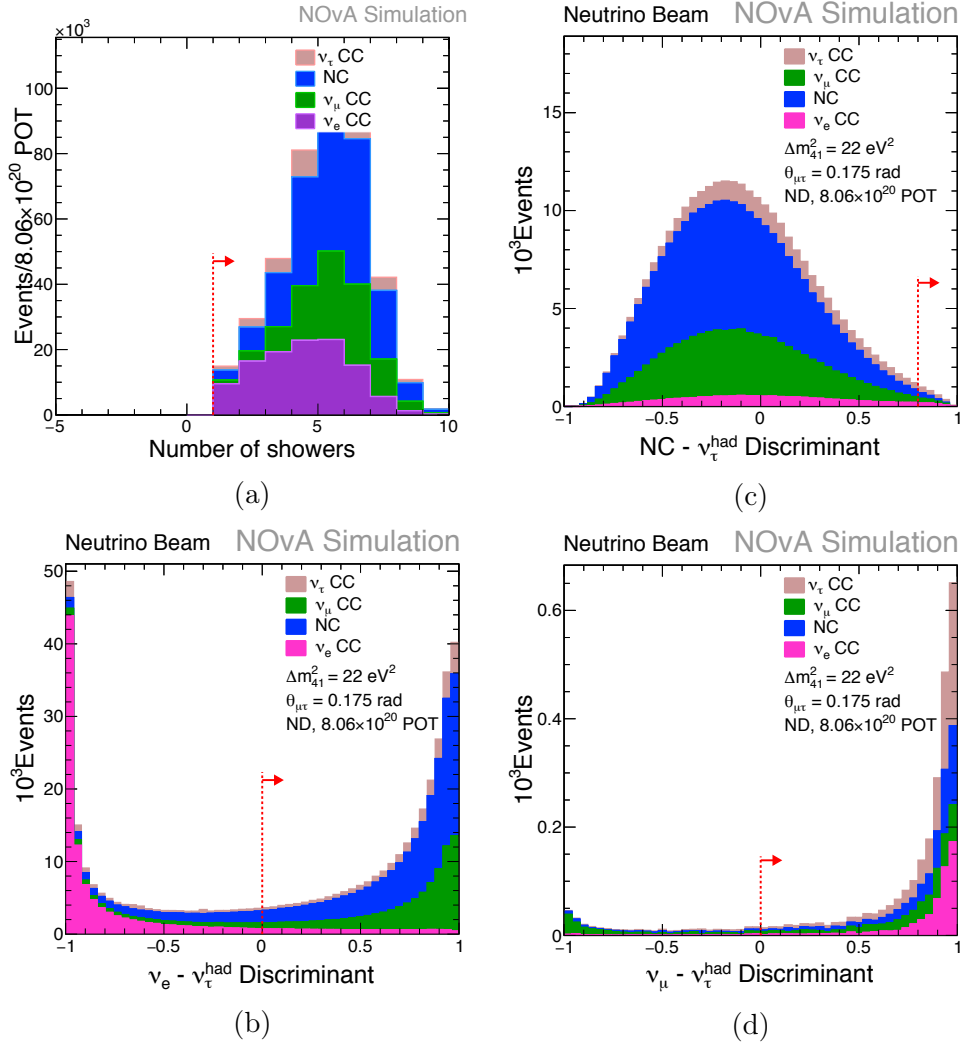
Figure 5.5: N-1 cut plots for ν_τ selection at ND. The plots are scaled to a data POT of 8.06×10^{20} and used a fixed four-flavor oscillation parameters, $\Delta m^2_{41} = 22$ eV^2 and $\theta_{\mu\tau} = 0.175$ rad.

Cut Level	Cut	Details
Data Quality	kStandardSpillCuts	Standard NuMI Spill Cuts Defined in CAFAna
Event Quality	kNDFiducial	Details are given in Table 5.1
	+kNDContain	
	+(4.2 GeV < kCaloE < 40. GeV)	Calorimetric Energy(GeV)

Table 5.5: ν_μ preselection cuts at ND.

Cut Level	ν_μ CC	NC	ν_τ CC	ν_e CC
ν_μ Preselection	1.9e+06	440908	65695	125665
+(kCVNm > 0.5)	1.52e+06	14252	6694	2063

Table 5.6: The number of events that pass the ν_μ selection cuts at the point $\Delta m_{41}^2 = 22$ eV^2 and $\theta_{\mu\tau} = 0.175$ rad. for 8.06×10^{20} POT.
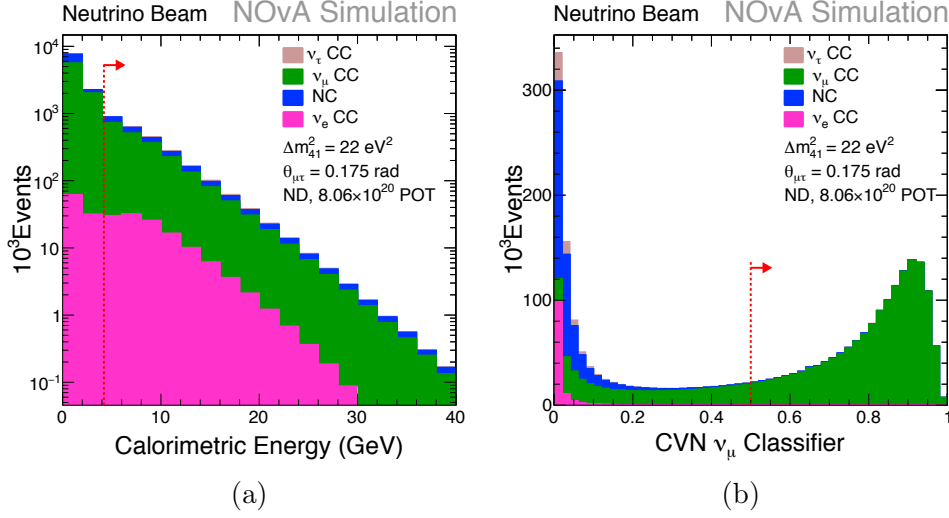
Figure 5.6: N-1 cut plots for ν_μ selection at ND. The plots are scaled to a data POT of 8.06×10^{20} and used a fixed four-flavor oscillation parameters, $\Delta m_{41}^2 = 22$ eV^2 and $\theta_{\mu\tau} = 0.175$ rad.

Signal Predictions

Table 5.7 shows the number of predicted neutrino events for $\nu_\mu \rightarrow \nu_\mu$ and $\nu_\mu \rightarrow \nu_\tau$ selections at the point $\Delta m_{41}^2 = 22$ eV^2 and $\theta_{\mu\tau} = 0.175$ rad. for 8.06×10^{20} POT. Figures 5.7 and 5.8 shows the corresponding spectra for both the ν_μ and ν_τ predictions in calorimetric energy (GeV) bins. We expect a total of 1.2×10^5 disappearing ν_μ events ($\sim 8\%$) and 1.5×10^6 remaining ν_μ events in $\nu_\mu \rightarrow \nu_\mu$ selection. Also a total of 866 ν_τ events are expected in $\nu_\mu \rightarrow \nu_\tau$ selection at this oscillation point for 8.06×10^{20} POT.

Selection	ν_μ **CC**	**NC**	ν_e **CC**	ν_τ **CC**	$\frac{S}{(S+B)}(\%)$
$\nu_\mu \to \nu_\mu$	1.52e+06	14252	2063	6694	98.5
$\nu_\mu \to \nu_\tau$	460	591	541	866	35.2

Table 5.7: The neutrino events passing $\nu_\mu \to \nu_\mu$ and $\nu_\mu \to \nu_\tau$ selections at the point $\Delta m_{41}^2 = 22$ eV^2 and $\theta_{\mu\tau} = 0.175$ rad. for 8.06×10^{20} POT.
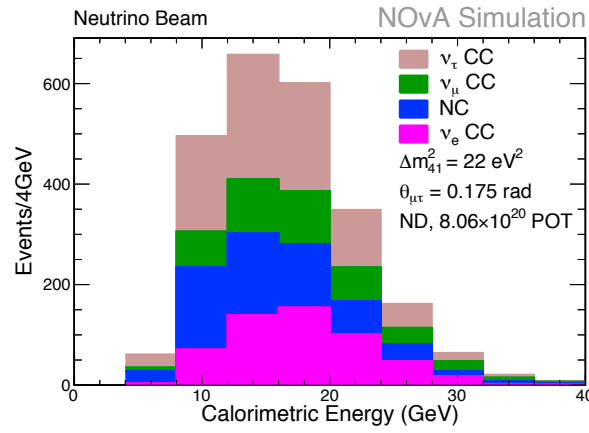
Figure 5.7: Simulated calorimetric energy distribution for $\nu_\mu \to \nu_\tau$ selection at the point $\Delta m_{41}^2 = 22$ eV^2 and $\theta_{\mu\tau} = 0.175$ rad. scaled to 8.06×10^{20} POT.
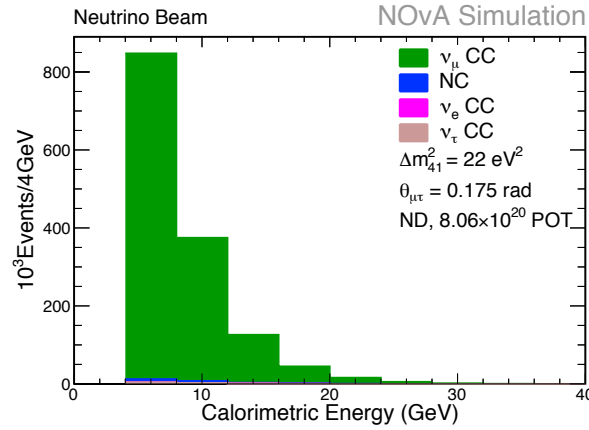
Figure 5.8: Simulated calorimetric energy distribution for $\nu_\mu \to \nu_\mu$ selection at the point $\Delta m_{41}^2 = 22$ eV^2 and $\theta_{\mu\tau} = 0.175$ rad. scaled to 8.06×10^{20} POT.

Chapter 6

Systematic Uncertainties

The ν_τ appearance analysis is sensitive to a number of systematic uncertainties. NOvA was designed to minimize these systematics using ND data for a FD MC prediction, but this analysis uses only ND. However this analysis finds an alternate method to reduce these uncertainties. A joint $\nu_\mu \to \nu_\tau$ and $\nu_\mu \to \nu_\mu$ fit helps to constrain most of the highly correlated systematics as many effects such as beam and cross section uncertainties which affect the $\nu_\mu \to \nu_\tau$ and $\nu_\mu \to \nu_\mu$ selections in a similar or same way.

The general technique used for calculating the systematics in the ND is the generation of the prediction without ("nominal") and with an applied systematic ("shifted") and calculate the difference between the two spectra. The difference between these spectra are quantified as the systematic uncertainty. Even though we show the full distribution of every systematic separately, we will only include the effect on integral in the analysis (sum in quadrature), as this analysis will be performed as a

rate analysis.

The systematic effects analyzed included uncertainties arising from
GENIE simulation, neutrino flux, light yield simulation, Cherenkov pho-
ton, miscalibration, ND rock-event contamination and overall normaliza-
tion. The details are given below.

6.1   Data Sets

The following are the MC data sets used for quantifying the systematic
uncertainties discussed in this technical note. We produce the spectra in
calorimetric energy bins after applying all the selection cuts for both the
$\nu_\mu \to \nu_\tau$ and $\nu_\mu \to \nu_\mu$ selections and compare each distribution produced
for the shifted vs. nominal cases. For light level systematics, we replace
"nominal" by a "no shift" sample due to the reasons described in Ref. [86].
The details of the data sets used are given in Appendix A.1.

6.2   GENIE Systematics

NOvA uses GENIE, a generator that involves a detailed physics modeling
of cross sections, hadronization, and final state interactions for the neu-
trino interaction simulations in the detectors. The cross section reweight-
ing is built into GENIE. Complete descriptions for all of the reweightable
GENIE cross section parameters (knobs) can be found in the GENIE

user's manual [93], which has been adapted into Tables A.1 and A.2 in Appendix A. Furthermore, Table A.3 and A.4 shows the cross section uncertainties calculated for the parameters mentioned in Tables A.1 and A.2 for the ν_τ selection. The overall calculated cross section systematic uncertainty on the ν_τ signal is 16.04% and the background is 20.14%. Tables A.5 and A.6 shows the cross section uncertainties calculated for the parameters mentioned in Tables A.1 and A.2 for the ν_μ selection. The overall systematic uncertainty on the ν_μ signal is 20.87% and on the background is 21.68%.

6.2.1   Large and Small Shifts

Since there are many reweight knobs, it would be impractical to include all of them in the thesis. Instead, the knobs with the largest shifts ($> 1\%$ shift) for ν_τ selection are shown in the Figures 6.2– 6.4 and the same for ν_μ selection is shown in Figures 6.5 – 6.9. The shifts from all these knobs are summed in quadrature and included as one systematic error. In this analysis we considered the cross section systematics as 'small cross section systematics' if the values are less than 1% and all other cross section systematics as the 'large cross section systematics'. The summary of large GENIE systematics and the sum in quadrature of all small GENIE systematics are shown in Tables 6.1 and 6.2 respectively. The numbers in bold letters show the large cross section uncertainties.

Systematic Parameter	ν_μ Signal		Background	
	(%) +1σ	(%) -1σ	(%) +1σ	(%) -1σ
PD3_DISvnCC1pi	**1.828**	**1.828**	0.4152	0.4152
PD3_DISvnCC2pi	**2.158**	**2.158**	0.491	0.491
PD3_DISvnCC3pi	**4.156**	**4.156**	**1.771**	**1.771**
PD3_DISvpCC3pi	**1.664**	**1.664**	0.959	0.959
PD3_MECq0ShapeSyst2017	**1.533**	0.443	0.819	0.384
PD3_RPACCQEEnhSyst2017	**3.961**	**3.430**	**2.029**	**1.961**
ReweightAhtBY	**1.133**	**1.132**	0.704	0.701
ReweightBhtBY	**1.252**	**1.261**	**1.422**	**1.464**
ReweightFormZone	**4.952**	**14.040**	**7.411**	**19.620**
ReweightMFP_N	**1.015**	**1.155**	0.686	0.823
ReweightMFP_pi	**1.605**	**1.792**	**2.212**	**2.518**
ReweightMaCCRES	**3.316**	**2.889**	0.3451	0.296
ReweightMvCCRES	**1.641**	**1.335**	0.161	0.130
sum of all small GENIE Systs.	1.797		1.617	
sum of all GENIE Systs.	16.040		35.870	

Table 6.1: The percentage difference between the shifted and nominal predictions for the number of selected $\nu_\mu \rightarrow \nu_\tau$ ND events due to neutrino interaction cross section systematics.

Systematic Parameter	ν_μ Signal		Background	
	(%) +1σ	(%) -1σ	(%) +1σ	(%) -1σ
PD3_DISvnCC1pi	2.510	2.510	0.358	0.358
PD3_DISvnCC2pi	3.162	3.162	0.360	0.360
PD3_DISvnCC3pi	7.287	7.287	0.739	0.739
PD3_DISvnNC3pi	0	0	3.167	3.167
PD3_DISvpCC0pi	1.656	1.656	0.206	0.206
PD3_DISvpCC2pi	1.391	1.391	0.191	0.190
PD3_DISvpCC3pi	4.233	4.233	0.477	0.477
PD3_DISvpNC0pi	0	0	1.031	1.031
PD3_DISvpNC3pi	0	0	3.114	3.114
PD3_RPACCQEEnhSyst2017	3.049	2.864	0.406	0.358
ReweightAhtBY	1.217	1.222	0.923	0.925
ReweightBhtBY	1.953	2.003	1.702	1.752
ReweightCV1uBY	1.144	1.224	1.085	1.155
ReweightCV2uBY	1.067	1.067	1.006	1.006
ReweightFormZone	6.806	17.790	7.184	20.64
ReweightMFP_pi	2.769	2.986	3.064	3.355
ReweightMaCCRES	1.227	0.812	0.279	0.223
sum of all small GENIE Systs.	1.288		1.644	
sum of all GENIE Systs.	20.870		21.680	

Table 6.2: The percentage difference between the shifted and nominal predictions for the number of selected $\nu_\mu \rightarrow \nu_\mu$ ND events due to neutrino interaction cross section systematics.

6.2.2   The ν_τ Cross Section Uncertainties

We have estimated an uncertainty of 16.04% for ν_τ cross section using the existing cross section models implemented in customized version of GENIE in NOvA, which assumes all leptons have the same behavior, but the τ cross sections are not well studied yet. Hence for the ν_τ, an overall scaling of 50% is applied on the ν_τ CC events, which is the same value used by the MINOS experiment [85], based on the conversations with Hugh Gallagher. The GENIE predicted cross section for ν_τ CC events in ^{12}C nucleus are shown in Figure 6.1. The black line shows the overall cross section, the blue line is QE, the green line is RES and red line indicates DIS. The plot shows the over all ν_τ CC interactions in the detector are dominated by DIS events.

6.3   Beam Systematics

Understanding the NuMI neutrino flux is crucial for the SBL τ neutrino oscillation search, since it enters directly into the measurement. The NOvA MC simulation includes the latest model of NuMI beam process to create the most realistic MC, but mismodeling can result in mismatch between the simulation and the real detector data. The NOvA Beam Working Group performed studies to calculate the effect that uncertainties in the simulation can have on the NuMI neutrino flux. These studies include the effects of incorrect modeling of various parts of the beam
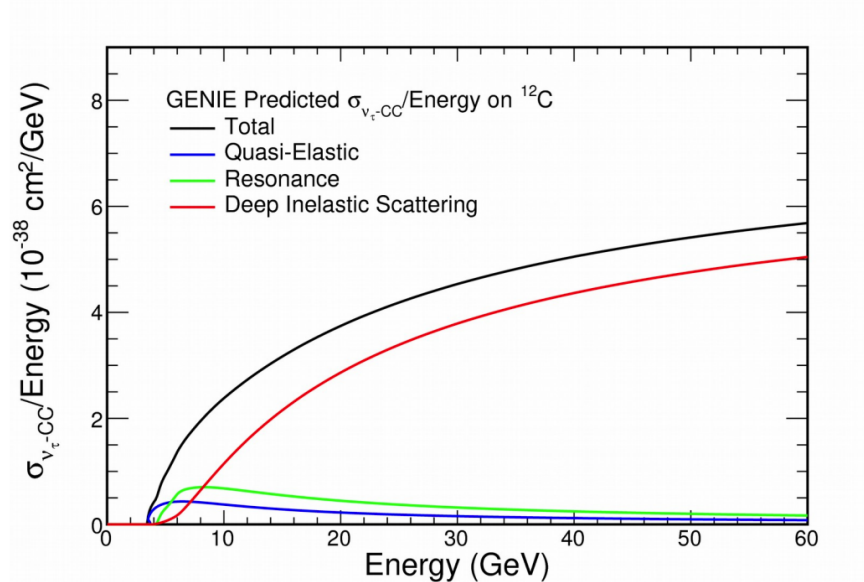
Figure 6.1: The GENIE predicted cross section for ν_τ CC events in ^{12}C nucleus.

transport and the effects of uncertainties in hadron production arising from fixed target experiments.

6.3.1   Beam Transport Systematics

The beam transport systematics are quantified using a sample flux generated using a systematic shift and compared to the nominal flux via simple ratio. The uncertainties considered include the horn and target position, the horn current, the beam position on the target and the beam spot size. Results were generated for both ν_μ and ν_τ selection, signal and backgrounds separately. The individual uncertainties are added in

(a)
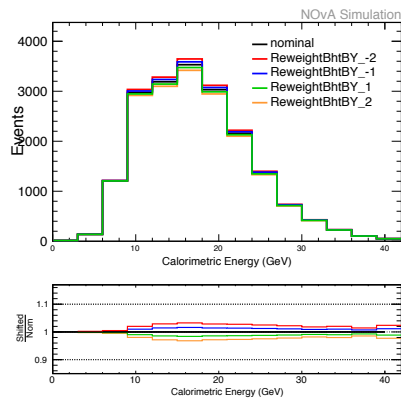
`ReweightBhtBY` systematics for signal events passing ν_τ CC selection.
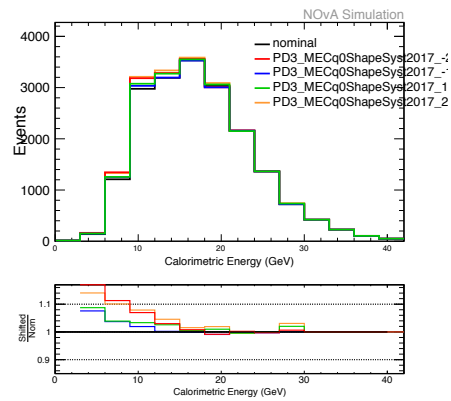
(c)

`PD3_MECq0ShapeSyst2017` systematics for signal events passing ν_τ CC selection.
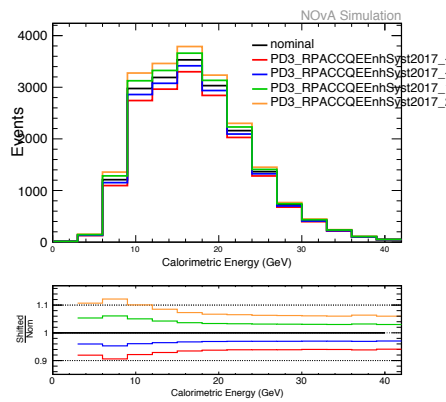
(b)

`PD3_RPACCQEEnhSyst2017` systematics for signal events passing ν_τ CC selection.
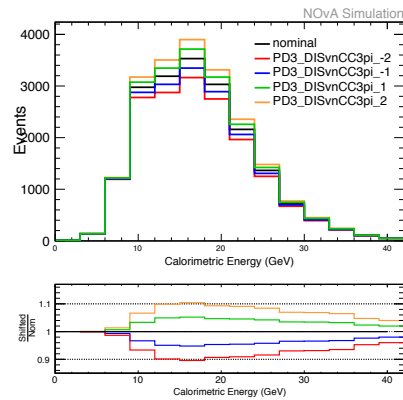
(d)

`PD3_DISvnCC3pi` systematics for signal events passing ν_τ CC selection.

Figure 6.2: Large GENIE systematics for the events passing ν_τ selection. Continued in the Figure 6.3.
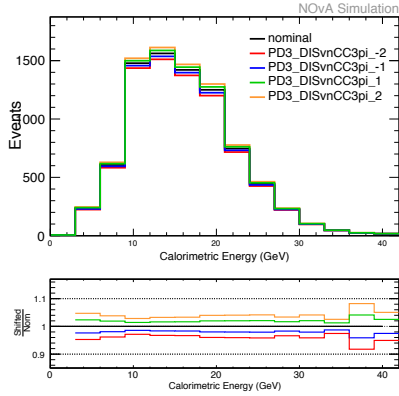
(a)
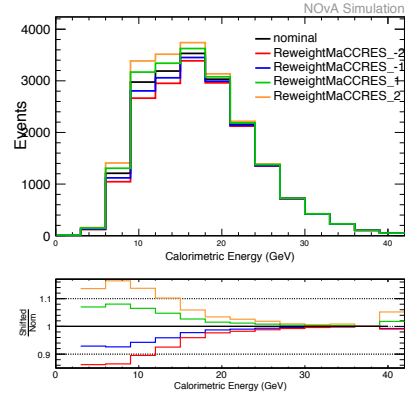
`PD3_DISvnCC3pi` systematics for background events passing ν_τ CC selection.

(b)

`ReweightFormZone` systematics for signal events passing ν_τ CC selection.

(c)
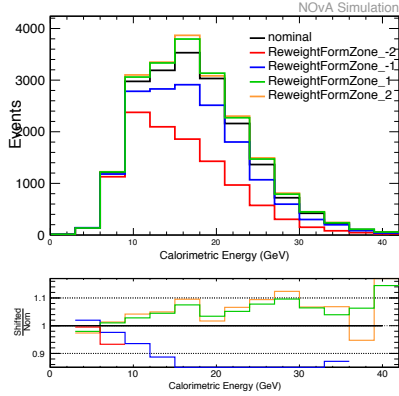
`ReweightMaCCRES` systematics for signal events passing ν_τ CC selection.
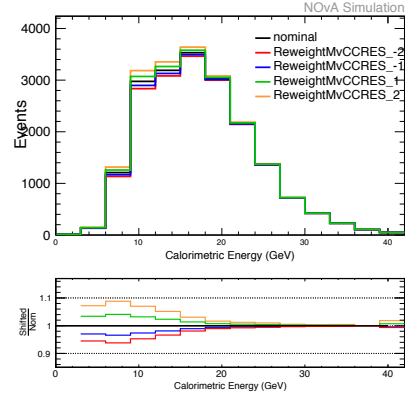
(d)

`ReweightMvCCRES` systematics for signal events passing ν_τ CC selection.

Figure 6.3: Large GENIE systematics for the events passing ν_τ selection. Continued in the Figure 6.4.
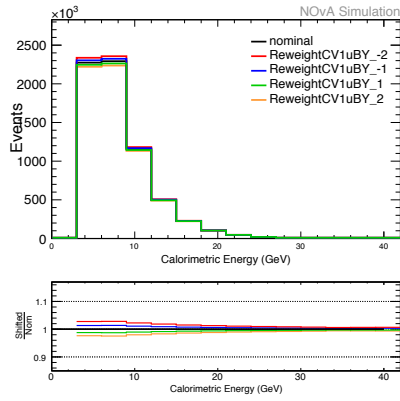
(a)

`ReweightCv1uBY` systematics for signal events passing ν_μ CC selection.
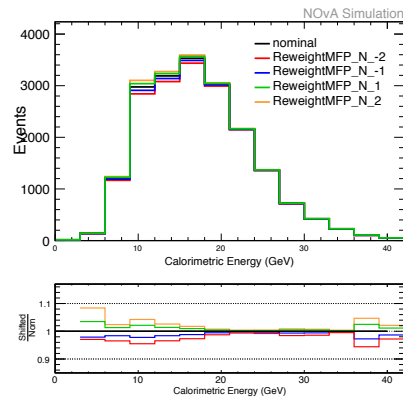
(b)

`ReweightMFP_N` systematics for signal events passing ν_τ CC selection.

Figure 6.4: Large GENIE systematics for the events passing ν_τ selection.

(a)
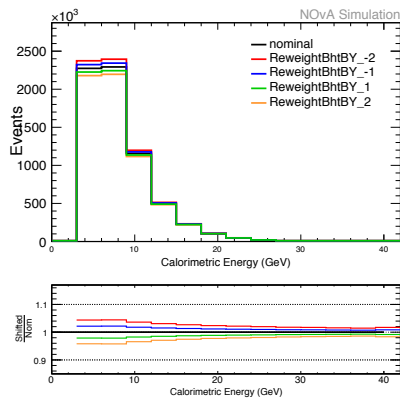
`ReweightBhtBY` systematics for signal events passing ν_μ CC selection.
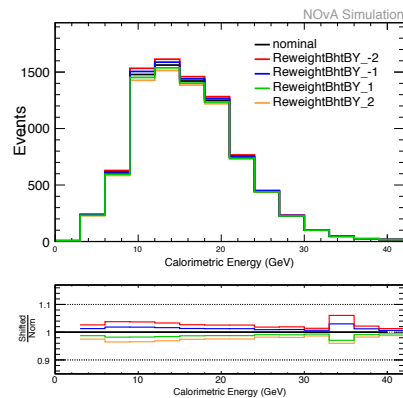
(b)

`ReweightBhtBY` systematics for background events passing ν_μ CC selection.

Figure 6.5: Large GENIE systematics for the events passing ν_μ selections. Continued in the Figure 6.6.
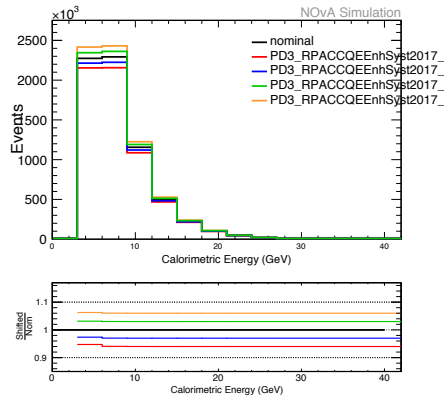
(a)

`PD3_RPACCQEEnhSyst2017` systematics for signal events passing ν_μ CC selection.

(c)
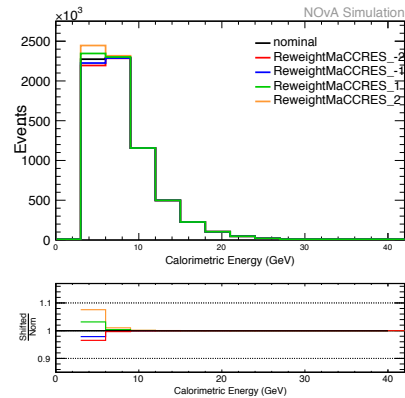
`ReweightMACCRES` systematics for signal events passing ν_μ CC selection.
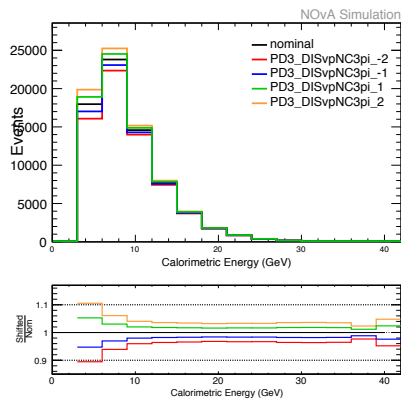
(b)

`PD3_DISvpNC3pi` systematics for background events passing ν_μ CC selection.
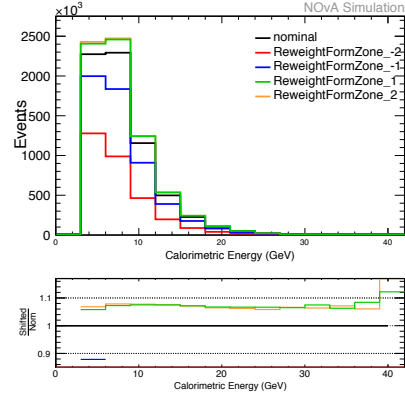
(d)

`ReweightFormZone` systematics for signal events passing ν_μ CC selection.

Figure 6.6: Large GENIE systematics for the events passing ν_μ selections. Continued in the Figure 6.7.
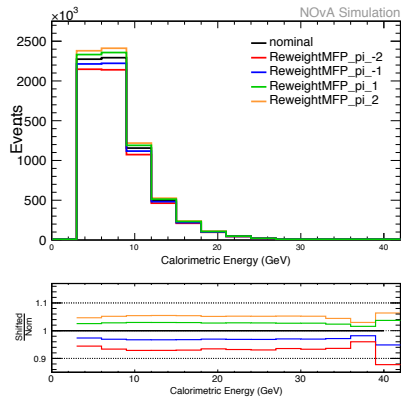
(a)

`ReweightMFP_pi` systematics for signal events passing ν_μ CC selection.
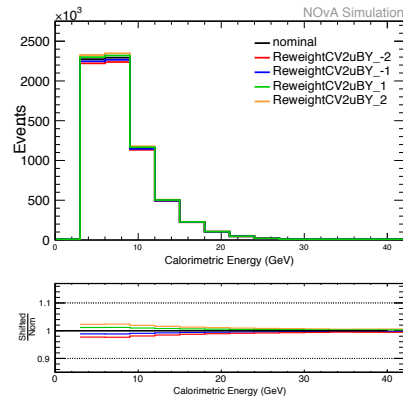
(c)

`ReweightCv2uBY` systematics for signal events passing ν_μ CC selection.
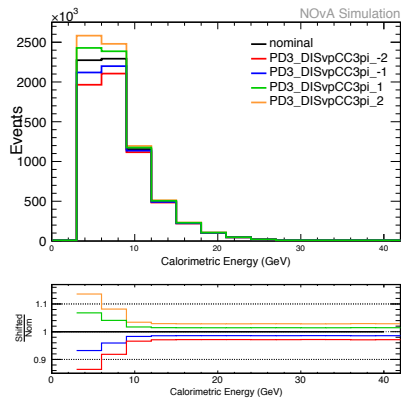
(b)

`PD3_DISvpCC3pi` systematics for signal events passing ν_μ CC selection.
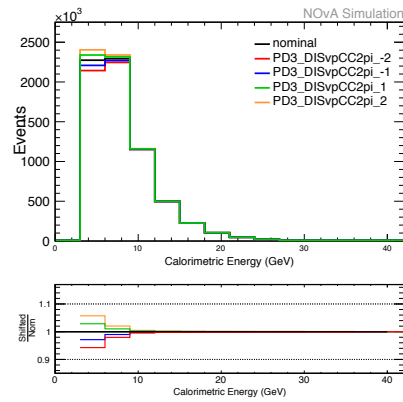
(d)

`PD3_DISvpCC2pi` systematics for signal events passing ν_μ CC selection.

Figure 6.7: Large GENIE systematics for the events passing ν_μ selections. Continued in the Figure 6.8.
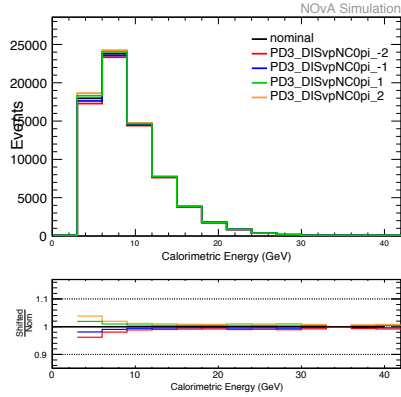
(a)

`PD3_DISvpNC0pi` systematics for background events passing ν_μ CC selection.
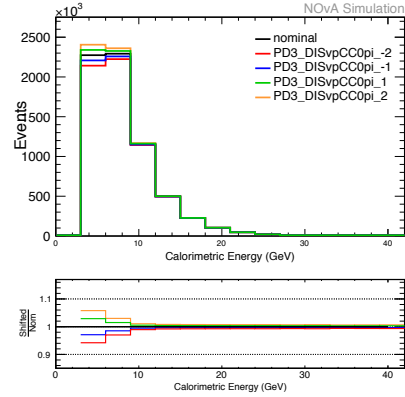
(c)

`PD3_DISvpCC0pi` systematics for signal events passing ν_μ CC selection.
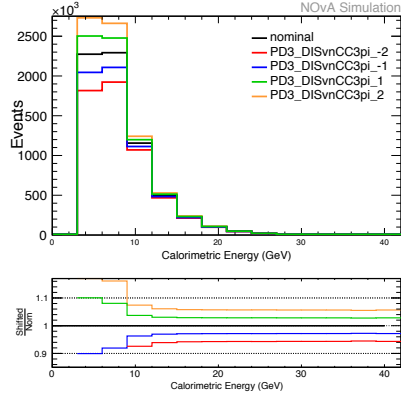
(b)

`PD3_DISvnCC3pi` systematics for signal events passing ν_μ CC selection.
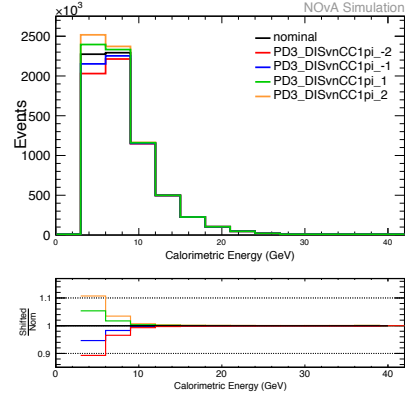
(d)

`PD3_DISvnCC1pi` systematics for signal events passing ν_μ CC selection.

Figure 6.8: Large GENIE systematics for the events passing ν_μ selections. Continued in the Figure 6.9.
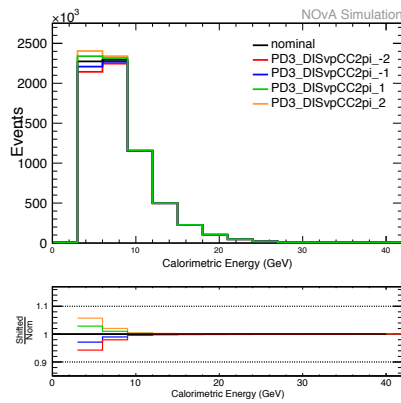
(a)

`PD3_DISvpCC2pi` systematics
for signal events passing ν_μ CC
selection.

(b)
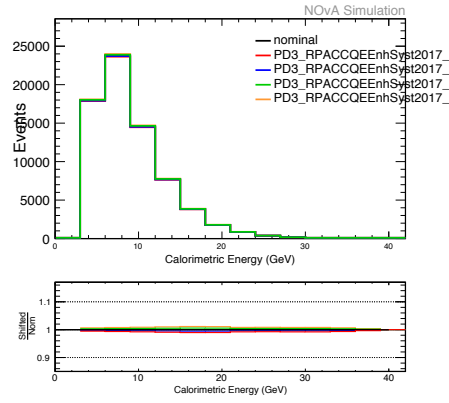
`PD3_RPACCQEEnhSyst2017`
systematics for background
events passing ν_μ CC selection.
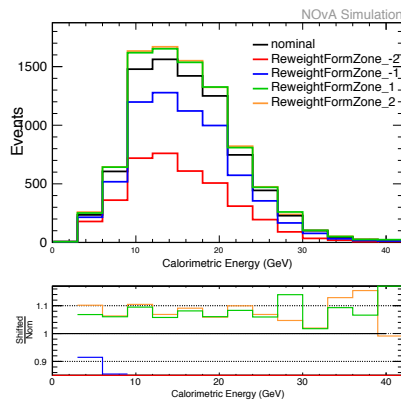
(c)

`ReweightFormZone` systematics
for background events passing
ν_μ CC selection.

Figure 6.9: Large GENIE systematics for the events passing ν_μ selections.

quadrature for signal and background for each sample. The beam transport systematic uncertainties calculated for the signal and background events that pass the ν_μ and ν_τ selections are shown in Tables 6.3 and 6.4. The corresponding plots are shown in Figure 6.10. The details of each beam transport systematic uncertainty are included in the Appendix A (see Figures A.1-A.10).

The selected neutrino events are due to the interaction of neutrinos originating from kaons and thus the flux uncertainties are very large. The total beam transport systematics (added in quadrature) is calculated to be 7.412% for the ν_τ signal and 8.224% for the background in $\nu_\mu \to \nu_\tau$ selection. For the $\nu_\mu \to \nu_\mu$ selection, the uncertainty on the signal is 4.397% and background is 4.704%.

	(%) +2σ		(%) +1σ		(%) -1σ		(%) -2σ	
	ν_τ Sig.	Bkg.	ν_τ Sig.	Bkg.	ν_τ Sig.	Bkg.	ν_τ Sig.	Bkg.
Magnetic Field in Decay Pipe	0.462	1.623	0.231	0.811	0.6625	0.704	1.325	1.408
Horn 1 X Position	5.735	7.273	2.868	3.637	5.127	4.429	10.25	8.858
Horn 1 Y Position	0.804	2.877	0.4021	1.439	2.540	2.010	5.080	4.020
Horn 2 X Position	1.038	2.487	0.518	1.243	2.077	1.991	4.154	3.982
Horn 2 Y Position	0.617	2.123	0.308	1.061	0.726	1.083	1.451	2.166
Horn Current	1.015	3.532	0.507	1.766	1.072	1.289	2.143	2.579
Spot Size	0.855	2.372	0.427	1.186	1.541	1.749	3.082	3.498
Beam Position X	0.369	0.788	0.184	0.394	0.652	0.698	1.304	1.397
Beam Position Y	0.037	0.524	0.019	0.262	0.325	0.320	0.651	0.642
New Horn Geometry and 1mm water	3.979	3.521	1.990	1.76	2.625	3.003	5.249	6.005
Target Z position	0.496	1.191	0.248	0.595	0.797	1.274	1.596	2.547
Combined Beam Transport Systematics	8.872	12.740	4.436	6.369	**7.412**	**8.224**	14.820	16.450

Table 6.3: The percentage difference between the shifted and nominal predictions for the number of selected $\nu_\mu \to \nu_\tau$ ND events due to beam systematics. The selected neutrinos are originating from kaon decays and thus have a large beam transport uncertainty.

	(%) +2σ		(%) +1σ		(%) -1σ		(%) -2σ	
	ν_μ **Sig.**	**Bkg.**	ν_μ **Sig.**	**Bkg.**	ν_μ **Sig.**	**Bkg.**	ν_μ **Sig.**	**Bkg.**
Magnetic Field in Decay Pipe	0.389	0.529	0.264	0.194	0.324	0.271	0.648	0.542
Horn 1 X Position	5.294	4.999	2.499	2.64	2.357	2.259	4.714	4.518
Horn 1 Y Position	1.594	1.687	0.843	0.796	1.107	1.079	2.215	2.159
Horn 2 X Position	1.013	1.096	0.548	0.506	1.07	0.957	2.139	1.915
Horn 2 Y Position	0.6438	0.8317	0.415	0.321	0.448	0.353	0.897	0.707
Horn Current	1.115	1.438	0.718	0.557	0.774	0.692	1.549	1.385
Spot Size	0.8882	0.9815	0.490	0.444	1.230	1.208	2.460	2.416
Beam Position X	0.346	0.376	0.188	0.173	0.504	0.495	1.010	0.991
Beam Position Y	0.063	0.091	0.045	0.032	0.247	0.233	0.493	0.466
Combined Beam Transport Systematics	5.148	4.442	2.221	2.574	2.354	2.213	4.709	4.427
Target Z position	0.553	0.675	0.337	0.276	0.502	0.405	1.005	0.808
Combined Beam Transport Systematics	8.794	8.633	4.317	**4.397**	**4.704**	4.394	9.407	8.788

Table 6.4: The percentage difference between the shifted and nominal predictions for the number of selected $\nu_\mu \to \nu_\mu$ ND events due to beam systematics. The selected neutrinos are originating from kaon decays and thus have a large beam transport uncertainty.

6.3.2   PPFX Systematics

This analysis used a new central value for the NuMI flux, derived from a combination of GEAT4 simulation [94] and PPFX (Package to Predict the FluX) weights [92]. This package combines external data from multiple sources to constrain and quantify the uncertainties on hadron production from the NuMI target. A set of weights is provided that are applied to the GEANT4 simulation of the NuMI beam (`kPPFXFluxCVWgt`) [91]. PPFX uncertainty is assessed by generating a number of alternative weightings where the uncertainty on the fixed target data and any theoretical assumptions are allowed to float within their uncertainty. Table 6.5 shows $\pm 1\sigma$ (%) difference between the nominal and shifted predictions for the ν_μ (ν_τ) signal and background of the ν_μ (ν_τ) selections.

	+1 σ (%)	-1 σ (%)
ν_μ Signal	8.384	8.384
ν_μ Background	8.503	8.503
ν_τ Signal	11.080	11.080
ν_τ Background	10.360	10.360

Table 6.5: The percentage difference between the shifted and nominal predictions for the number of selected $\nu_\mu \rightarrow \nu_\mu$ and $\nu_\mu \rightarrow \nu_\tau$ ND events due to PPFX systematics.

An uncertainty of 11.08% on signal and 10.36% on background are calculated for ν_τ selection and 8.384% on signal and 8.503% on background for ν_μ selection. The predictions and the ratio plots are shown in Figure 6.11.

6.4   Calibration Systematics

The calibration procedure is designed to make a constant energy response across the detector. This was evaluated by studying various MC samples with an engineered miscalibration. The effects studied included a miscalibration that varied as a function of the cell length and an overall scale miscalibration. The functional miscalibration was studied separately between the X and Y views of the detector. The scale miscalibration was applied as a 5% effect both up and down at the detector. These effects are motivated by studying data/MC comparisons for various samples and were updated based on the most recent round of data. The maximum overall effect was used as the systematic error that was then added in quadrature with the systematics from above. The Table 6.6 shows
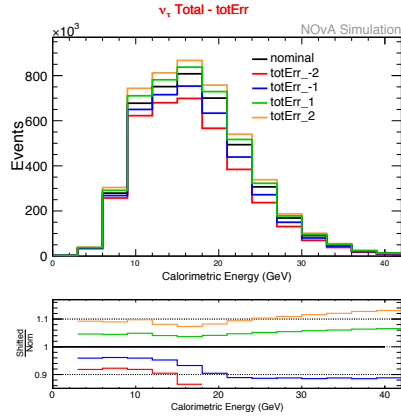
(a)

Combined beam transport systematics for signal events passing ν_τ CC selection.
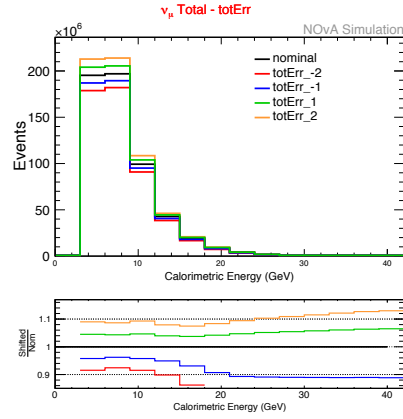
(c)

Combined beam transport systematics for signal events passing ν_μ CC selection.
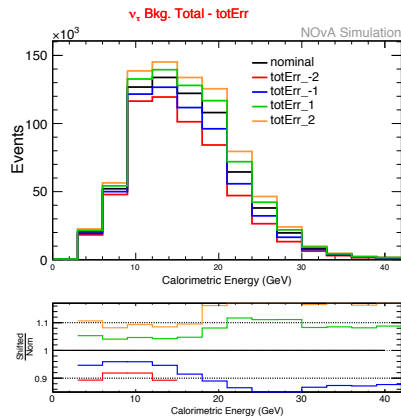
(b)

Combined beam transport systematics for background events passing ν_τ CC selection.
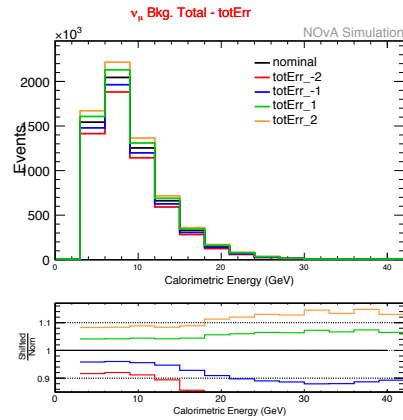
(d)

Combined beam transport systematics for background events passing ν_μ CC selection.

Figure 6.10: Combined beam transport systematics for signal and background events passing ν_τ CC and ν_μ CC selections. The selected neutrinos are originating from kaon decays.
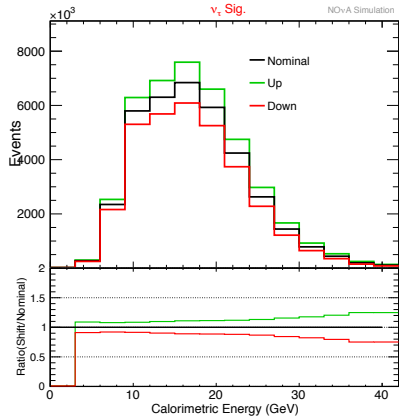
(a)

Signal events passing ν_τ CC selection.
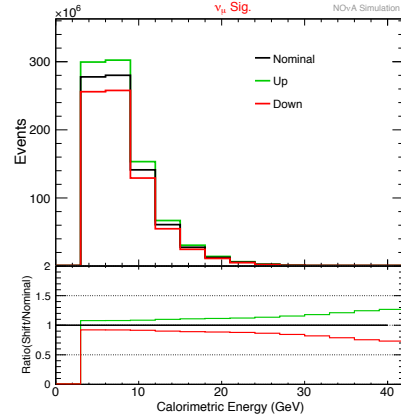
(c)

Signal events passing ν_μ CC selection.
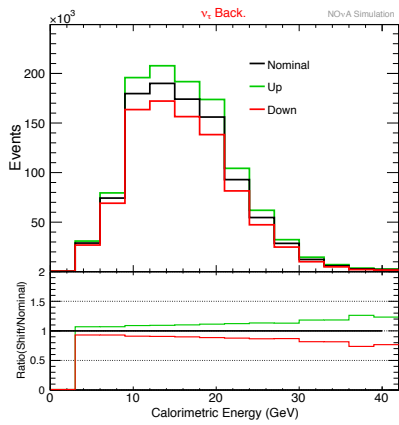
(b)

Background events passing ν_τ CC selection.

(d)
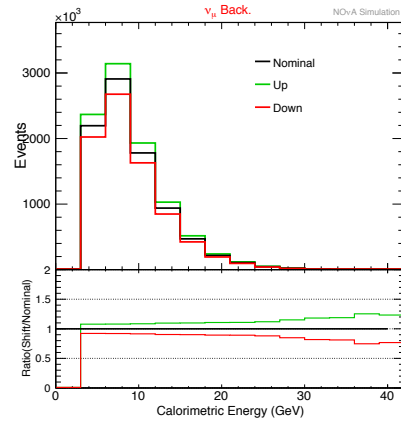
Background events passing ν_μ CC selection.

Figure 6.11: PPFX systematics for signal and background events passing ν_τ CC and ν_μ CC selections.

Systematic Parameter	ν_τ Sig.(%)	Tot. Bkg. (%)	NC (%)	ν_e (%)	ν_μ (%)
CalibUp	**14.770**	**24.990**	22.010	5.692	45.210
CalibDown	12.350	19.920	18.400	9.976	30.330
CalibShape	**7.881**	**8.077**	7.870	7.648	8.675

Table 6.6: The percentage difference between the shifted and nominal predictions for the number of selected $\nu_\mu \to \nu_\tau$ ND events due to miscalibration systematics. The bold numbers are the largest uncertainties, which will be used as the total calibration-up/calibration-down and calibration shape systematic uncertainties.

Systematic Parameter	ν_μ Sig. (%)	Tot. Bkg. (%)	NC (%)	ν_e (%)	ν_τ (%)
CalibUp	3.765	**6.122**	5.977	7.126	1.213
CalibDown	**4.284**	3.096	2.207	9.330	1.212
CalibShape	**2.063**	**0.014**	0.553	3.279	0.763

Table 6.7: The percentage difference between the shifted and nominal predictions for the number of selected $\nu_\mu \to \nu_\mu$ ND events due to miscalibration systematics. The bold numbers are the largest uncertainties, which will be used as the total calibration-up/calibration-down and calibration shape systematic uncertainties.

the calculated percentage uncertainties for signal and background of the ν_τ selection and the Table 6.7 shows the uncertainty on the signal and background of the ν_μ selection. The corresponding plots are shown in the Figures 6.12 and 6.13.

6.5 Light Level Systematics

A choice selection of images are shown in the Figures 6.14 and 6.15 which highlight the differences arising from the study of light level systematics.
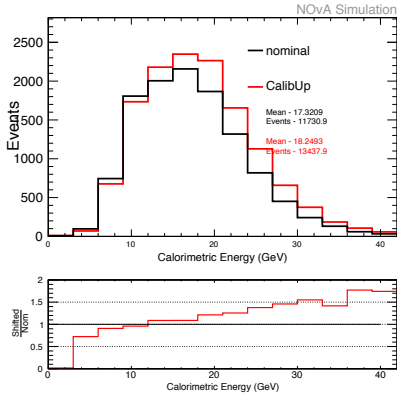
(a)

Calibration shift systematics for signal events passing ν_τ CC selection.

(c)

Calibration shift systematics for signal events passing ν_μ CC selection.
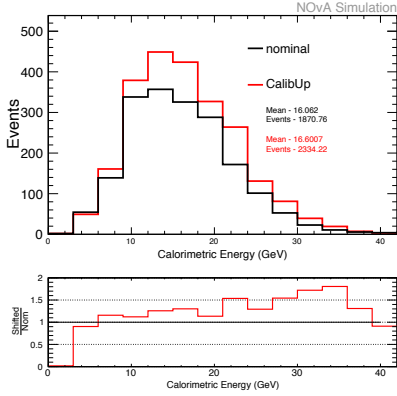
(b)

Calibration shift systematics for background events passing ν_τ CC selection.
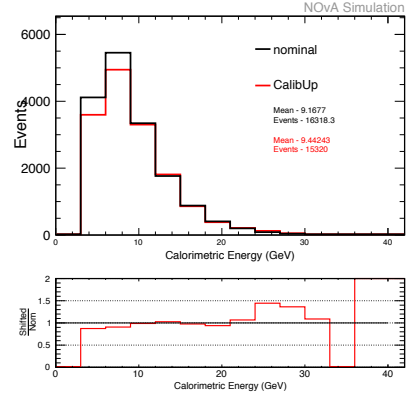
(d)

Calibration shift systematics for background events passing ν_μ CC selection.

Figure 6.12: Calibration shift systematics for the signal and background events passing ν_τ CC and ν_μ CC selections.
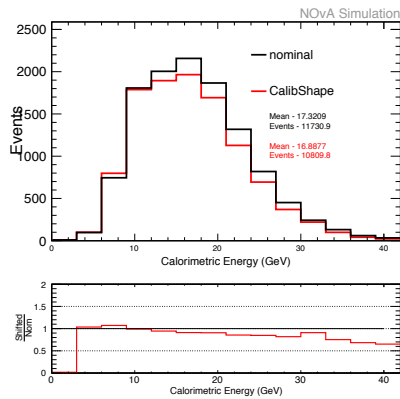
(a)

Calibration shape systematics for signal events passing ν_τ CC selection.
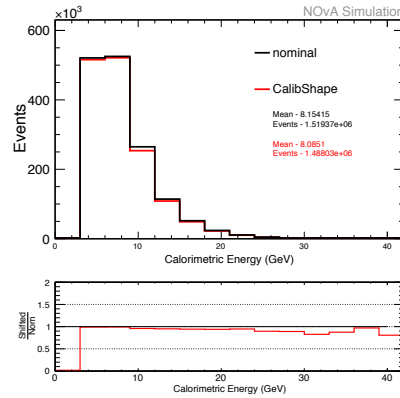
(b)

Calibration shape systematics for background events passing ν_τ CC selection.

(c)

Calibration shape systematics for signal events passing ν_μ CC selection.

(d)
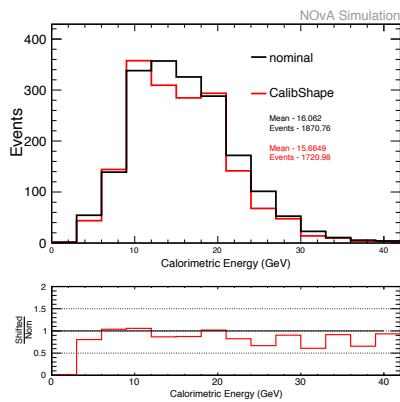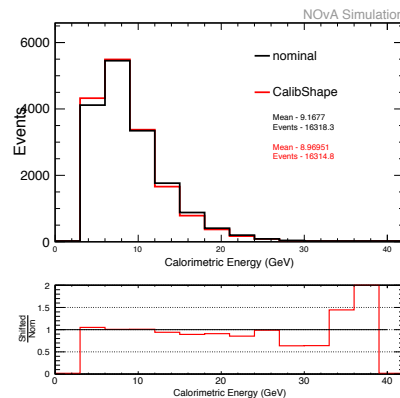
Calibration shape systematics for the signal and background events passing ν_μ CC selection.

Figure 6.13: Calibration shape systematics for the signal and background events passing ν_τ CC and ν_μ CC selections.

Systematic Parameter	ν_τ **Sig.(%)**	**Tot. Bkg.(%)**	**NC (%)**	ν_e **(%)**	ν_μ**(%)**
LightUp	0.9349	6.286	1.69	19.61	0.1568
LightDown	**4.782**	**7.069**	7.301	15.46	0.6

Table 6.8: The percentage difference between the shifted and nominal predictions for the number of selected $\nu_\mu \to \nu_\tau$ ND events due to light level systematics. The bold numbers are the largest uncertainties among light level up and down systematics, which will be used as the total light level systematic uncertainties.

Systematic Parameter	ν_μ **Sig. (%)**	**Tot. Bkg.**(%)	**NC (%)**	ν_e **(%)**	ν_τ **(%)**
LightUp	**0.9269**	1.35	0.8606	4.565	0.2482
LightDown	0.5715	**2.003**	2.552	1.701	0.05735

Table 6.9: The percentage difference between the shifted and nominal predictions for the number of selected $\nu_\mu \to \nu_\mu$ ND events due to light level systematics. The bold numbers are the largest uncertainties among light level up and down systematics, which will be used as the total light level systematic uncertainties.

For the light level systematics the reference histogram is the "No Shift Sample" for reasons discussed in Ref. [86]. Table 6.8 shows the calculated percentage uncertainties for signal and background of the ν_τ selection and Table 6.9 shows the uncertainty on the signal and background of the ν_μ selection. The corresponding distributions are shown in the Figure 6.14 and Figure 6.15 respectively.
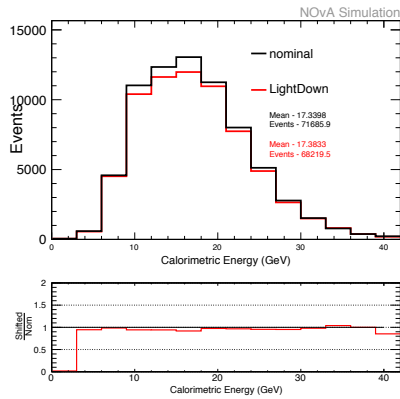
(a)

Light level down systematics for signal events passing ν_τ CC selection.
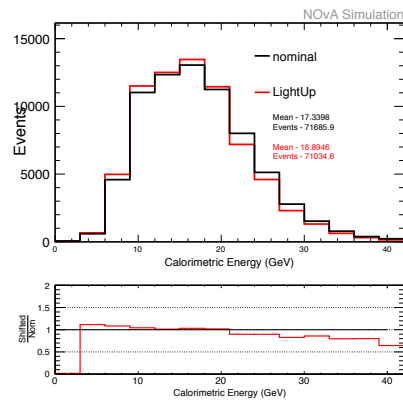
(c)

Light level up systematics for signal events passing ν_τ CC selection.

(b)

Light level down systematics for background events passing ν_τ CC selection.

(d)
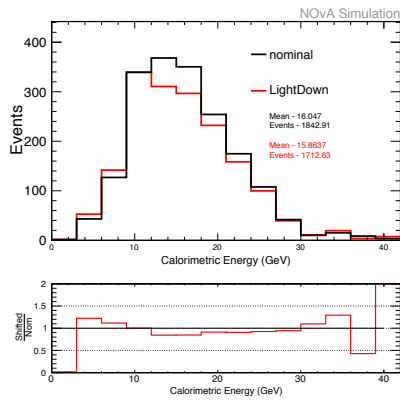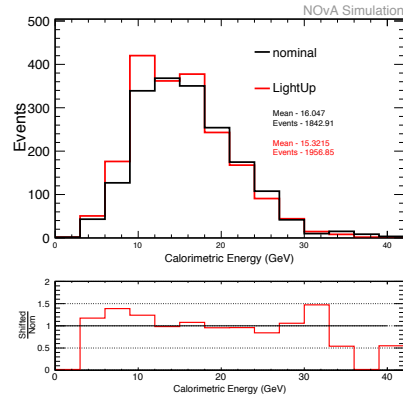
Light level up systematics for background events passing ν_τ CC selection.

Figure 6.14: Light level systematics for the signal and background events passing ν_τ selection.
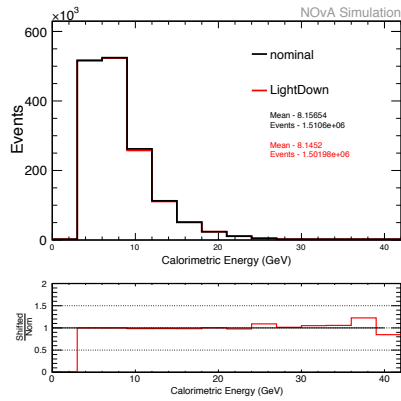
(a)

Light level down systematics for signal events passing ν_μ CC selection.
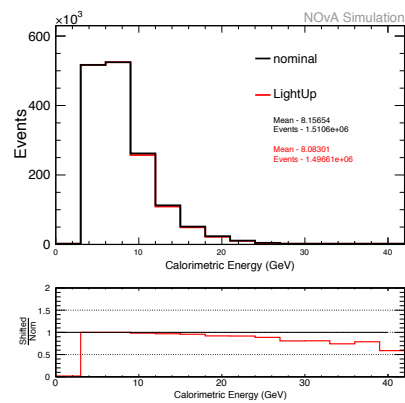
(c)

Light level up systematics for signal events passing ν_μ CC selection.

(b)

Light level down systematics for background events passing ν_μ CC selection.

(d)
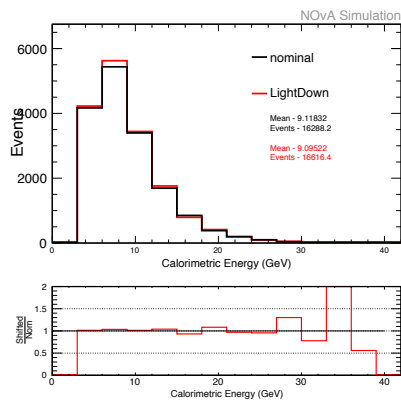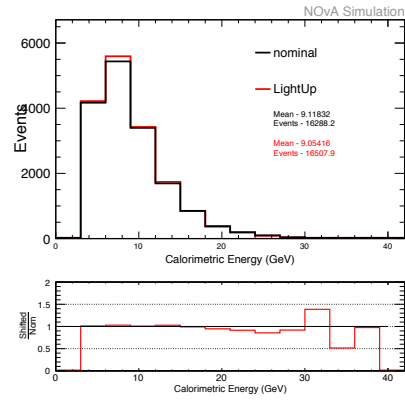
Light level up systematics for background events passing ν_μ CC selection.

Figure 6.15: Light level systematics for the signal and background events passing ν_μ selection.

Systematic Parameter	ν_τ Sig.(%)	Tot. Bkg.(%)	NC (%)	ν_e (%)	ν_μ (%)
CkvPhoton	**1.910**	**0.967**	2.353	7.171	1.074

Table 6.10: The percentage difference between the shifted and nominal predictions for the number of selected $\nu_\mu \to \nu_\tau$ ND events due to Cherenkov systematics.

Systematic Parameter	ν_μ Sig. (%)	Tot. Bkg.(%)	NC (%)	ν_e (%)	ν_τ (%)
CkvPhoton	**0.8212**	**0.706**	0.312	3.444	0.211

Table 6.11: The percentage difference between the shifted and nominal predictions for the number of selected $\nu_\mu \to \nu_\mu$ ND events due to Cherenkov systematics.

6.6   Cherenkov Systematics

An adjustment to the Cherenkov model shifts proton response down by 2.6% while leaving muon response unchanged [87]. The shifted light level and Cherenkov datasets were produced with the PhotonRewriter and is compared to a PhotonRewirter-NoShift sample instead of the nominal sample. This detail is handled by the PredictionSysts2017 classes in CAFAna. Table 6.10 shows the calculated percentage uncertainties for signal and background of the ν_τ selection and Table 6.11 shows the uncertainty on the signal and background of the ν_μ selection. The corresponding plots are also shown in the Figure 6.16.
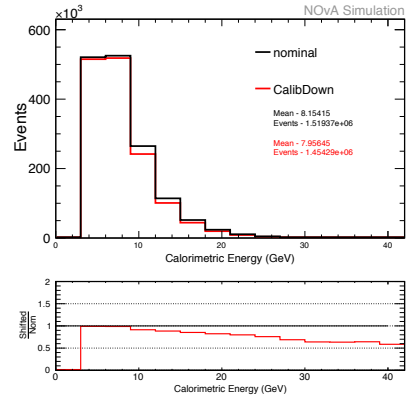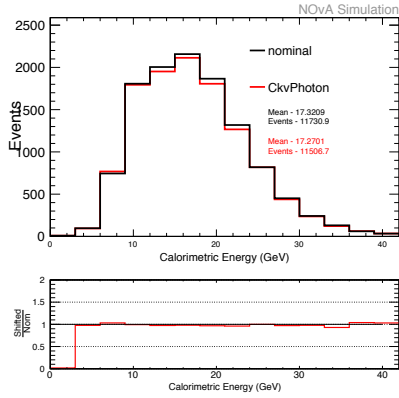
(a) Cherenkov light systematics for signal events passing ν_τ CC selection.
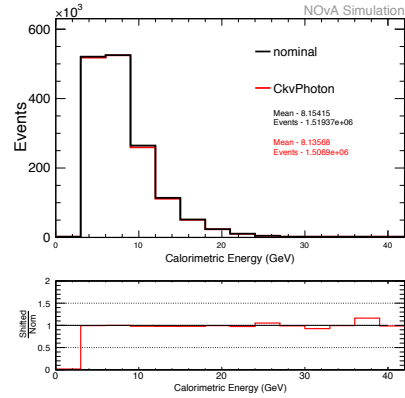
(c) Rock systematics for signal events passing ν_μ CC selection.
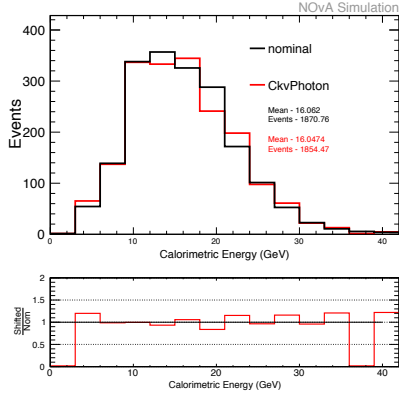
(b) Cherenkov light systematics for background events passing ν_τ CC selection.
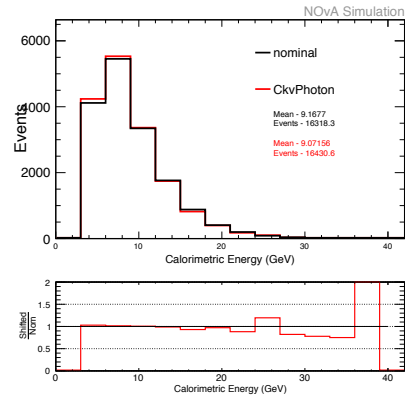
(d) Cherenkov light systematics for background events passing ν_μ CC selection.

Figure 6.16: Cherenkov light systematics for the signal and background events passing ν_τ CC and ν_μ CC selections.

Selection	Signal (%)	Background (%)
ν_τ	0.23	0.23
ν_μ	0.23	0.95

Table 6.12: The percentage difference between the shifted and nominal predictions for the number of selected $\nu_\mu \to \nu_\mu$ and $\nu_\mu \to \nu_\tau$ ND events due to rock systematics.

6.7   ND Rock Contamination Systematics

The MC simulation does include neutrino interactions that occur in the rock that surrounds the ND. These events often leak into the detector volume, and most of them are cut away by fiducial and containment cuts, but some of them remains. Those events that do remain cannot be reconstructed properly as their origins are outside of the detector. The systematic error that is incurred due to the rock event contamination was estimated by predicting the ND event spectrum with rock events removed by MC truth and comparing to the nominal predicted spectrum. The events were only removed from the ND MC sample, requiring that the true neutrino vertex was inside the detector. The shifted spectra are shown in Figure 6.17. This systematic amounted to an overall 0.23 % shift on the background spectrum of ν_τ selection. Similarly an overall 0.23% shift on the ν_μ signal spectrum and a 0.95 % shift on the background spectrum. We did not simulate the rock interactions for ν_τs and hence the same calculated 0.23% systematics for the background for this selection is assumed on the signal events also.
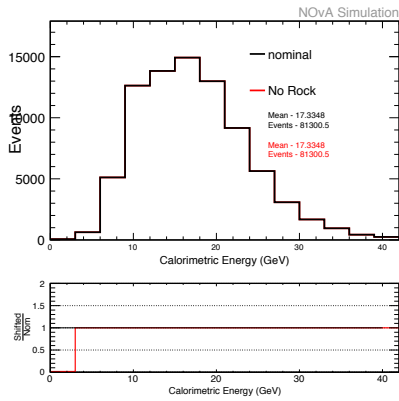
(a)

Rock systematics for signal events passing ν_τ CC selection.

(c)
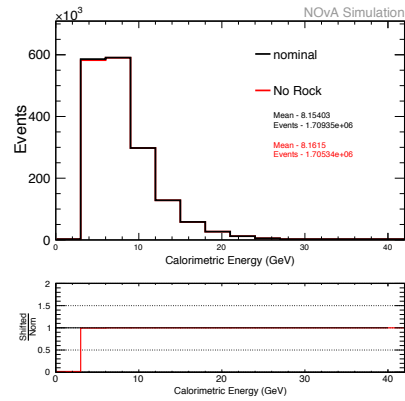
Rock systematics for signal events passing ν_μ CC selection.
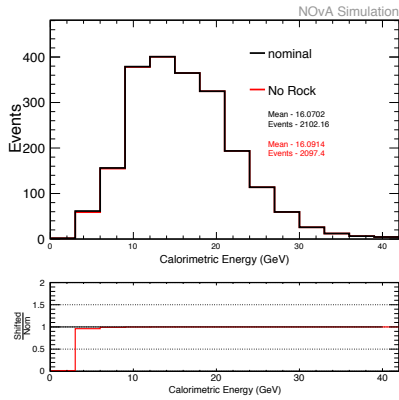
(b)

Rock systematics for background events passing ν_τ CC selection.
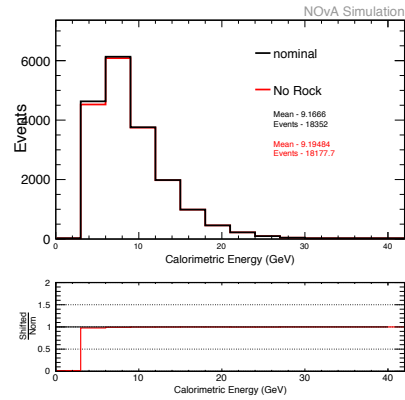
(d)

Rock systematics for background events passing ν_μ CC selection.

Figure 6.17: Rock systematics for background events passing ν_τ CC and ν_μ CC selections.

6.8   Overall Noramlization

A number of sources of uncertainty give rise to an overall normalization uncertainty on the ND event rate. The normalization systematic accounts for uncertainties in ν_τ cross section, muon energy scale, POT accounting and detector mass.

6.8.1   Muon Energy Scale

An absolute error of 0.96% and 0.76% is accounted for the ND active volume and muon catcher, respectively. The details are given in Ref. [88].

6.8.2   POT Accounting

This systematic accounts for the drift in the ratio of the calibrated response of `TRTGTD` and `TR101D` which is calculated to be a 0.5% overall normalization effect for the ND [89].

6.8.3   Detector Mass

Intensive work is done to get the correct mass accounting for both the detectors which is in Ref. [88] . From this reference, we consider a 0.27%

Systematic Parameter	ν_τ Sig.	Bkg.	ν_μ Sig.	Bkg.
cross section	50.00	20.14	20.87	21.68
Beam	7.41	8.22	4.39	4.70
PPFX	8.38	8.50	11.08	10.36
Calib +/-	14.77	24.99	4.28	6.12
Calib Shape	7.88	8.07	2.06	0.01
Light Level	4.78	7.07	0.92	2.00
Cherenkov	1.91	0.97	0.82	0.70
ND Rock	0.00	0.22	0.23	0.94
Overall Normalization	1.12	1.12	1.12	1.12
Sum in quadrature	**54.14**	**35.87**	**24.59**	**25.36**

Table 6.13: The percentage difference between the shifted and nominal predictions for the number of selected $\nu_\mu \to \nu_\mu$ and $\nu_\mu \to \nu_\tau$ ND events due to overall systematics.

overall normalization effect for the ND when considering detector mass accounting inaccuracies.

6.9 Summary

Table 6.13 shows a summary of all of the systematics, as well as an overall uncertainty. The overall uncertainty was calculated by summing the uncertainty from each row in quadrature. The final systematic uncertainty on the ν_τ and ν_μ signal are 54.14% and 24.59% respectively, and the uncertainty on the backgrounds are 35.87% and 25.36% respectively. The largest systematic uncertainty is the ν_τ cross section uncertainty (50%) in ν_τ selection since the ν_τ cross sections are not well studied yet.

Chapter 7

Sensitivity Studies

We now discuss the fitting and confidence determination for the analysis of the ν_τ appearance in NOvA ND. The ν_τ analysis is ideal for finding sterile neutrinos and making a measurement of $\sin^2 2\theta_{\mu\tau}$ and Δm^2_{41} and providing a constraint to the ν_τ appearance analysis which is sensitive to a large phase space. The final deliverables are allowed contours in $\sin^2 2\theta_{\mu\tau}$ vs. Δm^2_{41} space and $\sin^2 \theta_{24}$ vs. Δm^2_{41} space, which allows a confidence of rejecting a particular value of these parameters. Below we outline the procedure for placing appropriate limits on the phase space of the underlying neutrino properties and the effect of analysis choices in the sensitivities.

7.1   Fitting and $\Delta\chi^2$ Determination

The analysis fit, like all other analyses pieces, makes heavy use of the CAFAna framework. SBL oscillation framework in CAFAna allows users

to develop a spectral prediction of ND events for an arbitrary set of oscillation parameters. This prediction also encodes information about the variable L/E and spectral shifts caused by various systematic sources.

As such, the CAFAna prediction and fitting framework contains all the information needed to properly extract oscillation and nuisance systematic parameters. In this fit, systematic uncertainty terms are profiled and a pull term is included to keep the number of degrees of freedom in the fit a constant.

7.1.1   Correlated Systematic Uncertainties

As mentioned earlier, the analysis uses only ND data, which forces this analysis to find an alternate method to deal with large systematic uncertainties. To deal with these large uncertainties, we applied a joint ν_μ-ν_τ fit to the sterile oscillation parameters, which significantly reduced the systematics effect in this analysis. Also we assigned 100% correlation between individual components involved in each sample as mentioned in the Table 7.1 and made use of $\nu_\mu \rightarrow \nu_\mu$ sample to constrain the systematics in ν_τ appearance sample. The list of systematics and the correlations assigned are given in the Table 7.1.

Systematic Parameter	Correlation
Cross Section	Correlated for ν_μ CC, NC, ν_e CC and ν_τ CC seperately
Beam	Yes
PPFX	Yes
Calib +/-	Yes
Calib Shape	Yes
Light Level	Yes
Cherenkov	Yes
ND Rock	Yes
Overall Normalization	Yes

Table 7.1: The correlations between systematic uncertainities for the selected $\nu_\mu \to \nu_\mu$ and $\nu_\mu \to \nu_\tau$ ND events.

7.2 Joint Vs. Single Fit

The sensitivity studies using a single ν_τ selection and a joint ν_μ-ν_τ fit are discussed below. The Figure 7.1 shows the comparison between these two fits and a comparison of these fits with the previous experiment results. The red line is the joint statistics only sensitivity, dotted red line is after including a flat 10% normalization systematic uncertainty, the solid blue line represents the statistics only sensitivity for ν_τ only selection and dotted blue line is the ν_τ only sensitivity after including a 10% normalization systematic uncertainty, all for 90% C.L. The joint fit improves the overall sensitivity even after including a 10% normalization systematic uncertainty. The black line shows the NOMAD result and dark blue line is the CHORUS result for 90% C.L., also we should note

that all these previous experiments used only a two-flavor approximated oscillations and have not used a 3+1 sterile neutrino oscillation model. In this analysis, we have applied 3+1 oscillation weights to all prominent appearing and disappearing neutrino oscillation channels to explore the sterile neutrino oscillation parameters.
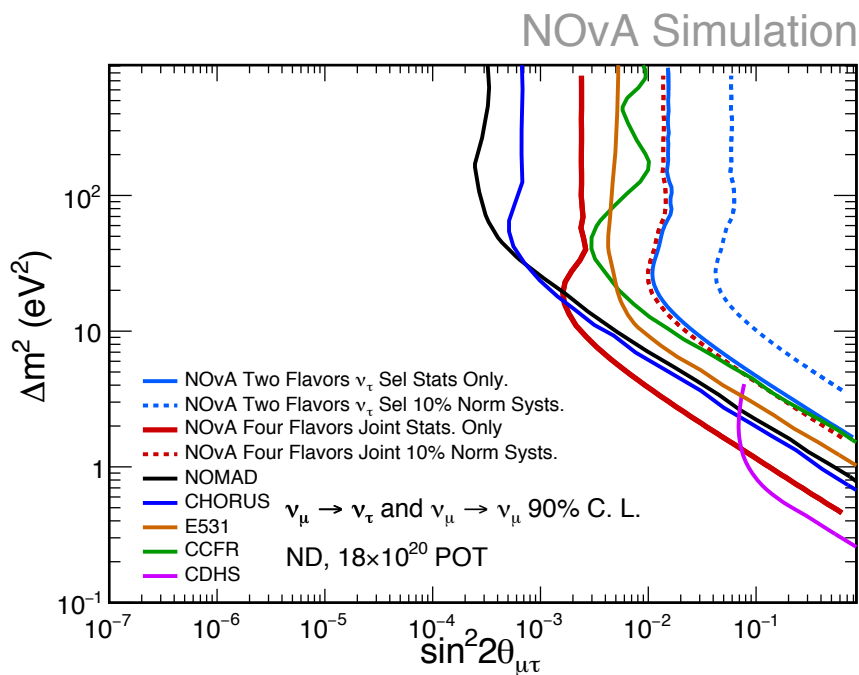
Figure 7.1: The comparison between sensitivities for just ν_τ fit and a joint ν_μ and ν_τ fit. Also compared to the results from other experiments. The red line is the joint stats. only sensitivity, dotted red line is after including a flat 10% normalization systematics, the solid blue line represents the statistics only sensitivity for ν_τ only selection and dotted blue line is the ν_τ only sensitives after including a 10% normalization systs., all within 90% C.L.

7.2.1 The Joint Fit

The Figure 7.2 shows the joint sensitivity plot for Δm_{41}^2 vs. $\sin^2 2\theta_{\mu\tau}$ scaled to a data POT of 8.06×10^{20}. The plots are made marginalizing over $\sin^2 2\theta_{24}$ and $\sin^2 \theta_{34}$. All other three flavor parameters set to the standard oscillation values, but they would not change oscillation probabilities. We set CP-mixing phases (δ's) $= 0$ as they have no effect at ND. Setting the angle $\theta_{14} = 0$ or allowing the fitter to marginalize over θ_{14} gives the same result as $\sin^2 2\theta_{\mu\tau}$ depends on $\cos^4 \theta_{14}$. The right region to violet line in the figure is the NOvA statistics only excluded region. The region right to the red line is the NOvA sensitivity after including all the systematics within 90% C.L. The Figure 7.3 shows the joint sensitivity plot for Δm_{41}^2 vs. $\sin^2 \theta_{24}$ scaled to a data POT of 8.06×10^{20}. The plots are made marginalizing over $\sin^2 \theta_{34}$. All other three flavor parameters set to the standard oscillation values. If the anomalous results from previous experiments [70, 71] were due to the existence of fourth flavor neutrino with a larger mass than the standard 3-flavor neutrinos, the NOvA near detector is expected to see the modifications in the NuMI flux due to the mixing between active and sterile neutrinos. We expect to see ν_τ CC interactions in ND due to these oscillations. This analysis is found to be sensitive to probe SBL sterile neutrino oscillations with $\sin^2 2\theta_{\mu\tau}$ and $\sin^2 \theta_{24} \gtrsim 0.1$ at $\Delta m_{41}^2 > 10$ eV^2.
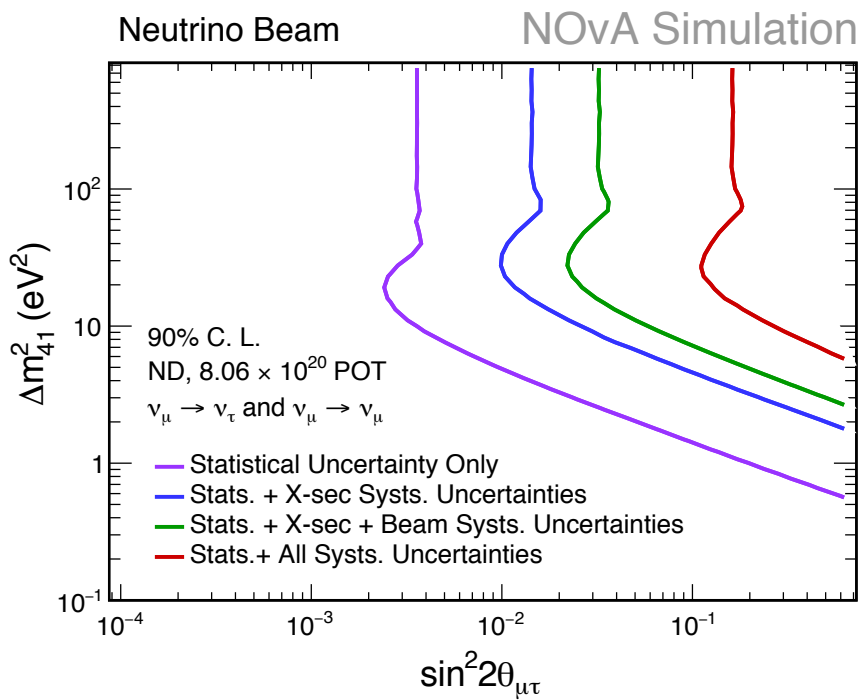
Figure 7.2: The sensitivity plot for Δm^2_{41} vs. $\sin^2 2\theta_{\mu_\tau}$. The right region to the violet line is the NOvA stats. only excluded region. The region right to the red line is the NOvA sensitivity within 90% C.L. after including all the systematics.
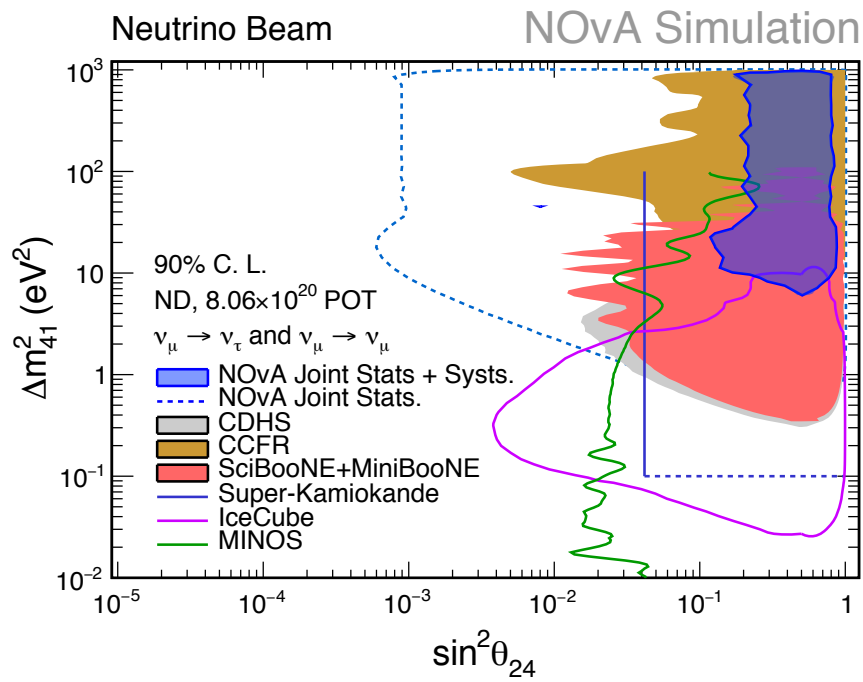
Figure 7.3: The sensitivity plot for Δm^2_{41} vs. $\sin^2 \theta_{24}$. The sensitivities are compared to the results from other experiments. The light shaded blue region is the NOvA stats. only excluded region and dark blue region is the NOvA sensitivity within 90% C.L. after including all the systematics.

7.3   Studies Using Real Data

We used the real data in two separate regions, where we do not expect any significant ν_τ appearance and ν_μ disappearance (sideband region) for the ν_τ and ν_μ selection respectively, to study any discrepancy in data and MC in high energy regions. All sideband studies show a good agreement between the data and MC within the systematic uncertainties. This analysis is performed as a rate-only analysis.

7.3.1   A mid ν_μ CVN region for ν_μ selection

We applied all the preselection cuts for ν_μ sample except the cut on ν_μ CVN (ν_μ CVN cut in the actual ν_μ selection is shown in the Figure 5.6b) and added a sideband cut such that $0.35 < \nu_\mu$ CVN < 0.5 for this study. The details of the cuts are given in the Table 7.2 and the number of events pass this selection are given in the Table 7.3. The number of events pass in data and MC are 138905 ± 373 (stats.) and 136985 ± 34712 (systs.) respectively. The corresponding calorimetric energy distribution of the selected events are shown in the Figure 7.4. The points denotes the data and blue, green and violet histograms respectively are the stacked prediction of NC, ν_μ CC and ν_e CC components. The red region in the ratio plot shows the systematic uncertainty band, which covers the mismatch between the data and MC.

Cut Level	Variable	Cut Value
Data Quality	kStandardSpillCuts	Standrad NuMI Spill Cuts
Preselection	+kNDContainment +kNDFiducial	Details are given in Table 5.1
	+kCalE	4.2 GeV < kCaloE
Sideband Cut	+kNumuCVN	0.35 < kCVNm < 0.5

Table 7.2: The selection cuts used for ν_μ sideband selection.
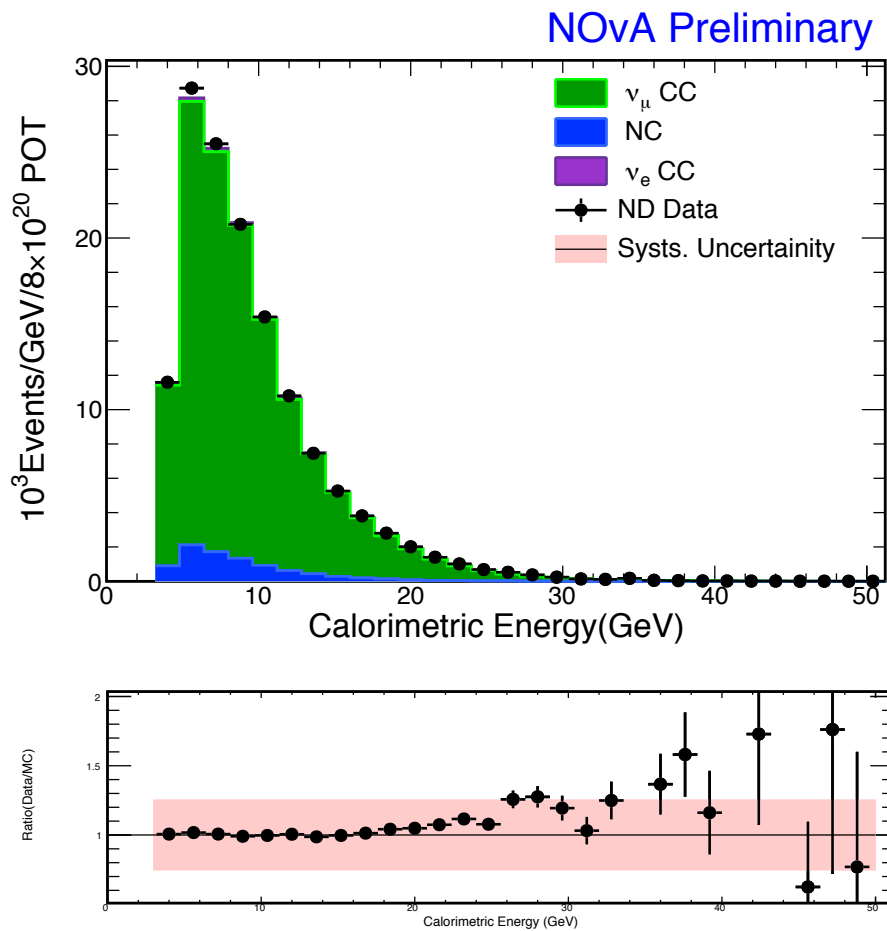
Figure 7.4: The events passing the ν_μ sideband selection with the cuts defined in Table 7.2, assuming 3 flavor oscillations.

ν_μ CC	126952
NC	8914
ν_e CC	1119
Total MC Prediction	136985 ± 34712 (systs.)
Real Data	138905 ± 373 (stats.)

Table 7.3: The summary of the events passing ν_μ side-band selection including the stats. and systs. uncertainties. MC scaled to a data POT of 8.06×10^{20}.

7.3.2   A high NC CVN region for ν_τ selection

Except the cut on NC CVN, we have applied all the preselection cuts for ν_τ sample and then added the sideband cut such that NC CVN > 0.62 for this sideband study. The cuts applied are given in the Table 7.4 and the number of events pass in data and MC are given in the Table 7.5. The number of events pass this selection cuts for data and MC are 189962 ± 436 (stats.) and 193528 ± 67735 (systs.) respectively. The corresponding calorimetric energy distribution of the selected events are shown in Figure 7.5. The points denote the ND data and blue, green and violet histograms respectively are the stacked predictions of the NC, ν_μ CC and ν_e CC components. The red region in the ratio plot shows the systematic uncertainty band, which covers the mismatch between the data and MC.

Cut Level	Cut	Details
Data Quality	kStandardSpillCuts	Standrad NuMI Spill Cuts
Event Quality	+(kNTrks > 0)	Number of tracks
	+(kNShw > 0)	Number of showers
	+kNDFiducial	
	+kNDContain	Details are given in Table 5.1
BDTG Presel	+(4.2 < kCaloE)	Calorimetric Energy (GeV)
	+(kCVNm < 0.1)	CVN numu classifier
Sideband Cut	+(kCVNnc > 0.62)	CVN nc classifier

Table 7.4: The selection cuts used in ν_τ sideband selection.

ν_μ CC	26247
NC	164022
ν_e CC	3259
Total MC Prediction	193528 ± 67735 (systs.)
Real Data	189962 ± 436 (stats.)

Table 7.5: The events passing ν_τ side-band selection including the stats. and systs. uncertainties. MC scaled to the data POT of 8.06×10^{20}.
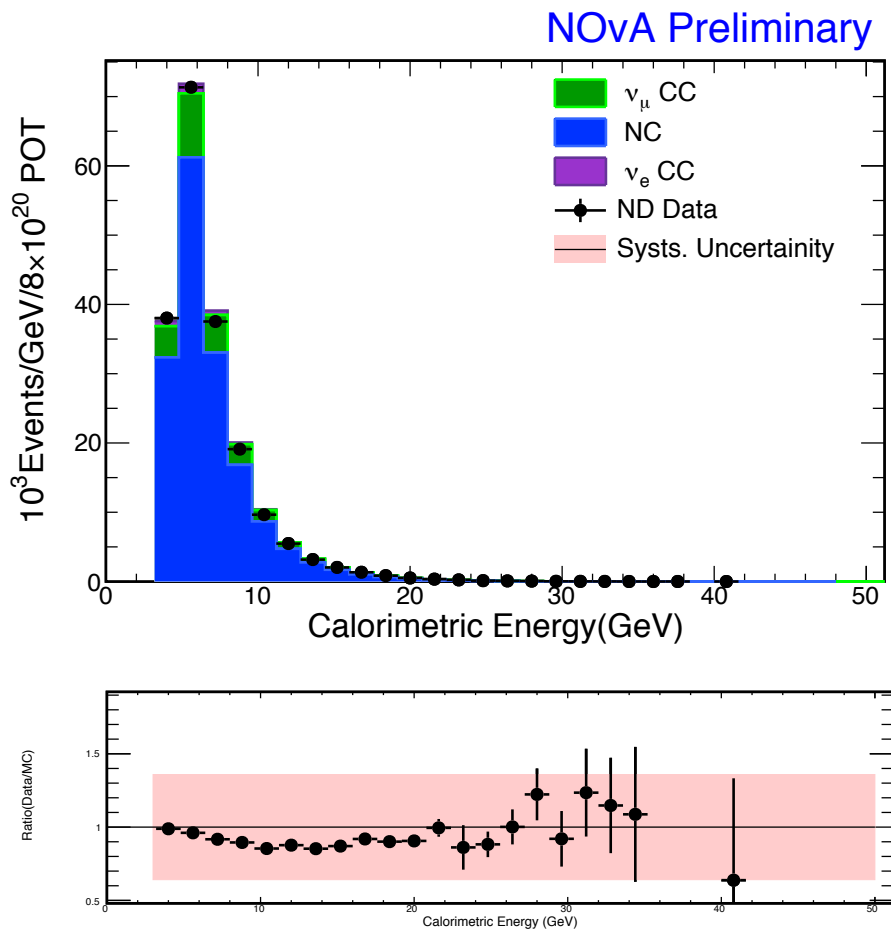
Figure 7.5: The events passing ν_τ side-band selection with the cuts defined in the Table 7.4 assuming 3 flavor oscillation.

Chapter 8

Conclusions and Future Plan

8.1   Results and Conclusions

The NOvA experiment is primarily designed for exploring the parameters involved in the active three flavor neutrino oscillations. Detectors are designed to observe the charged current muon-neutrino and electron-neutrino interactions, and the detectors are also capable of identifying the neutral current interactions. However, if the anomalous results from previous experiments were due to the existence of fourth flavor neutrino with a larger mass than the standard 3-flavor neutrinos, the NOvA Near Detector is expected to see the modifications in the NuMI flux due to this active to sterile neutrino oscillations.

In this thesis, we have shown the capability of the NOvA Near Detector to select ν_τ CC interactions with high purity using a noval method which is discussed in Chapter 5. For this, we have developed the particle

discriminants to select the hadronic ν_τ CC interactions from NC and ν_μ, ν_e CC backgrounds in NOvA ND as described in Chapter 4.

Finally, we have shown the NOvA experiment's potential to probe the anomalous muon-neutrino disappearance and tau-neutrino appearance using the NOvA Near Detector. The NOvA experiment is found to be sensitive to probe such SBL sterile neutrino oscillations with $\sin^2 2\theta_{\mu\tau}$ and $\sin^2 \theta_{24} \gtrsim 0.1$ at $\Delta m_{41}^2 > 10$ eV^2.

In NOvA long-baseline oscillation searches, the data from ND is used to constrain the correlated systematic uncertainties such as the detector and flux related uncertainties. But this analysis uses only ND which makes the analysis extremely hard as there is no such cancellation of systematic uncertainties. But we used an alternate method to constrain the large systematic uncertainties in this analysis. A high energy $\nu_\mu \rightarrow \nu_\mu$ disappearance sample is used to constrain the correlated systematic uncertainties incorporated with the $\nu_\mu \rightarrow \nu_\tau$ appearance sample. A brief demonstration about how the systematic uncertainties get constrained when we use a joint $\nu_\mu - \nu_\tau$ fit is given in Section 7.2. This is the first analysis of this kind and is a 'new method proving' analysis in NOvA.

The studies conducted so far are well understood, but some cross checks are needed before we can look at the data and produce the final NOvA's results from this analysis. This thesis contains all the results except the final data results. We have compared the real data

with MC in sideband regions and found that the systematic uncertainties cover the mismatch between the data and MC. We plan to use the ND data collected between October 2014 and May 2017 which corresponds to 8.05×10^{20} POT to publish the first results of this analysis.

8.2 Future Plan

We have enough room to improve the sensitivity by constraining the hadron production uncertainties, by improving the cross section models and with the use of ND specific energy estimators. By improving the ν_τ signal purity and with increased statistics we can improve the sensitivity to the sterile neutrino oscillation parameters. The same study can be done for NOvA's anti-neutrino data and can be used to make a joint fit with the NC-sterile results from NOvA to constrain $\sin^2 \theta_{24}$.

Appendix A

Details of Systematics

A.1 Data Sets

The data sets used for the evaluation of systematics are listed below.
These all MC files are prod-3 versions.

A.1.1 Nominal Samples

The data sets we used for the nominal MC files are prod3 version named
as shown below:

- `prod_caf_R17-03-01-prod3reco.k_nd_genie_nonswap_fhc`
  `_nova_v08_full_cycle0_v1_nutaucc-overlay`

- `prod_caf_R17-03-01-prod3reco.d_nd_genie_nonswap_fhc`
  `_nova_v08_full_v1`

A.1.2   Miscalibration Samples

Here we used the MC files defined as a data set:

- `prod_caf_R17-03-01-prod3reco.h_nd_genie_nonswap_fhc`
  `_nova_v08_full_calib-shift-nd-xyview-pos-offset_v1`

- `prod_caf_R17-03-01-prod3reco.k_nd_genie_nonswap`
  `_fhc_nova_v08_full_calib-shift-nd-xyview-pos-offset`
  `_nutaucc-overlay_v1`

- `prod_caf_R17-03-01-prod3reco.h_nd_genie_nonswap_fhc`
  `_nova_v08_full_calib-shift-nd-xyview-neg-offset_v1`

- `prod_caf_R17-03-01-prod3reco.k_nd_genie_nonswap`
  `_fhc_nova_v08_full_calib-shift-nd-xyview-neg-offset`
  `_nutaucc-overlay_v1`

- `prod_caf_R17-03-01-prod3reco.j_nd_genie_nonswap_fhc`
  `_nova_v08_full_calib-shift-nd-func_v1`

- `prod_caf_R17-03-01-prod3reco.k_nd_genie_nonswap_fhc`
  `_nova_v08_full_calib-shift-nd-func`
  `_nutaucc-overlay_v1`

A.1.3 Light Level Samples

For this light level systematics, we replace "Nominal" sample by "No shift" sample for all light level systematics due to reasons mentioned in [86].

- `prod_caf_R17-03-01-prod3reco.l_nd_genie_nonswap_fhc _nova_v08_full_lightmodel-noshift_nutaucc-overlay_v1`

- `prod_caf_R17-03-01-prod3reco.l_nd_genie_nonswap_fhc _nova_v08_full_no-shift_v1`

- `prod_caf_R17-03-01-prod3reco.l_nd_genie_nonswap_fhc _nova_v08_full_lightmodel-lightup-calibdown_v1`

- `prod_caf_R17-03-01-prod3reco.l_nd_genie_nonswap_fhc_nova _v08_full_lightmodel-lightup-calibdown_nutaucc-overlay_v1`

- `prod_caf_R17-03-01-prod3reco.l_nd_genie_nonswap_fhc _nova_v08_full_lightmodel-lightdown-calibup_v1`

- `prod_caf_R17-03-01-prod3reco.l_nd_genie_nonswap_fhc _nova_v08_full_lightmodel-lightdown-calibup_nutaucc-overlay_v1`

A.1.4 Cherenkov Samples

The data sets used for Cherenkov systematics calculations are given below:

- `prod_caf_R17-03-01-prod3reco.l_nd_genie_nonswap_fhc`
  `_nova_v08_full_ckv-proton-shift-down_v1`

- `prod_caf_R17-03-01-prod3reco.l_nd_genie_nonswap_fhc`
  `_nova_v08_full_ckv-proton-shift-down_nutaucc-overlay_v1`

A.2 GENIE Systematics

This appendix contains the details of the GENIE and beam transport shifts for both the $\nu_\mu \to \nu_\mu$ and $\nu_\mu \to \nu_\tau$ selections. These shifts are calculated by tweaking the GENIE and beam parameters $\pm 1\sigma$ and $\pm 2\sigma$ levels in the Nominal MC samples. The GENIE parameters used for the $\nu_\mu - \nu_\tau$ joint analysis in NOvA ND are detailed here. The Table A.1 and A.2 details the systematic uncertainties in the GENIE parameters we considered in this analysis. Tables A.3–A.6 show the calculated values of these systematics for this analysis. The NOvA experiment uses a customized version of GENIE.

Parameter	Description
PD3_DISvbarnCC0pi	DIS background in $\bar{\nu}n$CC0π interactions
PD3_DISvbarnCC1pi	DIS background in $\bar{\nu}n$CC1π interactions
PD3_DISvbarnCC2pi	DIS background in $\bar{\nu}n$CC2π interactions
PD3_DISvbarnCC3pi	DIS background in $\bar{\nu}n$CC3π interactions
PD3_DISvbarnNC0pi	DIS background in $\bar{\nu}n$NC0π interactions
PD3_DISvbarnNC1pi	DIS background in $\bar{\nu}n$NC1π interactions
PD3_DISvbarnNC2pi	DIS background in $\bar{\nu}n$NC2π interactions
PD3_DISvbarnNC3pi	DIS background in $\bar{\nu}n$NC3π interactions
PD3_DISvbarpCC0pi	DIS background in $\bar{\nu}p$CC0π interactions
PD3_DISvbarpCC1pi	DIS background in $\bar{\nu}p$CC1π interactions
PD3_DISvbarpCC2pi	DIS background in $\bar{\nu}p$CC2π interactions
PD3_DISvbarpCC3pi	DIS background in $\bar{\nu}p$CC3π interactions
PD3_DISvbarpNC0pi	DIS background in $\bar{\nu}p$NC0π interactions
PD3_DISvbarpNC1pi	DIS background in $\bar{\nu}p$NC1π interactions
PD3_DISvbarpNC2pi	DIS background in $\bar{\nu}p$NC2π interactions
PD3_DISvbarpNC3pi	DIS background in $\bar{\nu}p$NC3π interactions
PD3_DISvnCC0pi	DIS background in νnCC0π interactions
PD3_DISvnCC1pi	DIS background in νnCC1π interactions
PD3_DISvnCC2pi	DIS background in νnCC2π interactions
PD3_DISvnCC3pi	DIS background in νnCC3π interactions
PD3_DISvnNC0pi	DIS background in νnNC0π interactions
PD3_DISvnNC1pi	DIS background in νnNC1π interactions
PD3_DISvnNC2pi	DIS background in νnNC2π interactions
PD3_DISvnNC3pi	DIS background in νnNC3π interactions
PD3_DISvpCC0pi	DIS background in νpCC0π interactions
PD3_DISvpCC1pi	DIS background in νpCC1π interactions
PD3_DISvpCC2pi	DIS background in νpCC2π interactions
PD3_DISvpCC3pi	DIS background in νpCC3π interactions
PD3_DISvpNC0pi	DIS background in νpNC0π interactions
PD3_DISvpNC1pi	DIS background in νpNC1π interactions
PD3_DISvpNC2pi	DIS background in νpNC2π interactions
PD3_DISvpNC3pi	DIS background in νpNC3π interactions
PD3_MAQAGenieReducedSyst2017	MAQA reduced systematics
PD3_MECEnuShapeSyst2017	MEC shape
PD3_MECInitStateNPFracSyst2017	MEC composition of initial state struck nucleon pair fraction
PD3_MECq0ShapeSyst2017	MEC q0 shape
PD3_RPACCQEEnhSyst2017	RPA CCQE enhanced
PD3_RPACCQESuppSyst2017	RPA CCQE low Q^2 suppression
PD3_RPARESSyst2017	RPA RES systematics
ReweightAGKY_pT1pi	AGKY transverse momentum in single pion states

Table A.1: Neutrino interaction cross-section systematic parameters considered in NOvA. Continued in the Table A.2.

Parameter	Description
ReweightAGKY_xF1pi	AGKY Feynman x for single pion states
ReweightAhtBY	Higher-twist parameter(A_{HT}) in Bodek-Yang model
ReweightAhtBYshape	Higher-twist parameter(AHT) in Bodek-Yang model, shape only
ReweightBRIeta	Branching ratio for single-η resonance decays
ReweightBR1gamma	Branching ratio for radiative resonance decays
ReweightBhtBY	Higher-twist parameter (B_{HT}) in Bodek-Yang model
ReweightBhtBYshape	Higher-twist parameter (B_{HT}) in Bodek-Yang model, shape only
ReweightCCQEMomDistroFGtoSF	CCQE Nucleon Momentum Distribution
ReweightCCQEPauliSupViaKF	CCQE Pauli suppression (changes Fermi level k_F)
ReweightCV1uBY	C_{V1u} valence GRV98 PDF correction in Bodek-Yang Model
ReweightCV1uBYshape	C_{V1u} valence GRV98 PDF correction in Bodek-Yang Model, shape only
ReweightCV2uBY	C_{V2u} valence GRV98 PDF correction in Bodek-Yang Model
ReweightCV2uBYshape	C_{V2u} valence GRV98 PDF correction in Bodek-Yang Model, shape only
ReweightDISNuclMod	DIS nuclear modification (shadowing, anti-shadowing, EMC)
ReweightEtaNCEL	NCEL strange axial form factor eta, affects dsigma(NCEL)/dQ2 both in shape and normalization
ReweightFormZone	tweak formation zone
ReweightFrAbs_N	tweak absorption probability for nucleons, for given total rescattering probability
ReweightFrAbs_pi	tweak absorption probability for pions, for given total rescattering probability
ReweightFrCEx_N	tweak charge exchange probability for nucleons, for given total rescattering probability
ReweightFrCEx_pi	tweak charge exchange probability for pions, for given total rescattering probability
ReweightFrElas_N	tweak elastic probability for nucleons, for given total rescattering probability
ReweightFrElas_pi	tweak elastic probability for pions, for given total rescattering probability
ReweightFrInel_N	tweak inelastic probability for nucleons, for given total rescattering probability
ReweightFrInel_pi	tweak inelastic probability for pions, for given total rescattering probability
ReweightFrPiProd_N	tweak pion production probability for nucleons, for given total rescattering probability
ReweightFrPiProd_pi	tweak pion production probability for pions, for given total rescattering probability
ReweightMFP_N	mean free path for nucleons
ReweightMFP_pi	mean free path for pions
ReweightMaCCRES	Ma CCRES, affects d2sigma(CCRES)/dWdQ2 both in shape and normalization
ReweightMaNCEL	Ma NCEL, affects dsigma(NCEL)/dQ2 both in shape and normalization
ReweightMaNCRES	Ma NCRES, affects d2sigma(NCRES)/dWdQ2 both in shape and normalization
ReweightMvCCRES	Mv CCRES, affects d2sigma(CCRES)/dWdQ2 both in shape and normalization
ReweightMvNCRES	Mv NCRES, affects d2sigma(NCRES)/dWdQ2 both in shape and normalization
ReweightNC	NC total normalization
ReweightNormDISCC	tweak the inclusive DIS CC normalization (not currently working in genie)
ReweightRnubarnuCC	tweak the ratio of (CC) / (CC) (not currently working in genie)
ReweightTheta_Delta2Npi	distort pi angular distribution in $\delta \rightarrow N + \pi$
ReweightVecCCQEshape	elastic nucleon form factors (BBA/default -> dipole) - shape only effect of dsigma(CCQE)/dQ2

Table A.2: Neutrino interaction cross-section systematic parameters considered in NOvA.

	(%) +2σ		(%) +1σ		(%) -1σ		(%) -2σ	
	ν_τ Sig.	Background	ν_τ Sig.	Background	ν_τ Sig.	Background	ν_τ Sig.	Background
PD3_DISvbarnCC0pi	0	0.01264	0	0.006318	0	0.006318	0	0.01264
PD3_DISvbarnCC1pi	0.07362	0.05249	0.03681	0.02625	0.03681	0.02625	0.07362	0.05249
PD3_DISvbarnCC2pi	0.1493	0.04531	0.07465	0.02266	0.07465	0.02266	0.1493	0.04531
PD3_DISvbarnCC3pi	0.1592	0.09837	0.07959	0.04919	0.07959	0.04919	0.1592	0.09837
PD3_DISvbarnNC0pi	0	0.001247	0	0.0006234	0	0.0006234	0	0.001247
PD3_DISvbarnNC1pi	0	0	0	0	0	0	0	0
PD3_DISvbarnNC2pi	0	0.006963	0	0.003482	0	0.003482	0	0.006963
PD3_DISvbarnNC3pi	0	0.03601	0	0.01801	0	0.01801	0	0.03601
PD3_DISvbarpCC0pi	0.2178	0.08205	0.1089	0.04102	0.1089	0.04102	0.2178	0.08205
PD3_DISvbarpCC1pi	0.4059	0.1424	0.203	0.07121	0.203	0.07121	0.4059	0.1424
PD3_DISvbarpCC2pi	0.1859	0.05872	0.09295	0.02936	0.09295	0.02936	0.1859	0.05872
PD3_DISvbarpCC3pi	0.3679	0.1235	0.184	0.06177	0.184	0.06177	0.3679	0.1235
PD3_DISvbarpNC0pi	0	0.02195	0	0.01097	0	0.01097	0	0.02195
PD3_DISvbarpNC1pi	0	0.0009413	0	0.0004707	0	0.0004707	0	0.0009413
PD3_DISvbarpNC2pi	0	0.00496	0	0.00248	0	0.00248	0	0.00496
PD3_DISvbarpNC3pi	0	0.05605	0	0.02803	0	0.02803	0	0.05605
PD3_DISvnCC0pi	0.2148	0.06629	0.1074	0.03314	0.1074	0.03314	0.2148	0.06629
PD3_DISvnCC1pi	3.656	0.8304	**1.828**	0.4152	**1.828**	0.4152	3.656	0.8304
PD3_DISvnCC2pi	4.316	0.9811	**2.158**	0.4906	**2.158**	0.4906	4.316	0.9811
PD3_DISvnCC3pi	8.313	3.543	**4.156**	**1.771**	**4.156**	**1.771**	8.313	3.543
PD3_DISvnNC0pi	0	0.01501	0	0.007504	0	0.007504	0	0.01501
PD3_DISvnNC1pi	0	0.2316	0	0.1158	0	0.1158	0	0.2316
PD3_DISvnNC2pi	0	0.3982	0	0.1991	0	0.1991	0	0.3982
PD3_DISvnNC3pi	0	1.546	0	0.7731	0	0.7731	0	1.546
PD3_DISvpCC0pi	1.55	0.598	0.7751	0.299	0.7751	0.299	1.55	0.598
PD3_DISvpCC1pi	0.5758	0.1776	0.2879	0.08879	0.2879	0.08879	0.5758	0.1776
PD3_DISvpCC2pi	1.539	0.4319	0.7694	0.216	0.7694	0.216	1.539	0.4319
PD3_DISvpCC3pi	3.327	1.919	**1.664**	0.9594	**1.664**	0.9594	3.327	1.919
PD3_DISvpNC0pi	0	0.4674	0	0.2337	0	0.2337	0	0.4674
PD3_DISvpNC1pi	0	0.08093	0	0.04046	0	0.04046	0	0.08093
PD3_DISvpNC2pi	0	0.2213	0	0.1107	0	0.1107	0	0.2213
PD3_DISvpNC3pi	0	1.346	0	0.6732	0	0.6732	0	1.346
PD3_MAQAGenieReducedSyst2017	1.543	0.1391	0.7716	0.06955	0.6988	0.06121	1.398	0.1224
PD3_MECEnuShapeSyst2017	0.1602	0.08205	0.08009	0.04103	0.08009	0.04103	0.1602	0.08205
PD3_MECInitStateNPFracSyst2017	0.3498	0.06729	0.1749	0.03364	0.1749	0.03364	0.3498	0.06729
PD3_MECq0ShapeSyst2017	3.375	1.387	**1.533**	0.8196	0.4427	0.3844	2.47	0.1991
PD3_RPACCQEEnhSyst2017	7.922	4.058	**3.961**	**2.029**	**3.43**	**1.961**	6.859	3.922
PD3_RPACCQESuppSyst2017	1.351	0.1069	0.6756	0.05346	0.6505	0.04148	1.299	0.08218
PD3_RPARESSyst2017	1.524	0.2497	0.7622	0.1248	0	0	0	0
ReweightAGKY_pT1pi	0.01266	0	0.01808	0	0.008777	0	0.01502	0

Table A.3: The percentage difference between the shifted and nominal predictions for the number of selected $\nu_\mu \to \nu_\tau$ ND events due to neutrino interaction cross-section systematics. Continued in the Table A.4.

	(%) +2σ		(%) +1σ		(%) -1σ		(%) -2σ	
	ν_τ Sig.	Background	ν_τ Sig.	Background	ν_τ Sig.	Background	ν_τ Sig.	Background
ReweightAGKY_xF1pi	0.02281	0	0.01191	0	0.0009722	0	0.005479	0
ReweightAhtBY	2.272	1.408	**1.133**	0.704	**1.132**	0.7009	2.259	1.394
ReweightAhtBYshape	0	0	0	0	0	0	0	0
ReweightBR1eta	0.229	0.02885	0.1145	0.01443	0.1145	0.01443	0.229	0.02885
ReweightBR1gamma	0.03176	0.001092	0.01588	0.0005459	0.01588	0.000546	0.03176	0.001092
ReweightBhtBY	2.49	2.789	**1.252**	**1.422**	**1.261**	**1.464**	2.537	2.972
ReweightBhtBYshape	0	0	0	0	0	0	0	0
ReweightCCQEMomDistroFGtoSF	0	0	0	0	0	0	0	0
ReweightCCQEPauliSupViaKF	1.264	0.1064	0.569	0.05008	0.396	0.03936	0.5937	0.06273
ReweightCV1uBY	0.925	1.346	0.4703	0.688	0.4872	0.7215	0.993	1.48
ReweightCV1uBYshape	0	0	0	0	0	0	0	0
ReweightCV2uBY	0.8465	1.255	0.4233	0.6274	0.4233	0.6274	0.8465	1.255
ReweightCV2uBYshape	0	0	0	0	0	0	0	0
ReweightDISNuclMod	0	0	0	0	0	0	0	0
ReweightEtaNCEL	0	0	0	0	0	0	0	0
ReweightFormZone	5.749	7.93	**4.952**	**7.411**	**14.04**	**19.62**	41.64	53.48
ReweightFrAbs_N	0.2781	0.0764	0.1361	0.03738	0.1303	0.03575	0.2547	0.06987
ReweightFrAbs_pi	0.4181	1.005	0.1949	0.5165	0.1397	0.5023	0.192	0.9544
ReweightFrCEx_N	0.2336	0.03913	0.1141	0.02165	0.1087	0.02583	0.2119	0.05584
ReweightFrCEx_pi	0.08447	0.1297	0.04795	0.06394	0.06067	0.06234	0.1354	0.1233
ReweightFrElas_N	0.8545	0.01133	0.431	0.0006159	0.4413	0.003846	0.8928	0.01215
ReweightFrElas_pi	0.04219	0.05103	0.02026	0.02368	0.01866	0.01767	0.03569	0.0272
ReweightFrInel_N	0.1526	0.1152	0.07212	0.05799	0.06378	0.0588	0.1192	0.1184
ReweightFrInel_pi	0.2615	0.5476	0.06246	0.2175	0.07277	0.2587	0.1429	0.4937
ReweightFrPiProd_N	0.09512	0.08449	0.04755	0.04224	0.04752	0.04225	0.095	0.08449
ReweightFrPiProd_pi	0.04892	0.312	0.02386	0.1544	0.02267	0.1508	0.04417	0.2975
ReweightMFP_N	1.918	1.272	**1.015**	0.6868	**1.155**	0.8233	2.48	1.843
ReweightMFP_pi	2.982	4.154	**1.605**	**2.212**	**1.792**	**2.518**	3.946	5.531
ReweightMaCCRES	7.095	0.7478	**3.316**	0.3451	**2.889**	0.296	5.262	0.5431
ReweightMaNCEL	0	0	0	0	0	0	0	0
ReweightMaNCRES	0	0.09471	0	0.02641	0	0.008957	0	0.01167
ReweightMvCCRES	3.625	0.3553	**1.641**	0.1607	**1.335**	0.1303	2.394	0.2335
ReweightMvNCRES	0	0.0108	0	0.004289	0	0.002797	0	0.004597
ReweightNC	0	0.08685	0	0	0	0	0	0
ReweightNormDISCC	0	0	0	0	0	0	0	0
ReweightRnubarnuCC	0	0	0	0	0	0	0	0
ReweightTheta_Delta2Npi	0.3504	0.08421	0.2628	0.06316	0.1752	0.0421	0.0876	0.02105
ReweightVecCCQEshape	0.1658	0.005602	0.08288	0.002803	0.08288	0.002808	0.1658	0.005612
sum of all small GENIE Systs.			1.797	1.617				
sum of all GENIE Systs.			16.04	35.87				

Table A.4: The percentage difference between the shifted and nominal predictions for the number of selected $\nu_\mu \to \nu_\tau$ ND events due to neutrino interaction cross-section systematics.

|	(%) +2σ		(%) +1σ		(%) -1σ		(%) -2σ	
	ν_μ Sig.	Background	ν_μ Sig.	Background	ν_μ Sig.	Background	ν_μ Sig.	Background
PD3_DISvbarnCC0pi	0.007631	0.001586	0.003816	0.0007932	0.003816	0.0007932	0.007631	0.001586
PD3_DISvbarnCC1pi	0.09904	0.0185	0.04952	0.00925	0.04952	0.00925	0.09904	0.0185
PD3_DISvbarnCC2pi	0.1967	0.04684	0.09833	0.02342	0.09833	0.02342	0.1967	0.04684
PD3_DISvbarnCC3pi	0.3678	0.05851	0.1839	0.02926	0.1839	0.02926	0.3678	0.05851
PD3_DISvbarnNC0pi	0	0.002411	0	0.001205	0	0.001205	0	0.002411
PD3_DISvbarnNC1pi	0	0.02315	0	0.01158	0	0.01158	0	0.02315
PD3_DISvbarnNC2pi	0	0.04783	0	0.02391	0	0.02391	0	0.04783
PD3_DISvbarnNC3pi	0	0.2234	0	0.1117	0	0.1117	0	0.2234
PD3_DISvbarpCC0pi	0.3505	0.07584	0.1753	0.03792	0.1753	0.03792	0.3505	0.07584
PD3_DISvbarpCC1pi	0.4296	0.07422	0.2148	0.03711	0.2148	0.03711	0.4296	0.07422
PD3_DISvbarpCC2pi	0.3457	0.06615	0.1729	0.03308	0.1729	0.03308	0.3457	0.06615
PD3_DISvbarpCC3pi	0.5928	0.1096	0.2964	0.05482	0.2964	0.05482	0.5928	0.1096
PD3_DISvbarpNC0pi	0	0.07905	0	0.03953	0	0.03953	0	0.07905
PD3_DISvbarpNC1pi	0	0.03248	0	0.01624	0	0.01624	0	0.03248
PD3_DISvbarpNC2pi	0	0.04627	0	0.02314	0	0.02314	0	0.04627
PD3_DISvbarpNC3pi	0	0.2389	0	0.1194	0	0.1194	0	0.2389
PD3_DISvnCC0pi	0.5954	0.1023	0.2977	0.05115	0.2977	0.05115	0.5954	0.1023
PD3_DISvnCC1pi	5.021	0.7152	**2.51**	0.3576	**2.51**	0.3576	5.021	0.7152
PD3_DISvnCC2pi	6.324	0.7205	**3.162**	0.3602	**3.162**	0.3602	6.324	0.7205
PD3_DISvnCC3pi	14.57	1.478	**7.287**	0.7388	**7.287**	0.7388	14.57	1.478
PD3_DISvnNC0pi	0	0.08826	0	0.04413	0	0.04413	0	0.08826
PD3_DISvnNC1pi	0	0.8234	0	0.4117	0	0.4117	0	0.8234
PD3_DISvnNC2pi	0	1.367	0	0.6835	0	0.6835	0	1.367
PD3_DISvnNC3pi	0	6.335	0	**3.167**	0	**3.167**	0	6.335
PD3_DISvpCC0pi	3.312	0.4128	**1.656**	0.2064	**1.656**	0.2064	3.312	0.4128
PD3_DISvpCC1pi	1.145	0.205	0.5727	0.1025	0.5727	0.1025	1.145	0.205
PD3_DISvpCC2pi	2.781	0.3814	**1.391**	0.1907	**1.391**	0.1907	2.781	0.3814
PD3_DISvpCC3pi	8.466	0.9549	**4.233**	0.4774	**4.233**	0.4774	8.466	0.9549
PD3_DISvpNC0pi	0	2.061	0	**1.031**	0	**1.031**	0	2.061
PD3_DISvpNC1pi	0	0.447	0	0.2235	0	0.2235	0	0.447
PD3_DISvpNC2pi	0	1.076	0	0.538	0	0.538	0	1.076
PD3_DISvpNC3pi	0	6.228	0	**3.114**	0	**3.114**	0	6.228
PD3_MAQAGenieReducedSyst2017	0.07551	0.03915	0.03775	0.01958	0.02671	0.01572	0.05341	0.03144
PD3_MECEnuShapeSyst2017	0.05036	0.02959	0.02518	0.0148	0.02518	0.0148	0.05036	0.02959
PD3_MECInitStateNPFracSyst2017	0.08529	0.04818	0.04265	0.02409	0.04265	0.02409	0.08529	0.04818
PD3_MECqOShapeSyst2017	0.8011	0.4355	0.4144	0.2646	0.522	0.1021	0.4583	0.04207
PD3_RPACCQEEnhSyst2017	6.099	0.8122	**3.049**	0.4061	**2.864**	0.3587	5.728	0.7174
PD3_RPACCQESuppSyst2017	0.06559	0.04389	0.0328	0.02194	0.02825	0.01954	0.0559	0.03867
PD3_RPARESSyst2017	0.1268	0.09774	0.0634	0.04887	0	0	0	0
ReweightAGKY_pT1pi	0.0005038	0.0001865	0.0005518	0.0003331	0.0003763	0.00113	0.0005144	0.00126

Table A.5: The percentage difference between the shifted and nominal predictions for the number of selected $\nu_\mu \to \nu_\mu$ ND events due to neutrino interaction cross-section systematics. Continued in the Table A.6.

	+2σ (%)		+1σ (%)		-1σ (%)		-2σ (%)	
	ν_μ Sig.	Background	ν_μ Sig.	Background	ν_μ Sig.	Background	ν_μ Sig.	Background
ReweightAGKY_xF1pi	0.0007783	0.0005043	0.0003022	0.0004709	0.0004892	0.0009394	0.0002002	0.0007643
Reweight.AhtBY	2.426	1.843	**1.217**	0.9229	**1.222**	0.9248	2.449	1.851
ReweightAhtBYshape	0	0	0	0	0	0	0	0
ReweightBR1eta	0.00276	0.01562	0.00138	0.007811	0.00138	0.007811	0.00276	0.01562
ReweightBR1gamma	4.632e-06	0.0001771	2.338e-06	8.858e-05	2.437e-06	8.862e-05	4.891e-06	0.0001773
ReweightBhtBY	3.853	3.358	**1.953**	**1.702**	**2.003**	**1.752**	4.055	3.558
ReweightBhtBYshape	0	0	0	0	0	0	0	0
ReweightCCQEMomDistroFGtoSF								
ReweightCCQEPauliSupViaKF	0.05367	0.03561	0.02554	0.01718	0.02344	0.01438	0.04291	0.02577
ReweightCV1uBY	2.216	2.107	**1.144**	**1.085**	**1.224**	**1.155**	2.54	2.39
ReweightCV1uBYshape	0	0	0	0	0	0	0	0
ReweightCV2uBY	2.133	2.012	**1.067**	**1.006**	**1.067**	**1.006**	2.133	2.012
ReweightCV2uBYshape	0	0	0	0	0	0	0	0
ReweightDISNuclMod	0	0	0	0	0	0	0	0
ReweightEtaNCEL	0	0.0001886	0	8.663e-05	0	7.133e-05	0	0.0001274
ReweightFormZone	7.399	7.303	**6.806**	**7.184**	**17.79**	**20.64**	53.46	56.9
ReweightFrAbs_N	0.02235	0.007553	0.01115	0.003706	0.01111	0.003565	0.02218	0.00699
ReweightFrAbs_pi	0.1252	1.637	0.0539	0.8197	0.05016	0.8093	0.09648	1.571
ReweightFrCEx_N	0.03322	0.0442	0.01653	0.02196	0.01638	0.02168	0.03261	0.04309
ReweightFrCEx_pi	0.01796	0.09577	0.008767	0.05011	0.007936	0.05638	0.01503	0.1212
ReweightFrElas_N	0.03782	0.04929	0.01829	0.02551	0.01818	0.02819	0.03625	0.05906
ReweightFrElas_pi	0.1019	0.3344	0.05071	0.1672	0.05015	0.1678	0.09969	0.3368
ReweightFrInel_N	0.01612	0.03372	0.008216	0.01591	0.008531	0.01402	0.01738	0.02616
ReweightFrInel_pi	0.2882	1.13	0.02285	0.7421	0.01367	0.7648	0.02508	1.575
ReweightFrPiProd_N	0.005073	0.01728	0.002504	0.008669	0.00244	0.008723	0.004815	0.0175
ReweightFrPiProd_pi	0.006289	0.1352	0.003054	0.06784	0.002865	0.06822	0.005533	0.1367
ReweightMFP_N	1.107	0.8247	0.6028	0.4524	0.7356	0.5643	1.659	1.295
ReweightMFP_pi	5.075	5.648	**2.769**	**3.064**	**2.986**	**3.355**	6.401	7.256
ReweightMaCCRES	2.982	0.6194	**1.227**	0.2793	0.8122	0.2231	1.319	0.3916
ReweightMaNCEL	0	0.09182	0	0.026	0	0.008015	0	0.00993
ReweightMvCCRES	0	0.5047	0	0.1817	0	0.07354	0	0.09651
ReweightMvNCRES	1.347	0.3135	0.5752	0.1402	0.4192	0.1113	0.7169	0.1976
ReweightNC	0	0.08915	0	0.03279	0	0.02008	0	0.03189
ReweightNormDISCC	0	0	0	0	0	0	0	0
ReweightRnubarnuCC	0	0	0	0	0	0	0	0
ReweightTheta_Delta2Npi	0.07881	0.01991	0.05911	0.01493	0.03941	0.009954	0.0197	0.004977
ReweightVecCCQEshape	0.003073	0.0003255	0.001537	0.0001628	0.001537	0.0001631	0.003077	0.000326
sum of all small GENIE Systs.	1.288		1.288	1.644				
sum of all GENIE Systs.	20.87		20.87	21.68				

Table A.6: The percentage difference between the shifted and nominal predictions for the number of selected $\nu_\mu \to \nu_\mu$ ND events due to neutrino interaction cross-section systematics.
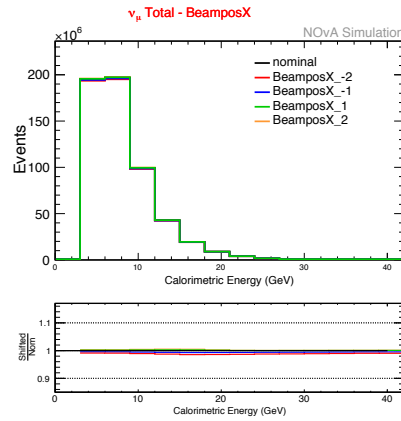
A.3   Beam Systematics

The uncertainties considered include the horn and target position, the horn current, the beam position on the target and the beam spot size. The beam systematic uncertainties calculated are shown in Figures A.1–A.10.
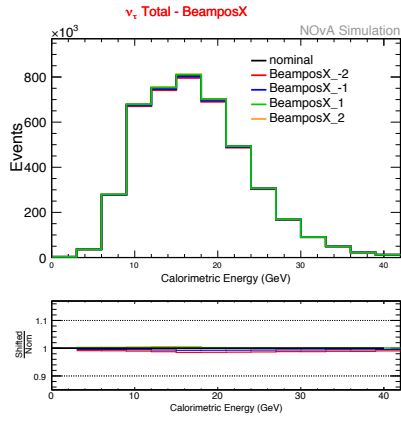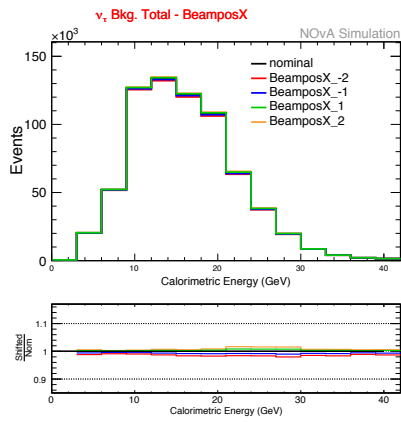
(a)

`BeamposX` systematics for signal events passing ν_τ CC selection.
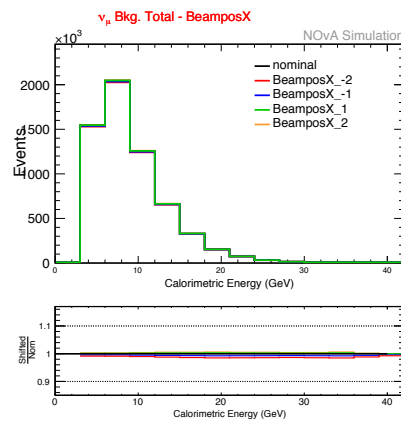

(c)

`BeamposX` systematics for signal events passing ν_μ CC selection.
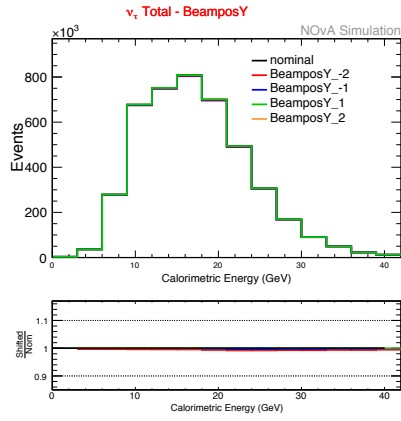

(b)
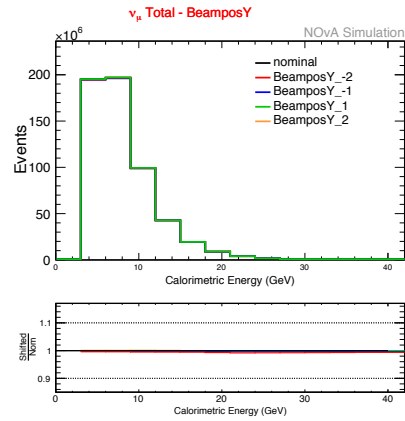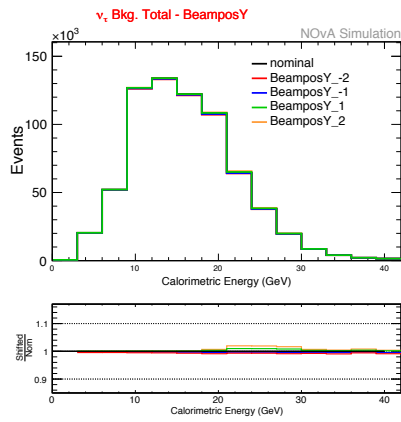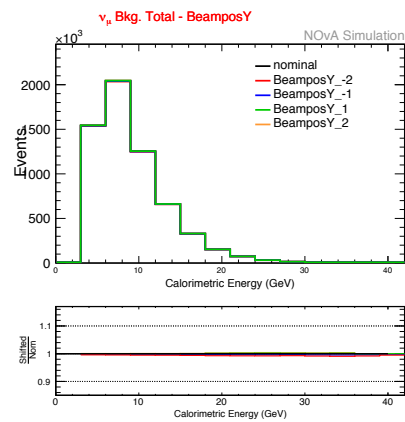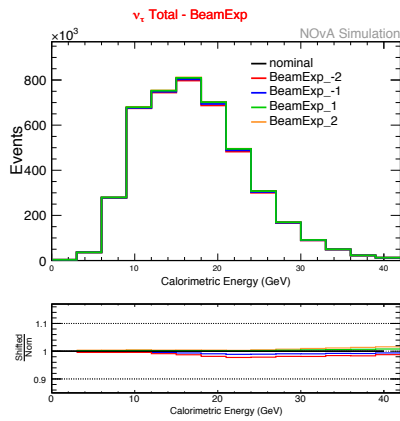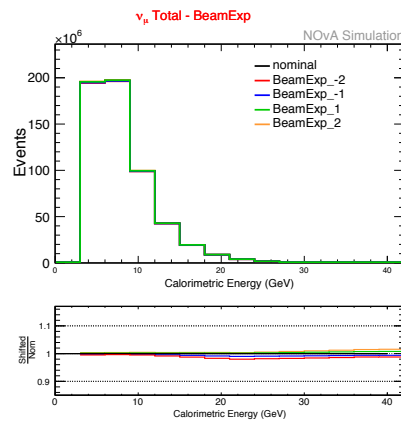
`BeamposX` systematics for background events passing ν_τ CC selection.

(d)

`BeamposX` for background events passing ν_μ CC selection.

Figure A.1: `BeamposX` systematics for background events passing ν_τ CC and ν_μ CC selections.

(a)

BeamposY systematics for signal events passing ν_τ CC selection.

(c)

BeamposY systematics for signal events passing ν_μ CC selection.

(b)

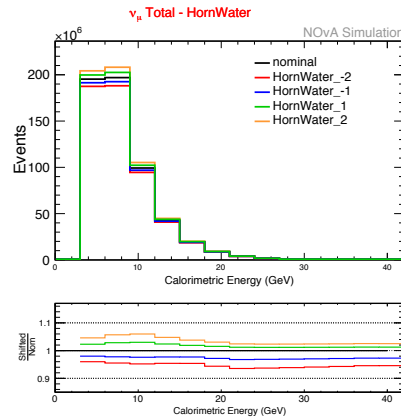BeamposY systematics for background events passing ν_τ CC selection.

(d)

BeamposY for background events passing ν_μ CC selection.

Figure A.2: BeamposY systematics for background events passing ν_τ CC and ν_μ CC selections.

(a)

BeamExp systematics for signal events passing ν_τ CC selection.

(c)

BeamExp systematics for signal events passing ν_μ CC selection.
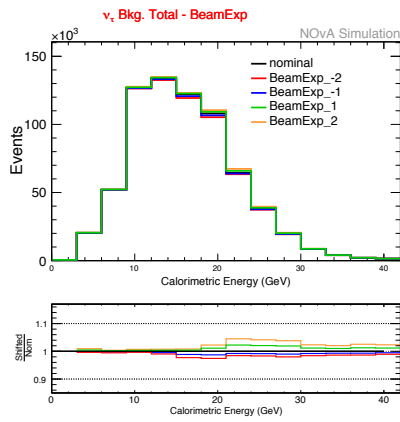
(b)

BeamExp systematics for background events passing ν_τ CC selection.
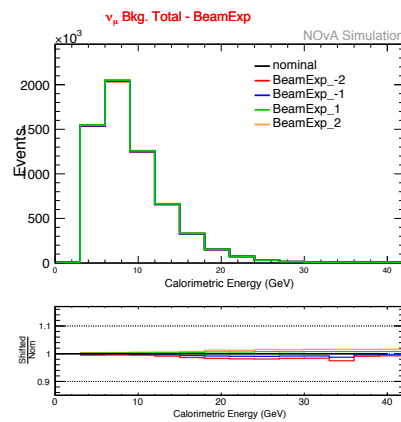
(d)

BeamExp for background events passing ν_μ CC selection.

Figure A.3: BeamExp systematics for background events passing ν_τ CC and ν_μ CC selections.
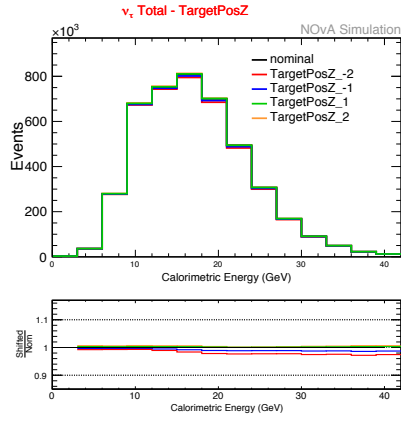
(a)

TargetPosZ systematics for signal events passing ν_τ CC selection.
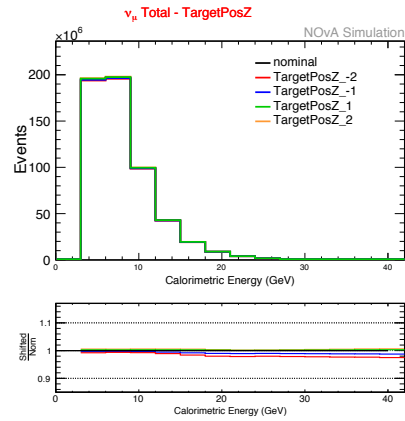
(c)

TargetPosZ systematics for signal events passing ν_μ CC selection.
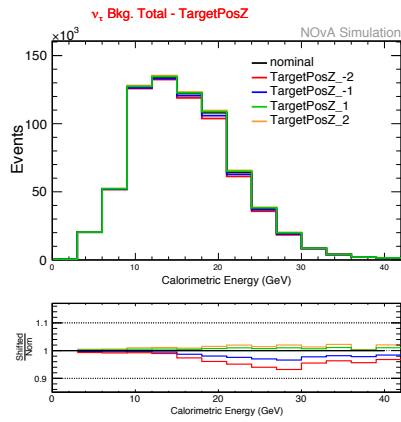
(b)

TargetPosZ systematics for background events passing ν_τ CC selection.
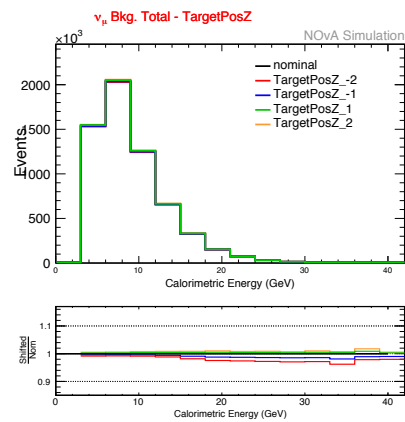
(d)

TargetPosZ for background events passing ν_μ CC selection.

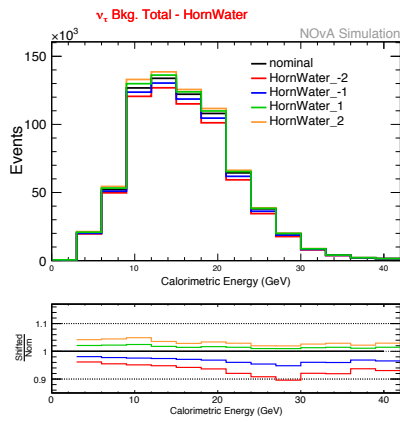Figure A.4: TargetPosZ systematics for background events passing ν_τ CC and ν_μ CC selections.
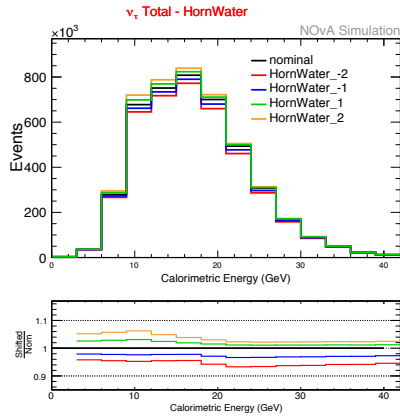
(a)

`HornWater` systematics for signal events passing ν_τ CC selection.
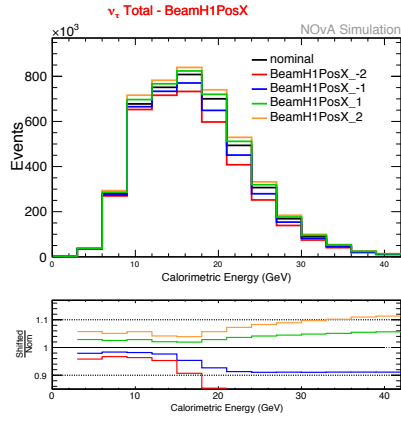
(c)

`HornWater` systematics for signal events passing ν_μ CC selection.

(b)

`HornWater` systematics for background events passing ν_τ CC selection.
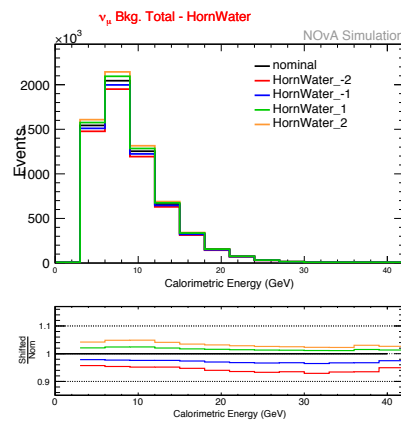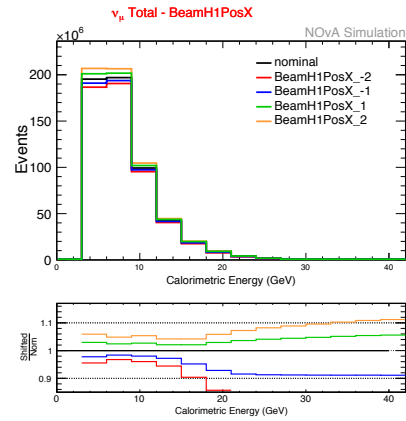
(d)

`HornWater` for background events passing ν_μ CC selection.

Figure A.5: `HornWater` systematics for background events passing ν_τ CC and ν_μ CC selections.
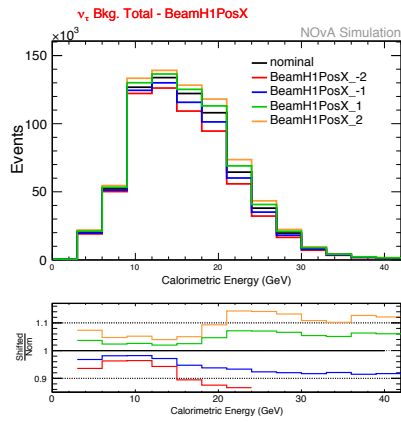
(a)

`BeamH1PosX` systematics for signal events passing ν_τ CC selection.
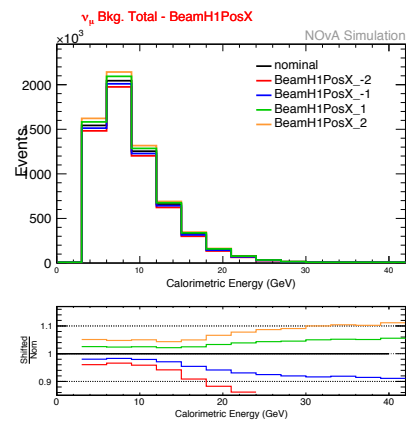

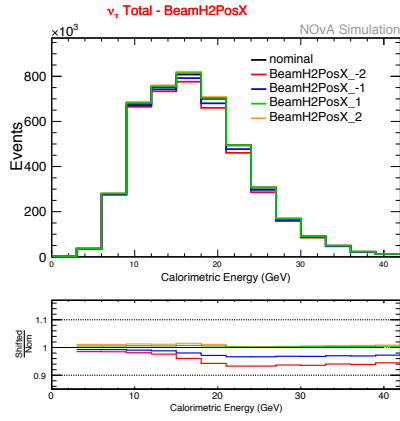(c)

`BeamH1PosX` systematics for signal events passing ν_μ CC selection.

(b)

`BeamH1PosX` systematics for background events passing ν_τ CC selection.

(d)

`BeamH1PosX` for background events passing ν_μ CC selection.

Figure A.6: `BeamH1PosX` systematics for background events passing ν_τ CC and ν_μ CC selections.

(a)

BeamH2PosX systematics for signal events passing ν_τ CC selection.

(c)

BeamH2PosX systematics for signal events passing ν_μ CC selection.

(b)

BeamH2PosX systematics for background events passing ν_τ CC selection.
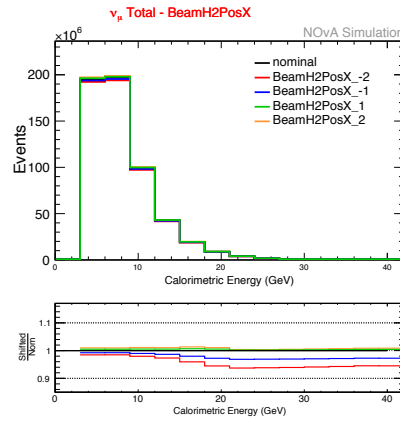
(d)

BeamH2PosX for background events passing ν_μ CC selection.

Figure A.7: BeamH2PosX systematics for background events passing ν_τ CC and ν_μ CC selections.
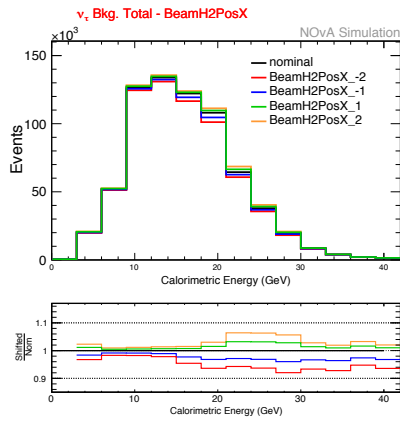
(a)

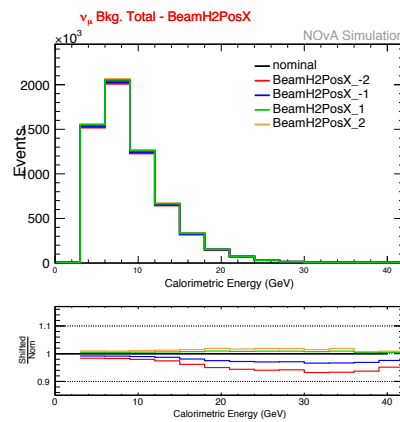BeamH1PosY systematics for signal events passing ν_τ CC selection.

(c)

BeamH1PosY systematics for signal events passing ν_μ CC selection.
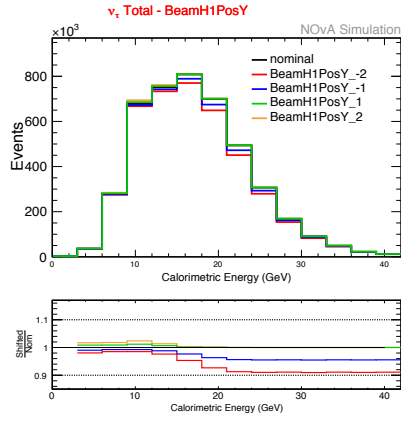
(b)

BeamH1PosY systematics for background events passing ν_τ CC selection.

(d)

BeamH1PosY for background events passing ν_μ CC selection.

Figure A.8: BeamH1PosY systematics for background events passing ν_τ CC and ν_μ CC selections.
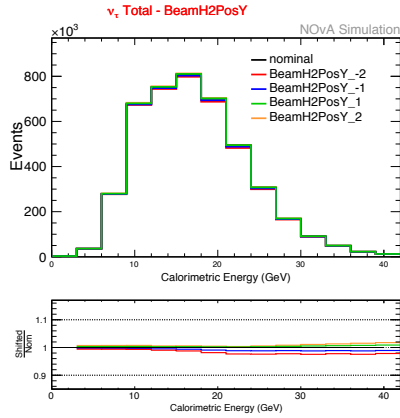
(a)

`BeamH2Pos` systematics for signal events passing ν_τ CC selection.

(c)

`BeamH2PosY` systematics for signal events passing ν_μ CC selection.
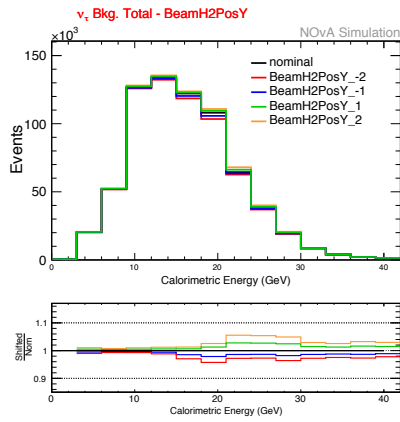
(b)

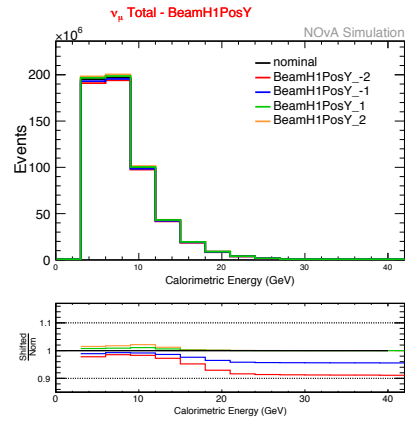`BeamH2PosY` systematics for background events passing ν_τ CC selection.

(d)

`BeamH2PosY` for background events passing ν_μ CC selection.

Figure A.9: `BeamH2PosY` systematics for background events passing ν_τ CC and ν_μ CC selections.
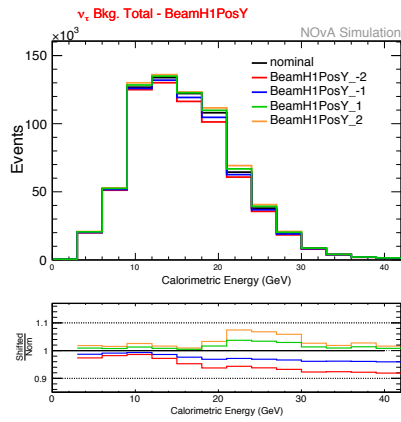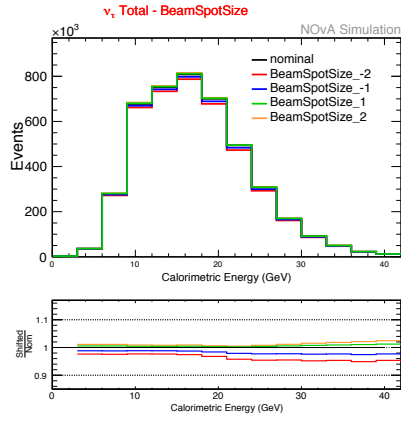
(a)

BeamSpotSize systematics for signal events passing ν_τ CC selection.
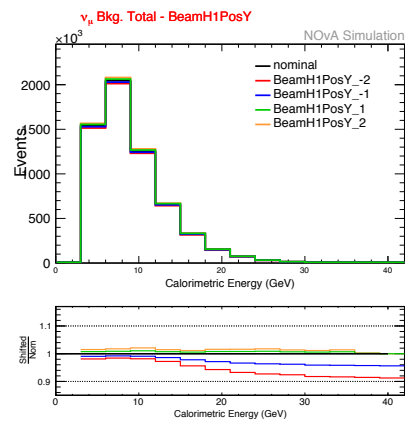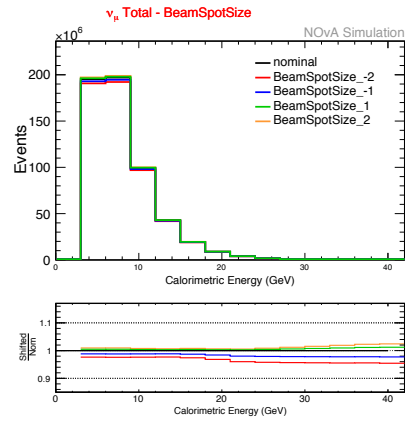
(c)

BeamSpotSize systematics for signal events passing ν_μ CC selection.
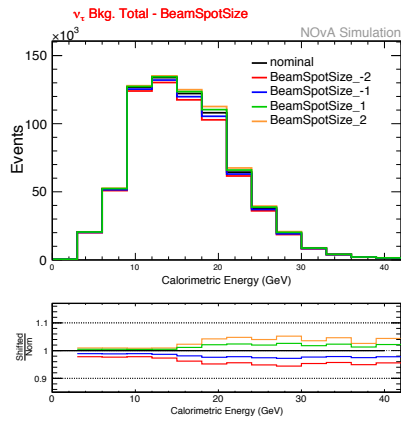
(b)

BeamSpotSize systematics for background events passing ν_τ CC selection.
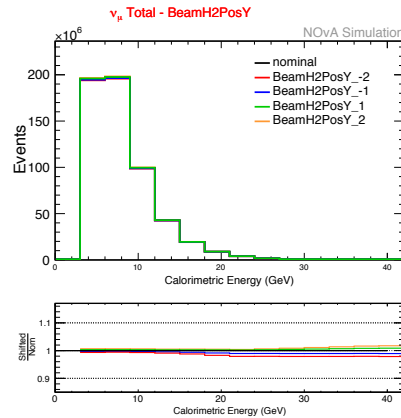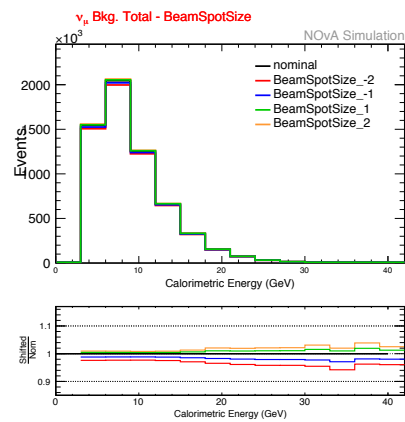
(d)

BeamSpotSize for background events passing ν_μ CC selection.

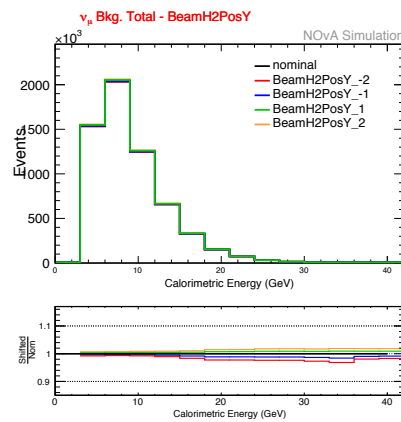Figure A.10: BeamSpotSize systematics for background events passing ν_τ CC and ν_μ CC selections.

Bibliography

[1] W. Pauli, "Dear radioactive ladies and gentlemen," *Phys. Today*, vol. 31N9, p. 27, 1978.

[2] C. S. Wu *et al.*, "Experimental test of parity conservation in beta decay," *Phys. Rev.*, vol. 105, pp. 1413–1415, Feb 1957.

[3] S. L. Glashow, "Partial Symmetries of Weak Interactions," *Nucl. Phys.*, vol. 22, pp. 579–588, 1961.

[4] S. Weinberg, "A model of leptons," *Phys. Rev. Lett.*, vol. 19, pp. 1264–1266, Nov 1967.

[5] R. N. Mohapatra *et al.*, "Neutrino Mass and New Physics," *Annual Review of Nuclear and Particle Science*, vol. 56, pp. 569–628, 2006.

[6] P.B Pal, "A Real Version of the Dirac Equation and Its Coupling to the Electromagnetic Field," *American Journal of Physics*, vol. 79, pp. 485–498, 2011.

[7] F. Reines and C. L. Cowan, "Detection of the free neutrino," *Phys.*

Rev., vol. 92, pp. 830–831, Nov 1953.

[8] C. L. Cowan *et al.*, "Detection of the free neutrino: a confirmation," *Science*, vol. 124, no. 3212, pp. 103–104, 1956.

[9] Davide D'Angelo, "Low Energy Neutrino Measurements," 2012.

[10] G. Danby *et al.*, "Observation of high-energy neutrino reactions and the existence of two kinds of neutrinos," *Phys. Rev. Lett.*, vol. 9, pp. 36–44, Jul 1962.

[11] K. Kodama *et al.*, "Observation of tau neutrino interactions," *Physics Letters B*, vol. 504, no. 3, pp. 218 – 224, 2001.

[12] J.A. Bagger, "Precision electroweak measurements on the z resonance," *Physics Reports*, vol. 427, no. 5, pp. 257 – 454, 2006.

[13] J. N. Bahcall, "Solar neutrinos. i. theoretical," *Phys. Rev. Lett.*, vol. 12, pp. 300–302, Mar 1964.

[14] L. Wolfenstein, "Neutrino oscillations in matter," *Phys. Rev. D*, vol. 17, pp. 2369–2374, May 1978.

[15] B. T. Cleveland *et al.*, "Measurement of the Solar Electron Neutrino Flux with the Homestake Chlorine Detector," *Astrophys.J*, vol. 496, pp. 505–526, 1998.

[16] J. N. Abdurashitov *et al.*, "The Russian-American Gallium Experiment (SAGE) Cr Neutrino Source Measurement," *Phys. Rev. Lett.*,

vol. 77, p. 4708, 1996.

[17] J. Abdurashitov *et al.*, " Measurement of the solar neutrino capture rate with gallium metal. III: Results for the 2002–2007 data-taking period," *Phys. Rev.*, vol. C80, p. 015807, 2009.

[18] P. Anselmann *et al.*, "Solar neutrinos observed by GALLEX at Gran Sasso," *Phys. Lett.*, vol. B285, pp. 376–389, 1992.

[19] P. Anselmann *et al.*, "Solar Neutrino Data Covering Solar Cycle 22," *Phys. Lett.*, vol. B285, p. 376, 1992.

[20] B. Pontecorvo, "Neutrino Experiments and the Problem of Conservation of Leptonic Charge," *JETP*, vol. 26, no. 5, pp. 984–988, 1968.

[21] Z. Maki *et al.*, "Remarks on the Unified Model of Elementary Particles," *Prog. Theor. Phys.*, vol. 28, p. 870, 1962.

[22] Q. Ahmad *et al.*, "Measurement of the Rate of $\nu_e + \text{d} \to \text{p} + \text{p} + \text{e}^-$ Interactions Produced by ^8B Solar Neutrinos at the Sudbury Neutrino ," *Phys. Rev. Lett.*, vol. 87, p. 071301, 2001.

[23] Q. Ahmad *et al.*, "Direct Evidence for Neutrino Flavor Transformation from Neutral-Current Interactions in the Sudbury Neutrino Observatory," *Phys. Rev. Lett.*, vol. 89, p. 011301, 2002.

[24] I. Stockdale *et al.*, "Limits on Muon-Neutrino Oscillations in the Mass Range $30 < \Delta\text{m}^2 < 1000 \text{ eV}^2/\text{c}^4$," *Phys. Rev. Lett.*, vol. 52, p. 1384, 1984.

[25] F. Dydak *et al.*, "A Search for Muon-neutrino Oscillations in the Δm^2 Range 0.3 eV^2 to 90 eV^2," *Phys. Lett.*, vol. B134, pp. 281–286, 1984.

[26] G. Cheng *et al.*, "Dual baseline search for muon antineutrino disappearance at 1 eV^2 < Δm^2 < 100 eV^2," *Phys. Rev.*, vol. D86, p. 052009, 2012.

[27] Y. J. Ko *et al.*, "Sterile neutrino search at NEOS Experiment," *Phys. Rev. Lett.*, vol. 118, p. 121802, 2017.

[28] A. Aguilar *et al.*, "Observation of a Significant Excess of Electron-Like Events in the MiniBooNE Short-Baseline Neutrino Experiment,"

[29] M. Ahn *et al.*, "Measurement of neutrino oscillation by the K2K experiment," *Phys. Rev.*, vol. D74, p. 072003, 2006.

[30] S. Fukuda *et al.*, "Determination of solar neutrino oscillation parameters using 1496 days of Super-Kamiokande I data," *Phys. Lett.*, vol. B539, pp. 179–187, 2002.

[31] P. Adamson *et al.*, "First measurement of muon-neutrino disappearance in NOvA," *Phys. Rev.*, vol. D93, p. 051104, 2016.

[32] P. Adamson *et al.*, "Measurement of the Neutrino Mass Splitting and Flavor Mixing by MINOS," *Phys. Rev. Lett.*, vol. 106, p. 181801, 2011.

[33] F. Ardellier *et al.*, "Letter of Intent for Double-CHOOZ: a Search for the Mixing Angle Theta13,"

[34] F. P. An *et al.*, "Observation of Electron-Antineutrino Disappearance at Daya Bay," *Phys. Rev. Lett.*, vol. 108, p. 171803, 2012.

[35] J. H. Choi *et al.*, "Observation of Energy and Baseline Dependent Reactor Antineutrino Disappearance in the RENO Experiment," *Phys. Rev. Lett.*, vol. 116, p. 211801, 2016.

[36] K. Eguchi *et al.*, "Determination of solar neutrino oscillation parameters using 1496 days of Super-Kamiokande I data," *Phys. Rev. Lett.*, vol. 90, p. 021802, 2003.

[37] P. Vogel, "Analysis of the antineutrino capture on protons," *Phys. Rev.*, vol. D29, p. 1918, 1984.

[38] A. Menegolli, "Some recent results from the icarus experiment," *Nuclear and Particle Physics Proceedings*, vol. 273-275, pp. 1891 – 1896, 2016. 37th International Conference on High Energy Physics (ICHEP).

[39] K. Kodama *et al.*, "Observation of tau neutrino interactions," *Physics Letters B*, vol. 504, pp. 218–224, 2001.

[40] K. Kodama *et al.*, "Final tau-neutrino results from the DONuT experiment," *Phys. Rev. D*, vol. 78, 2008.

[41] M. L. Perl *et al.*, "Evidence for anomalous lepton production in

$e^+ - e^-$ annihilation," *Phys. Rev. Lett.*, vol. 35, pp. 1489–1492, Dec 1975.

[42] K. Abe *et al.*, "Measurement of the τ neutrino helicity and michel parameters in polarized e^+e^- collisions," *Phys. Rev. Lett.*, vol. 78, pp. 4691–4696, Jun 1997.

[43] R. Barate *et al.*, "An upper limit on the τ neutrino mass from three and five-prong tau decays," *The European Physical Journal C - Particles and Fields*, vol. 2, pp. 395–406, Apr 1998.

[44] M. Acciarri *et al.*, "Measurement of the Michel parameters and the average tau-neutrino helicity from tau decays in e+ e- —> tau+ tau-," *Phys. Lett.*, vol. B377, pp. 313–324, 1996.

[45] M. Guler *et al.*, "Opera: An appearance experiment to search for $\nu_\mu \rightarrow \nu_\tau$ oscillations in the cngs beam," *Experimental proposal*, vol. Tech. Rep. CERN-SPSC-2000-028, 2000.

[46] N. Agafonova *et al.*, "Discovery of τ neutrino appearance in the cngs neutrino beam with the opera experiment," *Phys. Rev. Lett.*, vol. 115, p. 121802, Sep 2015.

[47] Robert M. Zwaska, "Accelerator system and instrumentation for the numi neutrino beam. phd thesis," *University of Texas, Austin*, 2005.

[48] D. Ayres *et al.*, "The nova technical design report.," *Fermilab, Batavia, Illinois*, 2007.

[49] E. Niner *et al.*, "Synchronization of the 14 kton nova neutrino detector with the fermilab numi beam," vol. 513.

[50] Mark Messier, "NOvA Internal Document: Vertex Reconstruction Based on Elastic Arms." `https://nova-docdb.fnal.gov/cgi-bin/private/ShowDocument?docid=7530`.

[51] Evan Niner, "NOvA Internal Document: Vertex Clustering with Possibilistic Fuzzy-K Means Algorithm." `https://nova-docdb.fnal.gov/cgi-bin/private/ShowDocument?docid=7648`.

[52] JÃČÂűrg SanderMartin EsterHans-Peter KriegelXiaowei Xu, "Density-Based Clustering in Spatial Databases: The Algorithm GDBSCAN and Its Applications," *Data Mining and Knowledge Discovery*, vol. 2, p. 169, 1998.

[53] S. Mufson *et al.*, "Liquid scintillator production for the nova experiment," *Nuclear Instruments and Methods in Physics Research Section A: Accelerators, Spectrometers, Detectors and Associated Equipment*, vol. 799, pp. 1 – 9, 2015.

[54] Campanella M, Ferrari A, Sala P and Vanini S, "First Calorimeter Simulation with the FLUGG Prototype," tech. rep., 1999.

[55] T. Bohlen *et al.*, "The FLUKA Code: Developments and Challenges for High Energy and Medical Applications," *Nuclear Data Sheets*, vol. 120, pp. 211–214, 2014.

[56] Ferrari, A.; Sala, P.R.; /CERN /INFN, Milan; Fasso, A.; /SLAC; Ranft, J.; /Siegen U., "FLUKA: A Multi-Particle Transport Code," 2005.

[57] R. Merenyi *et al.*, "Determination of pion intranuclear rescattering rates in ν_μ Ne versus ν_μ D interactions for the atmospheric neutrino flux," *Phys. Rev.*, vol. D45, pp. 743–751, 1992.

[58] C. Hagmann *et al.*, "Determination of pion intranuclear rescattering rates in ν_μ Ne versus ν_μ D interactions for the atmospheric neutrino flux," *IEEE Nuclear Science Symp. Conf. Rec. (Honolulu, HI)*, vol. 2, pp. 1143–1146, 2007.

[59] L. Fernandes *et al.*, "Real-timeline detection through an improved hough transform voting scheme," *Pattern Recognition*, vol. 41, p. 299âĂŞ314, 2008.

[60] R. E. Kalman, "A new approach to linear filtering and prediction problems," *Transactions of the ASMEâĂŞJournal of Basic Engineering*, vol. 82(Series D), pp. 35–45, 1960.

[61] C. Szegedy *et al.*, "Going deeper with convolutions,"

[62] Y. Jia *et al.*, "Caffe: Convolutional architecture for fast feature embedding,"

[63] Y. LeCun *et al.*, *Neural Networks: Tricks of the Trade.* Springer-Verlag Berlin Heidelberg, 1998.

[64] A. Hoecker *et al.*, "Tmva 4 toolkit for multivariate data analysis with root," *http://tmva.sourceforge.net/docu/TMVAUsersGuide.pdf.*

[65] J. A. Sepulveda-Quiroz, "Energy estimator based on a bdt for uncontained muons at the fardet - technote," *NOvA Document Database*, vol. DocDB 24466.

[66] G. Davies, "Cvn - 2018," *NOvA Document Database*, vol. DocDB 27467.

[67] J. H. Friedman, "Greedy function approximation: A gradient boosting mechine," *https://statweb.stanford.edu/ jhf/ftp/trebst.pdf.*

[68] R. Keloth, "First look at sideband - nutau appearance ana in nd-talk," *NOvA Document Database*, vol. DocDB 24858.

[69] R. Keloth, "The first nova short-baseline joint $\nu_\mu - \nu_\tau$ analysis executive summary," *NOvA Document Database*, vol. DocDB 30549.

[70] A. Aguilar *et al.*, "Evidence for neutrino oscillations from the observation of $\overline{\nu}_e$ appearance in a $\overline{\nu}_\mu$ beam," *Phys. Rev. D*, vol. 64, p. 112007, Nov 2001.

[71] A. Aguilar *et al.*, "Search for electron neutrino appearance at the $\Delta m^2 \sim 1$ ev^2 scale," *Phys. Rev. Lett.*, vol. 98, p. 231801, Jun 2007.

[72] N. Ushida *et al.*, "Limits to $\nu_\mu, \nu_e \to \nu_\tau$ oscillations and $\nu_\mu, \nu_e \to \tau^-$ direct coupling," *Phys. Rev. Lett.*, vol. 57, pp. 2897–2900, Dec 1986.

[73] A. Aurisano *et al.*, "A convolutional neural network neutrino event classifier," *Journal of Instrumentation*, vol. 11, no. 09, p. P09001, 2016.

[74] P. Adamson, ..., R. Keloth, *et al.*, "Measurement of the neutrino mixing angle θ_{23} in nova," *Phys. Rev. Lett.*, vol. 118, p. 151802, Apr 2017.

[75] P. Adamson, ..., R. Keloth, *et al.*, "Search for active-sterile neutrino mixing using neutral-current interactions in nova," *Phys. Rev. D*, vol. 96, p. 072006, Oct 2017.

[76] P. Adamson, ..., R. Keloth, *et al.*, "Constraints on oscillation parameters from ν_e appearance and ν_μ disappearance in nova," *Phys. Rev. Lett.*, vol. 118, p. 231801, Jun 2017.

[77] A. Aurisano *et al.*, "Position paper for 2017 joint ν_e appearance and ν_μ disappearance short-baseline oscillation analysis at the nova near detector," *NOvA Document Database*, vol. DocDB 26208.

[78] Wikipedia, "Plagiarism — Wikipedia, the free encyclopedia," 2018. [Online; accessed 3-Nov-2018].

[79] CERN Open Data, "Plagiarism — open data cern," 2018. [Online; accessed 3-Nov-2018].

[80] P. Astier *et al.*, "Final nomad results on $\nu_m u \rightarrow \nu_\tau$ and $\nu_e \rightarrow \nu_\tau$ oscillations including a new search for ν_τ appearance using hadronic

τ decays," *Nuclear Physics B*, vol. 611, no. 1, pp. 3 – 39, 2001.

[81] E. Eskut *et al.*, "Final results on $\nu_\mu \to \nu_\tau$ oscillation from the chorus experiment," *Nuclear Physics B*, vol. 793, no. 1, pp. 326 – 343, 2008.

[82] E. Radicioni *et al.*, "Results from the chorus experiment at cern," *Nuclear Physics B - Proceedings Supplements*, vol. 85, no. 1, pp. 95 – 100, 2000.

[83] R. Keloth, "The first nova sbl joint $\nu_\mu - \nu_\tau$ analysis- systematics summary," *NOvA Document Database*, vol. DocDB 30552.

[84] R. Keloth, "Sbl ν_τ appearance analysis- hadronic mode ν_τ cc pid training summary," *NOvA Document Database*, vol. DocDB 30555.

[85] S. Cavanaugh, "A measurement of electron neutrino appearance in the minos experiment after four years of data," *MINOS thesis*, vol. Fermilab-Thesis-2010-15.

[86] T. K. Warburton, "File shift systematics technote for ν_μ 2017 analysis," *NOvA Document Database*, vol. DocDB 23138.

[87] A. Aurisano, "Tech note: 2017 light model," *NOvA Document Database*, vol. DocDB 23228.

[88] Mathew Strait, "Muon energy scale systematics," *NOvA Document Database*, vol. DocDB 20816.

[89] H. Duyang *et al.*, "A technote describing the derivation and size

of numi flux uncertainties used in the first nova analyses," *NOvA Document Database*, vol. DocDB 13584.

[90] L. Aliaga *et al.*, "Beam systematic uncertainties for third analyses," *NOvA Document Database*, vol. DocDB 17608.

[91] L. Aliga, "Numi beam prediction for the nova 2017 analyses," *NOvA Document Database*, vol. DocDB 23441.

[92] L. Aliga *et al.*, "Package to predict the flux.," *https: //cd-cvs.fnal.gov/redmine/projects/ppfx/wiki/PPFX*.

[93] Andreopoulos C et al., "The GENIE Neutrino Monte Carlo Generator," *Nucl. Instrum. Meth.*, vol. A614, pp. 87–104, 2010.

[94] A. S *et al.*, "GEANT4: A Simulation toolkit," *Nucl. Instrum. Meth.*, vol. A506, pp. 250–303, 2003.